

ALMA MATER STUDIORUM
UNIVERSITÀ DEGLI STUDI DI BOLOGNA

Dottorato di Ricerca in Fisica - XXIII Ciclo

Settore Scientifico Disciplinare : FIS/01 - FIS/04

**MEASUREMENT OF THE MUON-INDUCED
NEUTRON FLUX AT LNGS
WITH THE LVD EXPERIMENT**

Relatore:
Prof.ssa G. Sartorelli

Candidato:
Rino Persiani

Correlatore:
Dr. M. Selvi

Coordinatore del dottorato:
Prof. F. Ortolani

Esame finale anno 2011

Contents

Introduction	1
1 The underground physics and neutrons	3
1.1 The Gran Sasso National Laboratory	3
1.1.1 Experiments and physics studied in the LNGS	4
1.2 Origin of neutrons in the underground laboratories	7
1.2.1 Neutrons from natural radioactivity	7
1.2.2 Muon-induced neutrons	12
2 The LVD detector	17
2.1 Detector description	17
2.2 DAQ and Electronic description	19
2.3 Energy calibration and resolution	21
2.4 Physics studied in LVD	22
2.4.1 Detection of supernova neutrinos	23
2.4.2 Neutrino oscillations	25
2.4.3 Monitor of the CNGS beam	26
2.4.4 Cosmic rays	27
2.4.5 Other topics	29
2.5 Detector status	30
3 Monte Carlo simulation programs	33
3.1 Historical introduction	33
3.1.1 GEANT3	35
3.1.2 FLUKA	37

3.1.3	Geant4	39
3.1.4	Reasons of the Geant4 choice	41
3.2	Structure of the simulation	43
3.2.1	Geometries	43
3.2.2	EventGenerators	44
3.2.3	Physics Lists	46
3.2.4	Output Format	49
3.2.5	Materials	50
3.3	Physics lists validation	51
4	Neutron measurements and simulations	55
4.1	Existing measurements and simulations	55
4.1.1	Neutron propagation	56
4.1.2	Neutron production	60
4.1.3	Neutron flux	66
4.2	Neutron yield	66
4.3	Neutrons from a ^{252}Cf source	76
4.3.1	^{252}Cf source placed in the center of a tank	77
4.3.2	^{252}Cf source placed in the LVD detector	78
4.4	Neutrons coming from the rock	80
4.4.1	Simulation description	80
4.4.2	Neutron energy spectrum	82
4.4.3	Neutron flux	84
4.4.4	Neutron multiplicity	86
4.4.5	Neutrons generation processes	87
5	An application: LVD Core Facility	89
5.1	LVD core facility	89
5.1.1	LVD-CF simulation description	92
5.1.2	LVD-CF simulation results	94
6	The muon-induced neutron yield measurements	103
6.1	LVD simulation description	103
6.1.1	Digitization	104

6.1.2	Selection cuts	105
6.2	Background, capture time and efficiencies estimation	108
6.2.1	Description of the analysis procedure	108
6.2.2	Mean neutron capture time: MC estimation	110
6.2.3	Background evaluation	116
6.2.4	Low energy threshold	118
6.2.5	Efficiency evaluation	122
6.2.6	Number of neutrons	123
6.3	The neutron yield measurement	125
6.3.1	LVD neutron yield	125
6.3.2	The iron and liquid scintillator neutron yield	126
	Conclusions	129
	Bibliography	131

Introduction

In Astroparticle Physics usually the experiments need an environment with an extremely low background, in order to be able to detect the rare events like neutrino or dark matter interactions.

The ultimate background for the experiments located deep underground is due to fast neutrons, in particular those induced by high energy cosmic muons.

The typical flux of muon-induced neutrons is three order of magnitude smaller than the flux of neutrons produced by radioactivity, so it is very difficult to be measured and it is currently not well known. Monte Carlo simulations predict that muon-induced neutrons have a hard energy spectrum and they can travel far away from the muon track. That makes very difficult to shield them.

The LVD detector, operating since 1992, is a multipurpose detector consisting of ~ 1000 ton of liquid scintillator and ~ 1000 ton of iron. Its main goal is the search of neutrinos from gravitational stellar collapses within our Galaxy, detecting both products (e^+ and neutron) of the inverse- β decay ($\bar{\nu}_e + p \rightarrow e^+ + n$). LVD is also able to reconstruct cosmic muons crossing the detector. That provides a valid way to measure the muon-induced neutrons yield in iron and liquid scintillator.

In this thesis we describe the Monte Carlo simulation of the LVD detector, developed with the Geant4 toolkit, and its applications to: a) estimate the performances of LVD to host a next generation dark matter experiments, acting as a shield and muon veto, b) measure the muon-induced neutron yield in the liquid scintillator and iron.

The use of Geant4 in a wide range of experiments assure an extensively tested toolkit. This fact, joined with the improved neutrons handling, has led to the choice to base our simulation (LVDG4) on Geant4 among other toolkits. Several tests have been performed to compare the LVDG4 both with measurements carried

out by LVD and with simulations based on other toolkits: in particular neutron flux coming from the rock has been estimated and compared with the flux obtained with a simulation based on the FLUKA program.

We demonstrate that the most internal part of LVD (the so-called "LVD core facility") can be used to host a next generation experiment searching dark matter, providing a good shield for gamma and a very good muon veto.

Finally, data collected with LVD during 4 years were analysed and the measurement of the muon-induced neutron yield in iron and liquid scintillator has been obtained. This is the first measurement ever done for iron, providing an important validation for the MC simulations of neutron production in heavy materials that are often used as shield in low background experiments. The neutron yield in scintillator compares well with previous measurements performed by other underground experiments at different depths (which means different average muon energy) and with the general trend of theoretical prediction and MC simulations.

Chapter 1

The underground physics and neutrons

All the experiments looking for rare events, such as neutrino interactions, neutrinoless double- β decay, dark matter interactions and so on, need to improve dramatically the sensitivity of detection and so they have to suppress the background level due to cosmic rays and natural radioactivity. For these reasons the experiments are usually located deep underground, where the flux of cosmic rays is reduced by many order of magnitude. In addition shields and radiopure materials are used for the detector design and construction. After a brief presentation of the Gran Sasso National Laboratory, its scientific program and the experiments currently running, will be discussed in section 1.1. Finally in section 1.2 the origin of neutrons in the underground laboratories will be shown.

1.1 The Gran Sasso National Laboratory

The Gran Sasso National Laboratory (LNGS) of INFN is an underground research infrastructure devoted to astroparticle physics. It was born from an idea of Prof. Antonino Zichichi in the 80s when he was the director of the INFN [1]. The laboratory is located between L'Aquila and Teramo on one side of the highway tunnel (10 *km* long) which crosses the Gran Sasso massif. The underground laboratory consists of three huge experimental halls (each one 100 *m* long, 20 *m* large

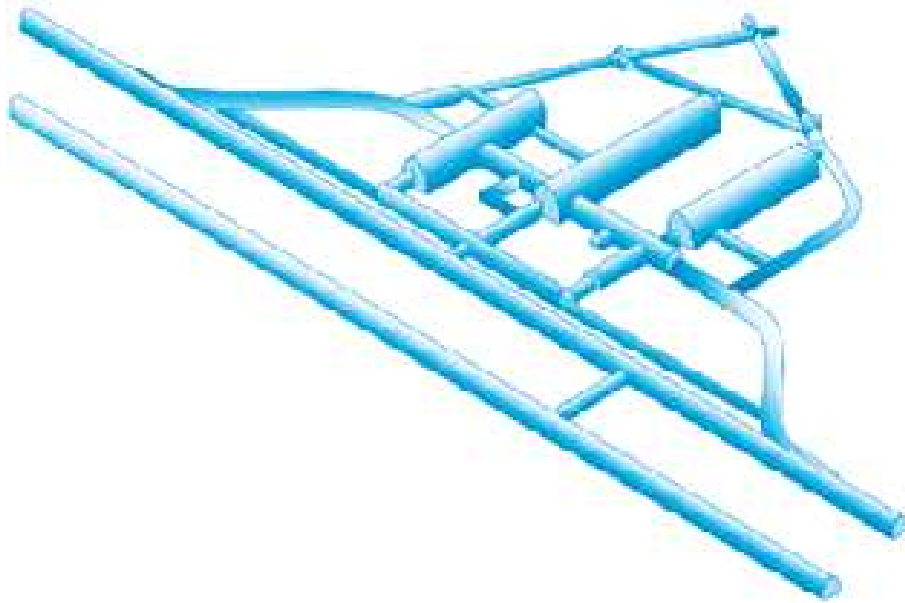


Figure 1.1: *Map of the underground laboratory.*

and 18 m high) for a total volume of about $180000 m^3$ (figure 1.1). The average 1400 m rock coverage gives a reduction factor of one million in the cosmic ray flux; moreover, the neutron flux from radioactivity is thousand times less than on the surface, thanks to the small content of Uranium and Thorium in the dolomite rocks of the mountain. On the surface a National Park hosts the external facilities of the laboratory as the laboratories of chemistry, electronic, mechanical, design and workshops, the Computing Centre, the Directorate and the various Offices. The LNGS is the biggest underground laboratory in the world built and dedicated to astroparticles physics and rare events.

1.1.1 Experiments and physics studied in the LNGS

The study of the intrinsic properties of neutrino is of prime interest in particle physics and one of the main research topics of the present scientific program of the Laboratory. Another main topics is represented by the search of the so called Dark Matter and the Gran Sasso National Laboratory is in the forefront of such studies [2].

Neutrino Physics

In order to study the mechanism of neutrino oscillations, it is necessary to measure the elements of the mixing matrix and this is the main goal of OPERA experiment, which aims to the detection of tau neutrinos in the artificial neutrino beam from CERN to Gran Sasso (CNGS), originally constituted by muon neutrinos only.

Borexino measures in real-time the interactions of solar neutrinos by means of a 300 ton sphere of scintillating liquid. This allows to study the functioning of the Sun and, at the same time, the neutrino properties.

The LVD experiment is continuously monitoring the Galaxy with its 1000 tons of liquid scintillator, looking for collapsing stars and it also offers an original monitoring of the CNGS neutrino beam. LVD participates in the SuperNovae Early Warning System of detectors.

Neutrinoless Double- β Decay

The study of neutrino properties through the research into a rare process called *neutrinoless double beta decay* may give a direct indication of the value of the ν mass, ascertaining its nature of Majorana particles (that is particle and antiparticle coinciding). At present LNGS is host to several experiments devoted to research neutrinoless double beta decay events.

The GERDA experiment will use the same enriched Germanium crystals of the Heidelberg-Moscow experiment, but they are directly immersed in 60 m^3 of liquid Argon, which acts as an active shield. They have built also a 10 m diameter tank all around the cryostat is a further protection and that acts as a veto Cherenkov for muons.

The CUORE experiment, after the success of CUORICINO, is the most recent and ambitious development of the TeO_2 *bolometers* technique. The mass of the crystals is about 740 kg and they are cooled at a temperature next to the absolute zero.

Finally there is the COBRA experiment, where the basic idea is to use $CdZnTe$ (CZT) semiconductors as detectors: they have a low radioactive background level, good energy resolution and operated at room temperature.

Dark Matter

Experimental evidence indicates the existence in the Universe of an amount of mass larger than the one observable by means of telescopes, called dark matter.

Its total amount is supposed to be five times the ordinary matter, which constitutes only 5% of our Universe. At LNGS four experiments are devoted to the hunt for dark matter candidates and their direct detection, using different technologies.

The DAMA/LIBRA experiment, made up of 250 *kg* of *NaI(Tl)* extremely radio-pure crystals, has been recording data since 2003. Results so far published have confirmed the annual modulation of very low energy signals induced in the detector. Such modulation is identical to the one expected from the Dark Matter particle flux.

WARP100 *lt* is a cryogenic detector that uses double phase argon and it is based on a double detection technique, the scintillation in liquid argon and the ionization in the gaseous state.

XENON100 is also a two-phase liquid cryogenic detector and the apparatus contains 170 *kg* of Xenon, 65 *kg* of which constitute the active part while the remaining ones act as a shield.

The CRESST experiment is based on the bolometer technique with *CaWO₄* crystals cooled at 10 *mK* as well as on the simultaneous detection of scintillation light and the heat resulting by the interaction of a particle with the crystals.

Nuclear Reactions

The solar models are based on data and extrapolations; in particular the thermonuclear cross sections of the involved reactions are not measured in the relevant energy range but rather extrapolated from higher energies. The direct measurements are made very difficult by the very low values of the cross sections. Using the new 400 kV accelerator, LUNA continued its activity for the measurements of the cross section of nuclear reaction of astrophysical interest.

Others

The Laboratory hosts experiments aimed to study cosmogenic and primordial radionuclides in solid and fluid matrix inside LNGS, and experiments of geophysical interest as well.

The activity of the theory group and of the staff and visitor scientists covers various aspects of astroparticle and particle physics, including Supernova neutrinos, ultra high energy cosmic rays, high energy neutrinos and cosmology, large scale structures and dark matter, phenomenology of Planck scale physics.

1.2 Origin of neutrons in the underground laboratories

The knowledge of neutron fluxes in underground laboratories is crucial in experiments searching for rare events: neutrino interactions, neutrinoless double-beta decay, proton decay and dark matter. For example, in dark matter searches, in order to reach 10^{-10} pb sensitivity to the WIMP-nucleon cross-section, the neutron flux produced by muons underground must be known and suitably attenuated. Neutrons in deep underground laboratories are produced in reactions initiated either by natural radioactivity or by cosmic rays. Neutron flux due to natural radioactivity (in the rock around the laboratory and/or in the materials of the experimental setup) is produced by spontaneous fission and (α, n) interactions of α 's from natural α -emitters ($E_\alpha < 10$ MeV) with light target nuclei. Neutrons from natural radioactivity have energy up to about 10 MeV. Neutrons are also produced in nuclear reactions induced by cosmic muons. These reactions can be caused by the muon itself or by secondary particles generated in muon-induced cascades in the rock or in the materials of the experimental setup. The energy spectrum of these neutrons is substantially harder compared to neutrons from radioactivity, because they can be emitted with energies up to a few GeV. The flux of neutrons from radioactivity of the experimental environment is two or three orders of magnitudes higher than the flux of neutrons from cosmic ray muons. Due to its very low intensity and harder spectrum, the muon-induced neutron flux underground is not easy to measure and represents the ultimate background that can limit the sensitivity of the over mentioned experiments.

1.2.1 Neutrons from natural radioactivity

The *ingredients* that are needed for the evaluation of the background induced in a given setup by neutrons from natural radioactivity are as follows [3]:

1. The chemical composition of the source material. The fractions of hydrogen and other light elements are particularly important because they affect in a substantial way the neutron production and/or propagation.

2. The contamination of the material mainly in ^{238}U , which undergoes spontaneous fission, and in α -emitters from the U and Th natural chains. This is important both for the total neutron production rate and for the neutron energy spectrum, because the (α, n) cross section is strongly dependent on energy.
3. The nuclear parameters of interest. For spontaneous fission they are the multiplicity, the half-life and the relevant branching ratio, while for the (α, n) interactions it is necessary to know the interaction cross-sections as a function of energy for all possible target isotopes that compose the material under investigation.
4. The propagation of neutrons from the production point to the sensitive volume, possibly through the external passive shield, and the neutron detection process.

The first three items are required to calculate the specific production rate of neutrons in the material under investigation. The last item is required to estimate the actual background rate in the detector, taking into account the detector properties.

Gran Sasso rock consists mainly of CaCO_3 and MgCO_3 , with a density of $2.71 \pm 0.05 \text{ g/cm}^3$. The weight percentage of the elements is given in table 3.2. Since there are no data on the chemical composition of Gran Sasso concrete available in literature, several samples were taken from different positions in the laboratories. The typical water content in the concrete is 12%, with a possible variation of 4% at most. The weight percentage of elements in concrete with 8% water content is shown in the same table 3.2 and the density is between 2.3 and 2.5 g/cm^3 , depending on the assumed water content.

There are mainly three nuclides in nature that undergo spontaneous fission: ^{238}U , ^{235}U and ^{232}Th . Because of the long fission half life of the last two nuclides, the ^{238}U is the responsible for this kind of reactions. The spectrum of the emitted

volume	hall A	hall B	hall C	concrete
^{238}U activities (ppm)	6.80 ± 0.67	0.42 ± 0.10	0.66 ± 0.14	1.05 ± 0.12

Table 1.1: ^{238}U activities in the LNGS rock and concrete.

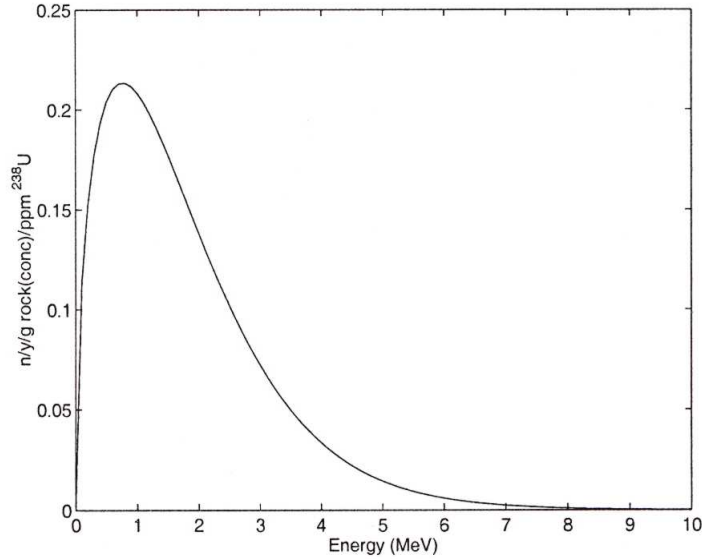


Figure 1.2: *Energy spectrum of neutrons from spontaneous fission of ^{238}U .*

neutrons follows the Watt spectrum:

$$N(E) = Ce^{-E/a} \sinh(bE)^{1/2} \quad (1.1)$$

where the Watt spectrum parameters of the Los Alamos model results [4] have been used: $a = 0.7124$ MeV and $b = 5.6405$ MeV $^{-1}$. The energy spectrum of neutrons from spontaneous fission of ^{238}U is shown in figure 1.2. The rate of spontaneous fission of ^{238}U is 0.218 fissions/years/g of rock (concrete) for 1 ppm of ^{238}U and the average number of neutrons emitted per fission event is 2.4 ± 0.2 [5]. This gives 0.52 neutrons/year/g of rock (concrete)/ppm ^{238}U . Multiplying this number with the activities in rock [6] and concrete [7], showed in table 1.1, it gives 3.54 and 0.55 neutrons/year/g in the rock of hall A and concrete respectively.

Uranium, Thorium and their daughter products decay by emitting α and β particles. In the rock and concrete α -particles can interact especially with light elements and produce neutrons through (α, n) reactions. The yield of neutrons per

α -particle for an individual element depends on the (α, n) interaction cross section, that depends on the energy, and on the energy loss of α -particles in a medium made of that element. The neutron yield of the (α, n) reactions for an individual element j in which the α -particle has a range R for thick target, can be written as [8]:

$$Y_j = \int_0^R n_j \sigma_j(E) dx \quad (1.2)$$

where n_j is the number of atoms per unit volume of element j , and σ_j is the microscopic (α, n) reaction cross section for an α -particle energy E . Transforming the right side of the last equation into an integral over energy gives:

$$Y_j = \frac{N_A}{A_j} \int_0^{E_i} \frac{\sigma_j(E)}{S_j^m(E)} dE \quad (1.3)$$

where E_i is the initial α -particle energy, N_A is Avogadro's number, A_j is the atomic mass and σ_j and S_j^m are the (α, n) cross section and the mass stopping power respectively, which are energy dependent. Neutron yields from individual elements can be used to calculate the total yield in a chemical compound or mixture, with the following assumption:

- the compound is a homogeneous mixture of its constituent elements.
- Bragg's law of additivity for stopping power holds for the compound.
- the ratio of an element's stopping power to the total stopping power of the compound is independent of the α -particle energy.

Under those assumptions the neutron yield of element j in the compound or mixture with initial α -particle energy E_i can be written as:

$$Y_{i,j,mix} = \frac{M_j S_j(E_0)}{\sum_j M_j S_j(E_0)} Y_j(E_i) \quad (1.4)$$

where M_j is the mass fraction of element j in the mixture, E_0 is a chosen reference energy, S_j^m is the mass stopping power and $Y_j(E_i)$ is the neutron yield of element j in isolation. Thus the (α, n) yield of a mixture is the sum of the yields of its elements

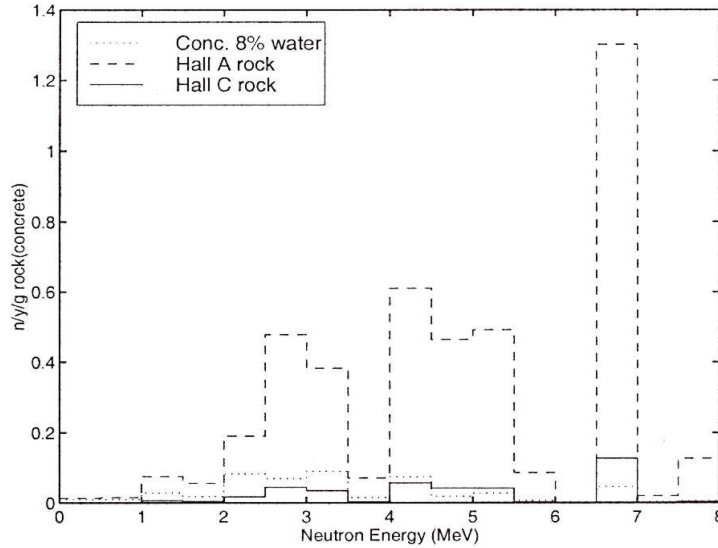


Figure 1.3: *Energy spectra of emitted neutrons from (α, n) reactions for hall A rock, hall C rock and concrete.*

weighted by the relative contributions of the elements to the total stopping power of the compound.

Each α emitter in ^{238}U and ^{232}Th decay chains emits α 's at a certain energy, which can be used as the initial energy in the neutron yield calculation. The neutron yield of each element with certain initial energy is then multiplied by the branching ratio, the number of α 's emitted by each emitter per unit time, and the concentration of ^{238}U and ^{232}Th in the rock and concrete. In the work [4], the total neutron production rate for each element has been calculated by summing up the contribution of all α emitters and under the assumption that ^{238}U and ^{232}Th are in secular equilibrium with their daughter products. In this work they find out that half of total (α, n) neutron production in the rock comes from interactions of α -particles with magnesium, which comprises only less than 6% of the weight percentage of the rock, whereas oxygen with almost 50% weight percentage contributes to only about 20% of the production rate. Due to the higher

activity of the hall A rock the (α, n) neutron production in the rock of this hall is more than 10 times higher than in the hall C rock. In the concrete Na, Al and Mg contribute significantly in spite of their minor weight percentages. The energy of the emitted neutron is dependent on the α energy, the reaction energy Q and the neutron emission angle. It was calculated under the following assumption:

- the interaction take place at the initial α energy
- the neutron is emitted at 90°
- the residual nucleus is produced in its ground state

Under these assumptions, the neutron energy can be determined by using the following equation:

$$E_n = \frac{MQ + E_\alpha(M - M_\alpha)}{M_n + M} \quad (1.5)$$

where M is the mass of the final nucleus, M_n and M_α are the masses of neutron and α -particle respectively, and E_α is the initial α energy. The threshold energy E_{th} for (α, n) reaction is the minimum kinetic energy the impinging α -particle must have in the laboratory system in order to make the reaction energetically possible and it can be obtained with the following:

$$E_{th} = -Q \frac{M_n + M_\alpha}{M_1} \quad (1.6)$$

where M_1 is the mass of the target nucleus. Finally, the yields of all elements were summed up and the energy spectra of neutrons from (α, n) reactions is showed in figure 1.3. Neutrons with energy higher than 1 MeV come mainly from a maximum depth of 7 and 13 centimeters of concrete and rock respectively. As the thickness of the concrete layer at the Gran Sasso is not less than 30 cm, the bulk of the total flux at the laboratory is given by neutrons produced in the concrete.

1.2.2 Muon-induced neutrons

The other important neutron source in underground laboratories are cosmic ray muons and muon-induced cascades. Since neutron flux is proportional to the residual muon rate at the underground site, this background can be reduced by

going deeper and deeper. In order to increase as much as possible the experimental sensitivity, it is important to estimate precisely the expected neutron flux induced by muons in the existing underground laboratories and to optimize the suppression of this background.

A theoretical investigation of the neutron flux associated with muons underground is a manysided problem that involves determining the muon spectrum at a given depth, considering processes via which muons initiate hadron and electromagnetic showers in matter and studying the properties of neutron transport in rock and in the detector material, as well as taking into account the geometry of the detector. The required *ingredients* for calculating the muon-induced neutron flux are as follows:

1. the total muon flux at the underground site
2. the energy spectrum and the angular distribution of muons.
3. the code to track muons and their interactions, as well as production, propagation and possible detection of all secondaries, including neutrons.

The first two items simply represent an input for the Monte Carlo tracking of primary muons. The third item is the most critical because it involves the modelling of the hadronic and electromagnetic interactions in a muon-induced particle shower.

The total muon flux is a specific parameter that characterizes each underground site, and is known experimentally. The residual muon flux at the Gran Sasso laboratory is about $1.17 \mu/(\text{m}^2 \text{ hour})$ [9], [10],[11].

For laboratories located under mountains, the energy-angular distribution is determined by the structure and the orography of the region, while for laboratories that are made in mines have a more homogeneous shielding profile. Information about energy and angular distribution can be obtained by experimental measure or by Monte Carlo simulation. Several fast dedicated codes like MUSIC [12], are able to track muons from the surface of the mountains down to the underground laboratory. Another code MUSUN [13] can be used to generate muons according to their angular and energy distribution (already got with MUSIC) underground.

The average muon energy increases with the site depth and for the Gran Sasso laboratory it is about 270 GeV.

Muons that reach the underground laboratories can induce neutrons by two ways:

- **directly** with the interaction of muons and nuclei with the production of radioactive isotopes and the spallation process.
- **indirectly** with muons that induce electromagnetic and hadron showers.

The contribution of either group to the total neutron yields depends on the average muon energy at a given depth.

Directly generated neutrons are largely produced in two processes: the capture of negative muons by nuclei and photonuclear reactions. The first process is dominant up to a depth of about 80 m w.e. ($\bar{E}_\mu \sim 30$ GeV), contributing about 50% to the total neutron yield at this depth, while at a depth of about 1000 m w.e. ($\bar{E}_\mu \sim 160$ GeV) the contribution of this process is reduced to few tenths of percentage [14]. Muons which stop and are captured, can generate highly excited isotopes emitting one or more neutrons, as described by the following reaction:



In this reaction the muon can be considered at rest, thus the energy exchanged in the process is equal to the muon mass and it is shared between the outgoing neutrino and the excitation energy of the nucleus. If the energy left to the nucleus is high, neutrons are evaporated and the nucleus goes down to the ground state, otherwise for lower excitation energies the nucleus can de-excite with emission of photons. Neutrons originated from muon capture have low energies with an average of about 8 MeV.

The muon spallation process is schematically illustrated in figure 1.4, with the exchanging of a virtual photon. This process of muons with nuclei is important at high muon energies ($E \geq 10$ GeV), and at relatively high energy transfers ν ($\nu/E \geq 10^{-2}$) and it is especially important for light materials. The average energy loss for this process increases almost linearly with energy, and at TeV muon

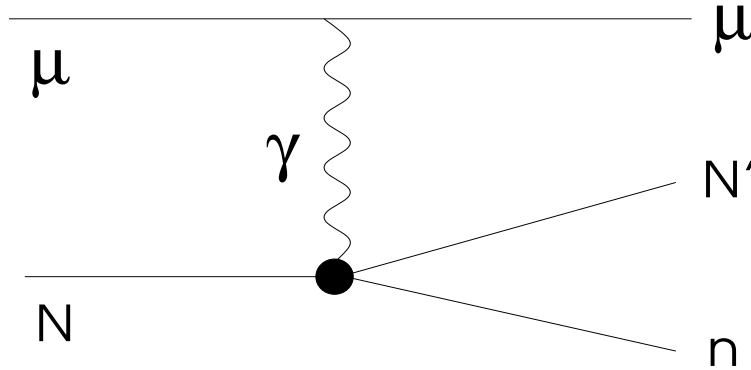


Figure 1.4: *The Feynman diagram of a muon spallation process.*

energies constitutes about 10% of the energy loss rate. Theoretical calculations often treat the virtual photons according to the Weizsacker-Williams approximation [15], in which the passage of a charged particle in a slab of material produces the same effects as of a beam of quasi-real photons. In that approximation, it is assumed that the $\gamma - N$ cross section is the same for real and virtual photons. At low muon energy the situation is more complicated. Here, the virtuality of the photon becomes comparable to its energy and cannot be neglected. In addition, the interaction of virtual photon with the nucleus is a collective excitation of the nucleus rather than a single photon-nucleon interaction. However, it might be reasonable to assume that neutron production by low-energy muon interactions is small as compared to neutron photoproduction by low-energy bremsstrahlung photons and adds therefore only a minor contribution to the total neutron yield.

Chapter 2

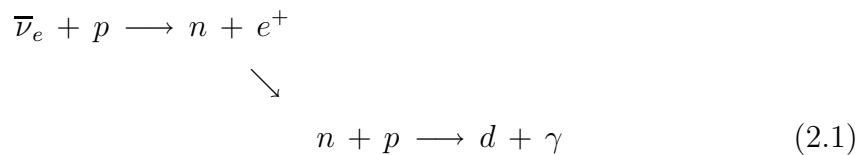
The LVD detector

The LVD detector, operating since 1992, is a multipurpose detector consisting of 1000 ton of liquid scintillator. LVD is able to reconstruct cosmic muons crossing the detector and neutrons: that provide a valid way to measure muon-induced neutrons.

This chapter introduces the concept and design of the LVD detector. After a brief description of the detector setup, DAQ and electronics presented in section 2.1 and 2.2, respectively, in section 2.3 is described the detector energy calibration and resolution. In section 2.4 are shown the Physics items studied in LVD and in the last section 2.5 the current status of the detector will be summarized.

2.1 Detector description

The Large Volume Detector (LVD), built in the INFN Gran Sasso National Laboratory, at the depth of 3600 m w.e., is a 1 kt liquid scintillator detector whose major purpose is monitoring the Galaxy to study neutrino bursts from gravitational stellar collapses [16] by the characteristic signature of the inverse *beta*-decay:



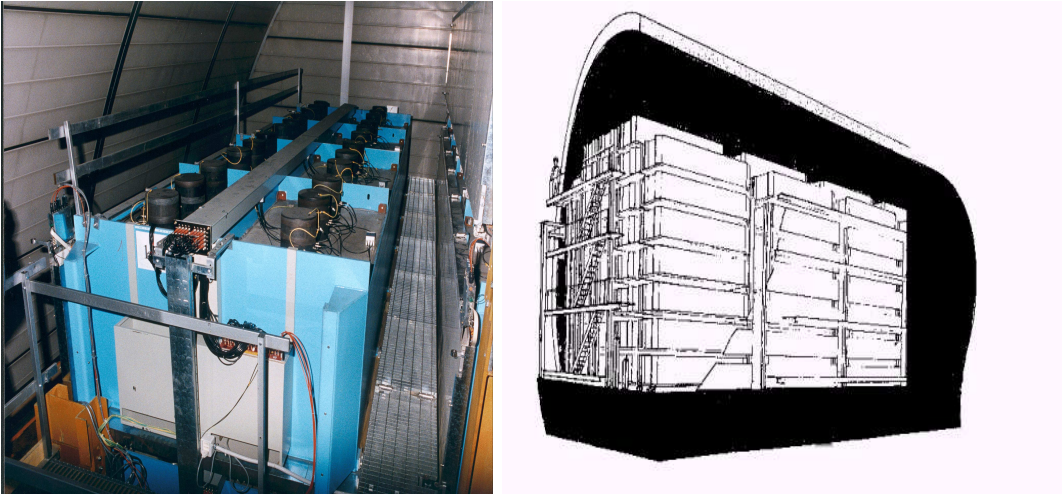


Figure 2.1: (left): A single portatank constituted of 8 scintillation counters. (right): A pictorial view of the whole LVD detector.

where an electron antineutrino interacts with a proton in the liquid scintillator originating a positron that gives a prompt signal and a neutron that will be slowed down to thermal energies ($1/40$ eV) in about $185 \mu\text{s}$ and then captured by a proton releasing a γ -capture of 2.23 MeV. In the next section we will show how the electronics employed has been optimized to pick out both signals.

Thanks to its high modularity, the experiment has been taking data, under different configurations, since 1992 when the detector construction started. The current configuration was finally reached in 2001. The detector is divided in 3 towers (5 columns and 7 levels), showed in figure 2.1 *right* each tower has 35 modules, called *portatank* and showed in figure 2.1 *left*, that contain 8 counters or tank. Over the seventh level of the three middle columns there is an additional level of switched-off modules (the number of modules are overall 114 for each tower). The eighth level modules are not connected to the electronics and they are used as a shield for the rock radioactivity. Formerly, every module was equipped by two streamer tubes for tracking muons but they were switched-off in 2002. The stainless steel thickness of the counters is ~ 0.4 cm and its composition is showed in section 3.2.5. Each counter is filled with 1.2 ton of liquid scintillator: the basis is an hydrocarbon (C_nH_{2n} where $\bar{n} = 9.6$) with 1 g/l of scintillation activator

PPO and 0.03 g/l of wavelength shifter POPOP added. The liquid scintillator has a density $\rho = 0.78 \text{ g/cm}^3$, a decay time of $\sim 5 \text{ ns}$ and an estimated attenuation length of $\lambda \geq 16 \text{ m}$. To increase the internal reflectivity, the counters are internally coated by an aluminated mylar film with reflection coefficient of about 0.92. The scintillator contained in a counter is monitored by three photomultiplier tubes (PMTs) from the top surface that watch inside the tank through a cylindrical plexiglass light guide with a thickness of 7 cm and a diameter of 19 cm. In order to avoid the scintillator ageing, an argon atmosphere has been put into the counter and the thickness is about 4 cm. The total amount of liquid scintillator in the detector, about 1 kton, is used as a sensitive target for neutrinos, but the iron support structure (1 kton) can also act as target for neutrinos and antineutrinos. The external dimensions of the active volume are $13 \times 23 \times 10 \text{ m}^3$ and in figure 2.2 is showed the detector installed in the hall A.

2.2 DAQ and Electronic description

When the reaction 2.1 occurs in the detector, an e^+ gives a prompt signal and the originated n, slowing down to thermal energies, is captured by a proton in the liquid scintillator. In order to reduce the cosmic ray contribution to the background, this kind of detector are always placed deep underground and is requested to continuously run with minimum dead time, large active mass and absolute timing [17]. An electronic system matching all these requirements with a very high modularity has been developed expressly for LVD. The system consists of two modules: C175 and C176. The first module provides the trigger to the whole system while the second one provides the charge and time-to-digital conversions and the data storage into the internal memory buffer [18].

The C175 module, assembled in a CAMAC double unit, contains 8 independent channels to serve each counter of the portatank and each channel has 3 inputs, one for each PMT. The signals from the 3 PMTs of a counter are amplified and discriminated with threshold: an high one (HET) that can have a value between 31 and 219 mV and a low one (LET) ranging from 15 up to 78 mV. These voltages correspond to an energy threshold of $\varepsilon_H \simeq 5 \text{ MeV}$ for the HET signals and $\varepsilon_L \simeq 1 \text{ MeV}$ for the LET signals. The double threshold system has been developed to



Figure 2.2: *The LVD detector, front view.*

detect both the positron and neutron capture signals from the inverse β -decay: when an HT signal is detected in a counter, the low threshold is enabled for a time gate of ~ 1 ms in all the counters of the same portatank. The 3 signals are summed, amplified and sent to the C176 with a logical flag (0 if the signal has passed the low threshold and 1 if it has passed the high threshold) and the GATE flag, that gives also the start to the charge integration gate of the ADC.

The C176 module, assembled in a CAMAC double unit as well, allows to measure the charge and the digitization of the arrival time of an input pulse. Eight completely independent channels are present. The events are stored in a FIFO

memory shared between the channels. The charge is converted by two 8 bit flash ADCs, each with 4 linearity zones so that the dynamic resolution of the charge converter is 12 bits. This electronic solution has been designed to have high resolution at low energies and, simultaneously, to have a wide dynamic range. The signal is integrated in a gate of about 250 ns and the time needed for the total charge conversion is 525 ns. Then 600 ns are needed to write the digitized data in memory and the total dead time is 1.125 μ s. The time measurement is carried out by a 29-bit TDC with a maximum resolution of 12.5 ns. The total conversion time is 800 ns. All this information is recorded on a 48 bits word in the FIFO memory of the C176 module and the FIFO contains a maximum of 512 words.

The electronics of each tower is connected to the tower CPU by a Branch Highway Camac Bus. When the acquisition system starts to record a high threshold event, a tower trigger subsystem is ready to generate an interrupt to the tower CPU to awaken the read-out process. Once the event is completely stored in the FIFOs, it is read by the tower CPU. The 3 independent DAQ CPUs of the towers are connected to a control system computer that periodically collects the data from the tower CPUs, correlates in time the events from different tower (program called BUILDER) and writes the final raw data on disk.

2.3 Energy calibration and resolution

The energy calibration of linear ADC channels is made by using cosmic muons detected by LVD. A muon event is defined as an event which has registered two or more high threshold signals in time coincidence within 250 ns. A simulation which considers the muon flux characteristics and the geometrical acceptance of the detector states that the muon mean path length in a counter is about 70 cm and that the mean energy released in a tank has a value of 185 MeV. By means of an automatic procedure, every month an energy calibration is performed fitting the muon spectrum in adc channels to get the muon peak mean value and assigning it the value carried out by the simulation. With this procedure all counters are calibrated in energy every month.

The energy resolution of the experiment, showed in figure 2.3, is mainly due to two factors:

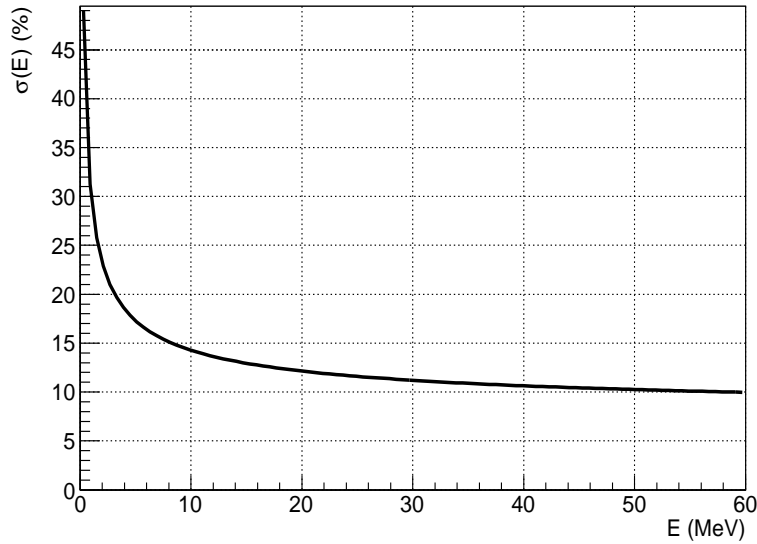


Figure 2.3: *LVD energy resolution.*

- geometrical, due to the light collection on PMTs and it depends on the geometrical characteristics of the counter and not on the energy.
- statistical, due to fluctuation in the number of photoelectron induced in the PMTs photocathode

These factors are represented, respectively, by the first and the second term of the following [23]:

$$\frac{\sigma}{E} = 0.07 + \frac{0.23}{\sqrt{E/MeV}} \quad (2.2)$$

2.4 Physics studied in LVD

The LVD detector main goal is the detection of neutrino bursts from supernova in our galaxy and the study of the early phases of the stellar collapse. Strictly connected to the supernova Physics, there is the Neutrino Physics because the signal observable in LVD in different channels is sensitive to intrinsic neutrino properties and can define some of the neutrino oscillation properties still missing.

LVD is well suited for reconstruction of the cosmic muon crossing the detector and so it offers a valid way to investigate the cosmic rays Physics underground. Another important study is the muon-induced neutrons flux because it represents the ultimate background for all the experiment located at LNGS that are searching for rare events and dark matter.

2.4.1 Detection of supernova neutrinos

The trigger logic is optimized for the detection of both products of the inverse beta decay, equation 2.1, and is based on the three-fold coincidence of the PMTs of a single counter. The amount of neutrino-iron interactions can be as high as about 20% of the total number of interactions. The observable neutrino reactions in the LVD scintillator are:

- $\bar{\nu}_e + p \rightarrow e^+ + n$, (physical threshold $E_{\bar{\nu}_e} > 1.8$ MeV) observed through a prompt signal from e^+ above ε_H , followed by the neutron gamma capture on proton above ε_L with a mean delay $\Delta t \simeq 185 \mu\text{s}$.
- $\nu_e + {}^{12}\text{C} \rightarrow {}^{12}\text{N} + e^-$, (physical threshold $E_{\nu_e} > 17.3$ MeV) observed through two signals: the prompt one due to the e^- above ε_H , followed by the signal, above ε_H , due to the β^+ decay of ${}^{12}\text{N}$ with a mean life $\tau = 15.9$ ms.
- $\bar{\nu}_e + {}^{12}\text{C} \rightarrow {}^{12}\text{B} + e^+$, (physical threshold $E_{\bar{\nu}_e} > 14.4$ MeV), observed through two signals: the prompt one due to e^+ and the second one, above ε_H , from the β^- decay of ${}^{12}\text{B}$ with a mean life $\tau = 29.4$ ms.
- $\bar{\nu}_l^{(-)} + {}^{12}\text{C} \rightarrow \bar{\nu}_l^{(-)} + {}^{12}\text{C}^*$ with $l=e,\mu,\tau$, (physical threshold $E_{\nu} > 15.1$ MeV) whose signature is the monochromatic photon from carbon de-excitation of 15.1 MeV, above ε_H .
- $\bar{\nu}_l^{(-)} + e^- \rightarrow \bar{\nu}_l^{(-)} + e^-$, which yields a single signal above ε_H due to the recoiling electron.

The higher energy part of the neutrino flux can be detected also with the $\bar{\nu} + Fe$ interaction, resulting in an electron (positron) that may exit the iron structure and release energy in the liquid scintillator. The reactions are:

- $\nu_e + {}^{56}\text{Fe} \rightarrow {}^{56}\text{Co} + e^-$
- $\bar{\nu}_e + {}^{56}\text{Fe} \rightarrow {}^{56}\text{Mn} + e^+$

For these reactions the efficiency for electron and gammas to reach the scintillator with energy higher than ε_H is greater than 20% for $E_\nu > 30$ MeV and grows up to 70% for $E_\nu > 100$ MeV. With these characteristics and detectable neutrino interactions, LVD can provide astrophysical parameters of the supernova explosion mechanism, up to now not well defined, such as the total energy emitted in neutrinos, the star distance, the neutrino-sphere temperatures and the partition of the energy among the neutrino flavours.

The search for ν bursts is performed by studying the temporal sequence of triggers and looking for clusters. No candidates have been found since 1992. Since the LVD sensitivity is higher than expected from GSC models (even if the source is at a distance of 20 kpc and for soft neutrino energy spectra), the resulting 90% c.l. upper limit to the rate of gravitational stellar collapses in the galaxy ($D \leq 20$ kpc) is 0.15 y^{-1} .

The first and unique observation of neutrinos from a stellar collapse was guided by the optical observation and since the optical observation of supernova in our galaxy has a 20% of probability a system is needed to demonstrate the detector capabilities of identifying a neutrino burst. In the presence of an electromagnetic counterpart, on the other hand, the prompt identification of the neutrino signal could alert the worldwide network of observatories allowing study of all aspects of the rare event from its onset. The SNEWS (SuperNova Early Warnings System) project [19] is an international collaboration including several experiments sensitive to a core-collapse supernova neutrino signal in the Galaxy and neighbourhood. Its goal is to provide the astronomical community with a prompt and confident alert of the occurrence of a galactic supernova event, generated by the coincidence of two or more active detectors. In July 2005, after a few years of tuning, the charter members (LVD, Super-K and SNO, before decommissioning) of SNEWS together with the newly joined Amanda/IceCube, started the effective operation of the network. The corresponding detection efficiency are shown in figures 2.4 and the details are described in reference [20].

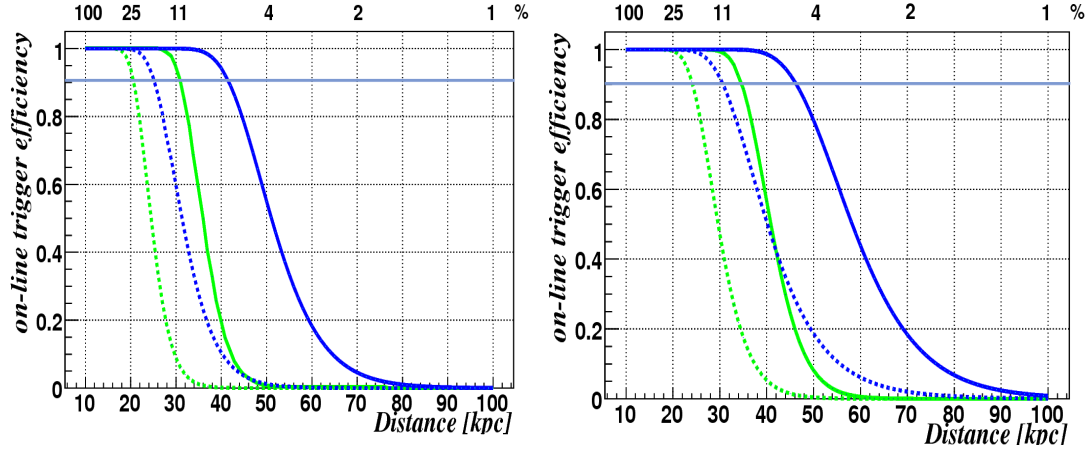


Figure 2.4: *On-line trigger efficiency versus distance (lower scale) and percentage of SN1987A signal at 10kpc (upper scale) for $E_{cut} = 7 - 10$ MeV (light green and dark blue lines, respectively) and $M = 300 - 1000$ t (dotted and continuous lines, respectively) for LVD stand alone (left) and for LVD in the SNEWS (right).*

2.4.2 Neutrino oscillations

The signal observable in LVD, in different reactions and due to different kinds of neutrinos, besides providing astrophysical information on the nature of the collapse, is sensitive to intrinsic neutrino properties, as oscillation of massive neutrinos and can give important contribution to define some of the neutrino oscillation properties still missing.

There are many experimental works suggesting neutrino conversions among flavours in the recent few years, through the study of atmospheric, solar, reactor and accelerator neutrinos. In the standard three flavour scenario, six parameters must be determined by oscillation experiments: 3 mixing angles (θ_{sol} , θ_{13} and θ_{atm}), 2 squared mass differences (Δm_{sol}^2 and Δm_{atm}^2) and 1 CP-violation phase δ . The available experimental data constrains the *atmospheric* and *solar* parameters to be in the following 99% c.l. ranges:

$$\begin{aligned}\Delta m_{sol}^2 &= (7.2 \div 8.9) \times 10^{-5} \text{ eV}^2 \\ |\Delta m_{atm}^2| &= (1.7 \div 3.3) \times 10^{-3} \text{ eV}^2 \\ \theta_{sol} &= 30^\circ \div 38^\circ \\ \theta_{atm} &= 36^\circ \div 54^\circ\end{aligned}$$

However the other parameters are not completely determined: the θ_{13} mixing angle is only upper limited, mainly by the Chooz experiment data ($\sin^2\theta_{13} < 3 \times 10^{-2}$ at the 99% c.l.), the sign of Δm_{atm}^2 , that fixes the so-called mass hierarchy, is completely unknown, as well as the CP-violation phase δ . Because of the wide range of matter density in the stellar envelope, a supernova explosion represents a unique scenario for further study of the neutrino oscillation mixing matrix. Indeed neutrinos can cross two resonance density layers and therefore the resulting possible mixing scenarios are different from the solar ones. The emerging neutrino spectra are sensitive to the sign of Δm_{atm}^2 and to the value of θ_{13} . The expected signal of neutrinos in LVD detector from a supernova core collapse greatly benefits of the neutrino oscillation mechanism, practically in all the possible detection channels, especially in the case of an adiabatic transition and the inverted hierarchy. More details about how neutrino oscillations affect the signal detected in LVD have been studied in reference [21].

2.4.3 Monitor of the CNGS beam

The Cern Neutrino to Gran Sasso (CNGS) project is a high energy, wide band ν_μ beam set up at Cern and sent towards the LNGS. Its main goal is the observation of the ν_τ appearance, through neutrino flavour oscillation. As shown in [22], due to its large area and active mass, LVD can act as a beam monitor, detecting the interaction of neutrinos inside the detector and the muons generated in the rock upstream the detector.

The CNGS events in LVD can be subdivided into two main categories:

- ν_μ charged current (CC) interactions in the rock upstream the LNGS; they produce a muon that can reach LVD and be detected.
- ν_μ CC and neutral current (NC) interactions in the material (liquid scintillator and iron of the support structure) of LVD.

A full Monte Carlo simulation has been developed and the expected events at the nominal intensity of 4.5×10^{19} p.o.t./y corresponds to ~ 165 CNGS events per day: 78% are muons from the rock, 17% are CC interactions in the detector and 5% are NC.

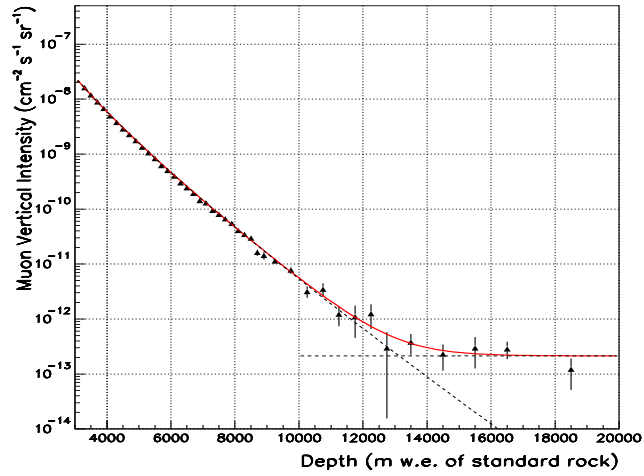


Figure 2.5: *Depth-vertical-muon-intensity curve in standard rock.*

2.4.4 Cosmic rays

The average 1400 *m* rock coverage at the LNGS underground laboratory gives a reduction factor of one million in the cosmic ray flux. The residual muon flux is about $1.17 \mu/(\text{m}^2\text{hour})$ and that let to study the cosmic rays. The main topics are:

- the muon depth-intensity relation
- the high energy muon spectrum in Extensive Air Shower
- seasonal modulation of the cosmic muon flux
- coincident events between the OPERA and LVD detector

During the past years the cosmic ray muon energy spectrum has been studied in many experiments using different methods and one of these is the measurement of the depth-intensity curve deep underground. With the knowledge of the Gran Sasso mountain profile, the angular distribution of muon intensity measured by LVD has been converted to the depth-vertical-muon intensity relation. In figure 2.5 it is showed the muon vertical intensity versus the rock thickness crossed by muons and two components are evident. The first is dominant at depth up to 13 km w.e. of standard rock due to cosmic muons originated by pions and kaons in

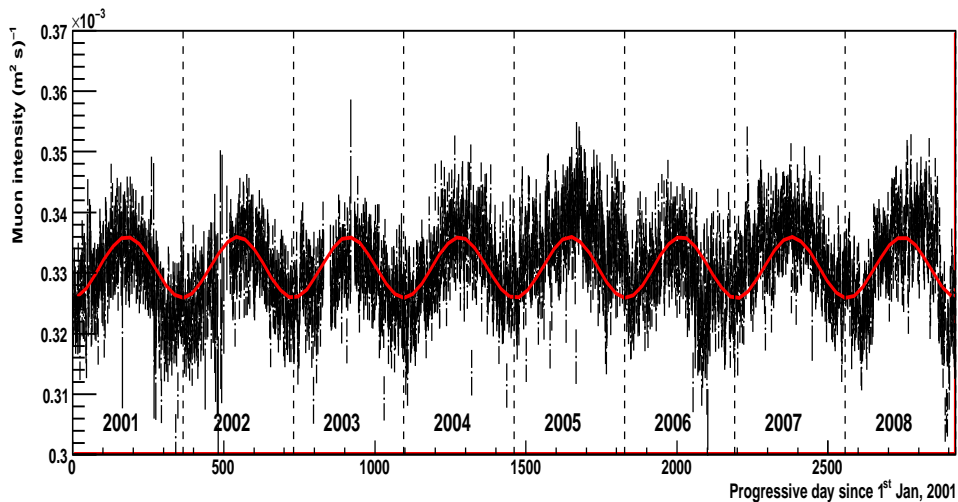


Figure 2.6: *Muon intensity along the 8 years of data acquisition. Each bin corresponds to one day and the solid red curve is the result of a cosinusoidal fit to the data.*

the atmosphere. The second one is due to horizontal muons induced by neutrino interaction in the rock surrounding the experimental hall. More details in reference [9].

A task in the study of cosmic rays above 10^{14} eV from ground based observation consists of the separation of primary composition from high energy interaction effects. Measurements on high energy secondaries represent important tools for such purpose since they are produced in the first interactions and therefore not subject to the processes of cascade development. Moreover, their energy distribution in the high energy tail is subject to the kinematical cutoff $E_s^{max} < E_0/A$ which makes this observable sensitive to the primary composition. This sensitivity is most effectively displayed when muon energy is correlated to shower size measurements. The analysis is summarized in reference [24] where emerges that the LVD detector is sensitive to the increase of the average muon energy with shower size and that the measured relation between the average muon energy loss in the LVD detector and shower size measured at the surface by EAS-TOP reflects the mixed character of the cosmic ray primary composition.

It is well known that the flux of cosmic muons underground is related to the temperature of the Earth atmosphere (the higher the temperature, the higher the muon flux underground) because the change in the air density implies a variation in the decay and interaction rate of the parent mesons. This effect has been previously measured by various experiments deep underground but only for few years. LVD data starting in January 2001 and ending in December 2008 has been analyzed and the total number of muons in the full data is greater than 20 million. The muon intensity measured day by day since 2001 is showed in figure 2.6. A modulation is clearly visible and fitting with a cosinusoidal function, the period $T = (367 \pm 15)$ days is compatible with one year, the phase $t_0 = (185 \pm 15)$ days correspondes to a maximum intensity at the beginning of July and minimum at the beginning of January and with an average amplitude of 1.5%. More details about these results can be found in reference [25].

The relative position of the OPERA and LVD detector, both at LNGS and separated by an average distance of 170 m, allows an unprecedented analysis of very large cosmic ray showers looking at their penetrating TeV component. The physics case follows the consideration that TeV muons separated by hundreds of meters are produced in high p_T interactions up in the atmosphere ($p_T > 3$ GeV) where perturbative QCD can be applied. One can therefore relieve the interpretation of cosmic ray data from phenomenological models usually adopted to describe the bulk of soft processes occurring in cosmic ray showers. Data of 2008 have been analyzed and 183 events have been found, which 145 from CNGS events 38 out of the CNGS spill window. Indeed, these last events do not represent different muons that cross both detector in time coincidence but represent the same muon coming from the so-called *Teramo valley*, where the mountain profile exhibits a small rock depth even for horizontal directions.

2.4.5 Other topics

Other topics under investigation are about the long-term study of low energy counting rate and the study of muon-induced neutrons. The latter represents the main subject of this thesis and will be checked in chapter 6.

The single counter rate at the low energy threshold (LTCR) is measured by a

system of 840 scalers enabled, every 10 minutes for 10 s, by a dedicated trigger, designed for monitoring purpose. The rate per counter is around 50 Hz, and it is mainly due to to gammas from rock radioactivity and decays of radon products. To study the long-term behavior of the low-energy counting rate it has been taken into account scaler data between 1997 and 2009 and only the counters that shows a stable behavior versus time. The data recorded by an alpha radon-meter located just inside the LVD experiment and the LTCR are correlated. As highlighted by other authors [26], the radon concentration in the laboratory strongly depends on the conditions of the ventilation system and there is an anti-correlation between pressure and radon emanation from rock in caves. To study long-term modulations in the counting rate, it has been considered only the period after the beginning of 2003 and, when the counting rate was more homogeneous. The data are well fitted by a sinusoidal function and the seasonal modulation shows the maximum at day 241 ± 32 , corresponding to the end of August and is consistent with the one found by the radon-meter inside LVD. The details of the analysis are discussed in reference [27].

2.5 Detector status

LVD has been taking data since June 1992 with increasing mass configurations (sensitive mass being always greater than 300 t), enough to monitor the whole galaxy ($D \leq 20$ kpc). The final configuration was achieved in the January of 2001 with 1 kt of active mass. The neutrino burst from a supernova is a very rare and short event: the supernova rate expected in the galaxy is about $1 \div 3$ per century and neutrino burst is expected to be 20 s wide. Thus for its detection it is crucial to have a big active mass and a high duty cycle, and LVD meets both requirements as showed in figures 2.7 red and black lines respectively. During the period 2001-2010 the sensitive mass of the experiment has been greater than 900 t and the LVD duty cycle, in the same period, greater than 99.5%.

In the last years we have investigated possible upgrades of the detector. In particular we studied:

- the possibility to improve the detector capability in distinguish different neu-

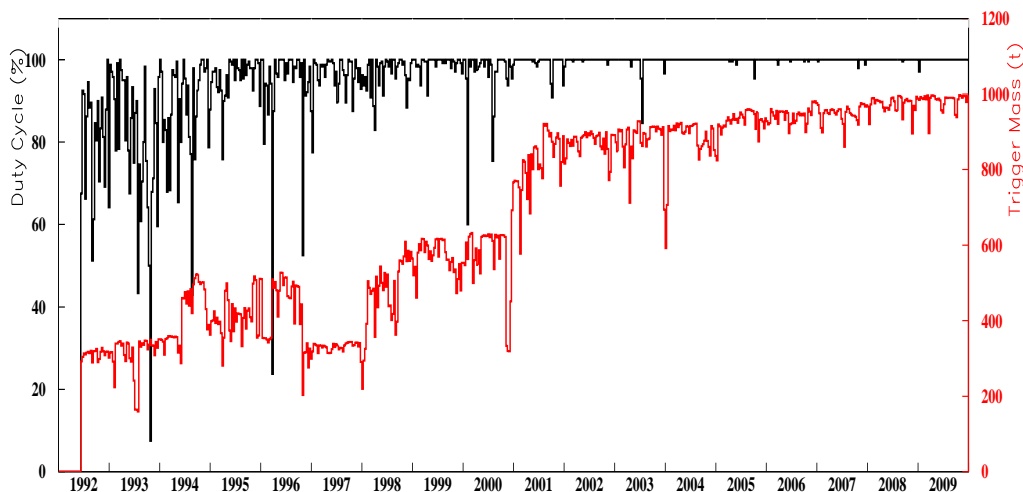


Figure 2.7: *LVD sensitive mass (red line) and duty cycle (black line).*

trino interactions by adding Gd to the liquid scintillator.

- the performance of the LVD detector as a powerful active shielding and veto with respect to an internal region that we called *core facility* (LVDcf).

Doping the liquid scintillator with a small ($\sim 0.15\%$ in weight) quantity of Gd definitely improves the performance of the LVD tank in the neutron detection, because Gd has a huge cross section for n-capture due, essentially, to the two isotopes ^{155}Gd and ^{157}Gd ; in particular the mean n-capture time results to be $\tau < 23 \mu\text{s}$, 8 times shorter than the one obtained with undoped liquid scintillator. Moreover n-captures on Gd generate a gamma cascade up to about 8 MeV to be compared with the 2.23 MeV of gamma quanta from (n,p) capture. Accordingly, Gd could increase the signal to noise ratio of a factor of several hundreds maintaining the present neutron capture detection efficiency, simply increasing the energy for neutron detection and shortening the time window for the coincidence. These results are described in reference [28].

It is well known that the muon-induced fast neutrons limit the possibility of searches for rare events, like neutrinoless double beta decay or WIMP dark matter

interactions. An inner region inside the LVD structure (LVDcf) has been identified with a volume of about 30 m^3 : its realization causes a negligible impact on LVD operation and sensitive mass. The LVDcf could be effectively exploited by a compact experiment for the search of rare events, such as double beta decay or dark matter. It has been evaluated the shielding power of LVD working both as an active veto for muons inducing high energy neutrons, with a dedicated simulation that is a part of this thesis and will be showed in section 5.1 and as a passive shield and moderator for the low energy gamma [29] and neutron background [30]. The results are summarized in reference [31].

Chapter 3

Monte Carlo simulation programs

The aim of this thesis has been the building and developing of a full Monte Carlo simulation (LVDG4) of the LVD detector. This simulation has been based on Geant4 toolkit.

After a brief historical introduction about the several simulations toolkit that are around given in section 3.1, in section 3.2 are presented the structure of the built simulation. Finally in section 3.3 the validation of the physics list used in the simulation will be presented.

3.1 Historical introduction

The Monte Carlo method is an application of the laws of probability and statistics to the natural sciences. The essence of the method is to use various distributions of random numbers, each distribution reflecting a particular process in a sequence of processes. Statistical sampling had been known for some time, but without computers calculations were really hard to make. The advent of computers made the approach extremely useful for many physics problems [32].

During the Second World War, a team of scientists, engineers and technicians was working on the first electronic computer: the *ENIAC*. In the same period John von Neumann was interested in the thermonuclear problem and with S. Frankel and N. Metropolis prepared a preliminary computational model of a thermonuclear reaction for the *ENIAC*. In the spring of 1946, with the contribution of E.

Fermi, A. Turkevich and E. Teller was released a review of the *ENIAC*, the calculations and conclusions about the feasibility of a thermonuclear weapon. Among the attendees there was S. Ulam and he was duly impressed by the speed and versatility of the *ENIAC*. In addition his mathematical background made him aware that statistical techniques had fallen into desuetude because of the length and tediousness of the calculation, but with these electromechanical computers that techniques should be resuscitated. He discussed this idea with von Neumann and thus was triggered the spark that led to the Monte Carlo method [33]. However Fermi was one of the first to use the Monte Carlo method, in a rather simple form and hand-calculated, long before it had a name. He was interested in neutron diffusion and he used this method for studying the neutron moderation and interactions. He persuaded also P. King to build an *analog* device to implement studies in neutron transportation, later called *FERMIAC*. In 1949, Metropolis published the first public document on Monte Carlo simulation with Ulam and introduced, among other ideas, Monte Carlo particle methods, which form the basis of modern Monte Carlo methods. In early 1952 a new computer, the *MANIAC*, became operational at Los Alamos and soon after A. Turkevich led a study of the nuclear cascades that result when an accelerated particle collides with a nucleus. In this study the particles were followed until all particles either escaped from the nucleus or their energy dropped below some threshold value. In the late 50's and 60's, the method was tested in a variety of ways, but many problems remained unsolved through the seventies until the advent of high-speed supercomputers.

The Monte Carlo methods are especially useful in studying systems with a large number of coupled degrees of freedom, such fluids, disordered materials, solid, and nowadays they are widely used in a lot of different fields like engineering, finance and business, telecommunications, biology, games and so on. In experimental particle Physics, these methods are used for designing detectors, understanding their behavior and comparing experimental data to theory. For this purpose several toolkit have been developed to describe the particle transportation and interaction through the matter. Some of them are very specialized in the description of a particular class of particles or interactions and they are used only in specific fields, while others are more generic without losing accuracy and are used for designing large detectors where can be produced every kind of particles and every kind of

interaction can occur. In the latter case the main simulation software are:

- **GEANT3** is one of the first Monte Carlo simulation package and is written in FORTRAN.
- **FLUKA** is developed using the FORTRAN language and has several common features with GEANT3.
- **Geant4** is the latest generation of simulation software entirely written in C++ and with a modern object-oriented design.

3.1.1 GEANT3

GEANT3 is a system of detector description and simulation tools that help physicists in: detectors design and optimisation, events reconstruction and analysis, experimental data interpretation.

The first version of GEANT dates back to 1974. It was a bare framework which initially emphasised tracking of a few particles per event through relatively simple detectors and it had been developed with continuity over the years until 1994, when the last version 3.21 was released. GEANT version 3 (GEANT3) originated from an idea of René Brun and Andy McPherson in 1982 during the development of the OPAL simulation program and was based on the skeleton of GEANT version 2 code. In GEANT3 were developed the first versions of the graphics system as well as the early versions of the interactive package, a first version of the electromagnetic processes and an interface with GHEISHA as hadronic shower package were inserted. Since about 2000, the last version release has been essentially in stasis and receives only occasional bug fixes.

The GEANT3 program simulates the passage of elementary particles through the matter. Originally designed for the high-energy Physics experiments, it has found applications also outside this domain. The principal applications of GEANT3 in high-energy Physics are the transport of particles through an experimental setup for the simulation of detector response and the graphical representation of the setup and particles trajectories. The GEANT3 [34] system allows to:

- describe an experimental setup by a structure of geometrical volumes.

- accept events simulated by Monte Carlo generators.
- transport particles through the various regions of the setup, taking into account geometrical volume boundaries and physical effects (particles, materials, magnetic fields).
- record particle trajectories and the response of the sensitive detectors.
- visualize the detectors and the particle trajectories.

The program contains *dummy* and *default* user subroutines called whenever application-dependent actions are expected and it is the responsibility of the user to:

- code the relevant user subroutines providing the data describing the experimental environment.
- assemble the appropriate program segments and utilities.
- compose the appropriate data records which control the execution of the program.

A main program has to be provided by the user and it has to contain the three phases of the run:

1. initialisation: controlled by the user in the subroutine `UGINIT` and that initialises the `GEANT3` common blocks, the memory manager, drawing package, reads *free format* data records to modify the default options, processes all the geometrical information, book the histograms if required and computes energy loss and cross-section tables. In this subroutine the user has to define the geometry setup, the medium parameters and define the sensitive regions.
2. event processing: triggered by a call to the subroutine `GRUN` which, for each event to be processed, initialises and processes one event. After each step along the track, control is given to the subroutine `GUSTEP` and the user is able to take appropriate action such as storing information or killing particles, etc.
3. termination: controlled by the user via the subroutine `UGLAST` where statistical information is calculated and printed.

3.1.2 FLUKA

FLUKA[35] is a general purpose tool for calculations of particle transport and interactions with matter, covering an extended range of applications from proton and electron accelerator shielding to target design, calorimetry, dosimetry, activation, detector design, cosmic rays, neutrino physics, radiotherapy etc.

The history of FLUKA goes back to 1962-1967. During this period, Johannes Ranft was at CERN doing work on hadron cascades under H. Geibel and L. Hoffman, and wrote the first high-energy Monte Carlo transport code. Starting from those early pioneer attempts, it is possible to distinguish three different generations of this code along the years: FLUKA of the '70s, FLUKA of the '80s and the FLUKA of today. These codes stem from the same root and every new generation originated from the previous one. The name FLUKA has been preserved but the present code is completely different from the versions released before 1990. The first codes of Ranft were originally non-analogue and were used as a tool for designing shielding of high energy proton accelerators. The first analogue cascade code was written from 1967 and 1969, it was called FLUKA (**FLU**ktuierende **KA**skade) and was used to evaluate the performances of NaI crystals used as hadron calorimeters [36]. The particles considered were protons, neutrons and charged pions. Some development were done and the generator could sample also neutral pions, kaons and antiprotons. Ionisation energy losses and multiple Coulomb scattering were implemented as well, although it was in a crude way and the transport of low-energy particles were not simulated. After the SPS construction phase, a complete re-design of the code was started in 1978 and the goal was to make a more user friendly hadron cascade code with flexible geometry and with a modern formulation of the hadron interaction model. The existing versions of Ranft's programs were unified into a single code under the name of FLUKA. The new code was capable to perform multi-material calculations in different geometries and to score energy deposition, star density and differential fluxes. The possibility to work with complex composite materials and the use, in principle, of Combinatorial Geometry were introduced. Moreover were added a first attempt at simulating ionisation fluctuations, a rudimentary transport of particles in magnetic fields and the first model to describe the nucleus-nucleus collisions. At about the time when the last version

was frozen (1987), a new generation of proton colliders started to be planned, but the design of the new accelerators and associated experiments needed a capability to handle large multiplicities, strong magnetic fields, energy deposition in very small volumes, high-energy effects, low-energy neutron interactions. A. Ferrari and A. Fassó set up a plan to transform FLUKA into a code which could handle most particles of practical interest and their interactions over the widest possible energy range. Over a period of six years, FLUKA evolved from a code specialised in high-energy accelerator shielding, into a multipurpose code applied in a very wide range of fields and energies: neutrino physics and cosmic ray studies, accelerators and shielding, synchrotron radiation shielding, background and radiation damage in experiments, dosimetry, radio-biology, calorimetry and spallation sources.

FLUKA reads user input from an ASCII standard input file and it consists of a text file containing a sequence of option lines, called *cards*, which are followed sometimes by data cards specific of the option or command requested. Option cards have all the same structure and can be read in fixed or free format. The general structure of the FLUKA command line (card), contains:

- one keyword,
- six floating point values called WHATs,
- one character string called SDUM.

Some WHATs represent numerical quantities (energy, coordinates, etc.), while others are converted to integers and they are indices corresponding to a material, a type of particle, etc. Not necessarily all WHATs and SDUMs are used. Apart from FLUKA commands, the input file may contain also the description of the geometry of the simulated detector provided by means of specific geometry command cards in a special format or, on request, it can be kept in a separate ASCII file. The typical structure of a FLUKA input file is the following:

- Titles and comments for documentation purposes (optional)
- Description of the geometry (mandatory)
- Definition of the materials (mandatory unless pre-defined materials are used)

- Material assignments (mandatory)
- Definition of particle source (mandatory)
- Definition of the requested detectors where the user wants to calculate the expectation value of a physical quantity
- Definition of biasing schemes (optional)
- Definition of settings such as energy cut-offs, step size, physical effects not simulated by default, etc. (optional)
- Initialisation of the random number sequence (mandatory if an estimation of the statistical error is desired)
- Starting signal and number of requested histories (mandatory)

In addition, special commands are available in FLUKA for more advanced problems involving magnetic fields, time-dependent calculations, transport of optical photons, event by event scoring etc. There are more than 70 option keywords available for input in FLUKA and a summary is given in Section 7.1 in reference [35].

3.1.3 Geant4

Geant4 is a toolkit for simulating the passage of particles through matter. It includes a complete range of functionality including tracking, geometry, physics models and hits. The toolkit is the result of a worldwide collaboration of physicists and software engineers. It has been created exploiting object-oriented technology and implemented in the C++ programming language.

The origin of Geant4 development can be traced back to two studies done independently at CERN and KEK in 1993 [37]. Both groups investigated how modern computing techniques could be applied to improve the existing FORTRAN based GEANT3 [34] simulation program. These two activities were merged at the end of the same year and a formal proposal, RD44, was submitted to construct an entirely new program based on object-oriented technology. The R&D phase was completed in the end of 1998 [38] with the delivery of the first production release.

Subsequently the Geant4 collaboration was established in 1999 to continue the development and refinement of the toolkit, and to provide maintenance and user support. The essential kernel capabilities were provided in this first public version of Geant4. Subsequent releases focused on providing a number of refinements, improvements, performance enhancement and additional developments required by the more sophisticated simulation applications pursued by the experiments. Most of these requirements have been concentrated in three areas of the kernel development: run and event management, region dependent production threshold and variance reduction [39]. Improvements in the Geant4 kernel are not limited to the implementation of new functionality, but also include consolidation and continuous monitoring of its performance and validation.

Geant4 is driven by the software needs of modern experiments and it contains components (event generator, detector simulation, reconstruction and analysis) that can be used separately or in combinations. Other design requirements are that it is modular and flexible, and that its implementation of physics is transparent and open to user validation. Its modular architecture let the user to pick only those components he needs. All the aspects of the simulation process have been included in the toolkit:

- the geometry of the system
- the materials involved
- the fundamental particles of interest
- the generation of primary events
- the tracking of particles through materials and electromagnetic fields
- the physics processes leading particles interactions
- the response of sensitive detector components
- the generation of event data
- the storage of events and tracks
- the visualization of the detector and particle trajectories

- the capture and analysis of simulation data at different levels of detail and refinement

The toolkit modular and hierarchical structure is reflected in its class category diagram, showed in figure 3.1. The categories at the bottom of the diagram are used by virtually all higher categories and provide the foundation of the toolkit. The **global** category covers the system of units, constants, numeric and random number handling, while the categories **materials** and **particles** implement facilities necessary to describe the physical properties of particles and materials for the simulation of particle-matter interactions. The **geometry** module offers the ability to describe a geometrical structure and propagate particles efficiently through it. Above these reside categories required to describe the tracking of particles and the physical processes they undergo. The **track** category contains class for tracks and steps, used by the **processes** category, which contains implementations of physics models. All processes are invoked by the **tracking** category, which manages their contribution to the evolution of a track's state and provides information in sensitive volumes for hits and digitization. Above these the **event** module manages events in terms of their tracks and the **run** category manages collections of events that share a common beam and detector implementation. A **readout** category allows the handling of pile-up. Finally capabilities that use all of these categories and connect to facilities outside the toolkit through abstract interfaces, are provided by **visualization**, **persistency** and **interfaces** categories.

3.1.4 Reasons of the Geant4 choice

The choice of Geant4 over other packages as the basis for LVDG4 was motivated by its flexibility and active development within the particle physics communities, as well as its C++ and object-oriented structure. Geant4 is open-source and allows collaborations with members from multiple countries to use it. It is widely spread among physicists and so it is constantly tested and updated. Finally it will likely be supported for at least another decade.

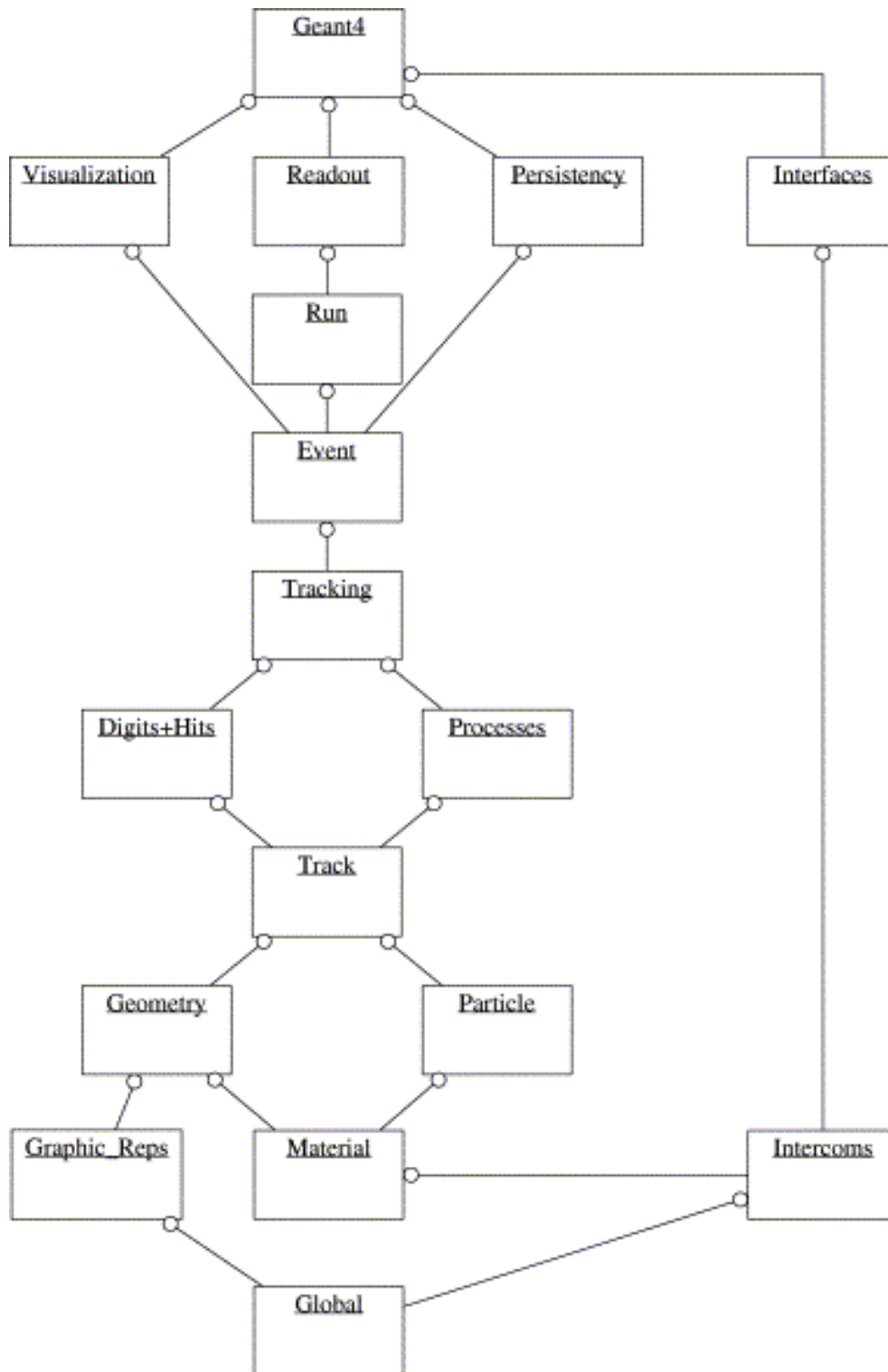


Figure 3.1: *Geant4* class categories. The open circle on the joining lines represents a using relationship; the category at the circle end uses the adjoined category [40].

3.2 Structure of the simulation

In section 3.1.3 has been showed the main characteristics of the Geant4 simulation toolkit. It provides the abstract interface for eight user classes and the concrete implementation, instantiation and registration are mandatory in three cases, but optional in the other five. The three mandatory classes describe the geometry, the physics list and event generator. The optional user classes allow the application programmer to modify the default behaviour of Geant4 and are used to gather and collect information for some specific particle or hit information when certain conditions happen. In the next sections will be described the classes implemented in the code.

3.2.1 Geometries

The geometry module offers the ability to describe a geometrical structure and propagate particles through it. The concepts of *logical* and *physical* volume are like those of GEANT3. A logical volume represents a detector element of a certain shape that can hold other volumes inside it and has access to other information such as material and sensitive detector behaviour. A physical volume represents the spatial positioning of the logical volume. In Geant4 the logical volume has been refined by defining the shape as a separate entity named *solid*. LVDG4 supports geometric description via the Geant4 geometry description classes (mentioned above) and currently it has 5 user-selectable geometries, each one encoded in a class that derives from a geometry base class (*LVDG4DetectorConstruction*). The main methods of this class are:

- *ConstructDetector()* method that is invoked by Geant4 to construct the detector geometry during run-time and it returns the pointer to the world physical volume that is defined as the biggest volume which host the whole detector.
- *DefineMaterials()* that is executed at the beginning of detector construction and its dedicated to the definitions of all the materials used in the simulation. The materials can be selected among Geant4 predefined materials or built by the developer.

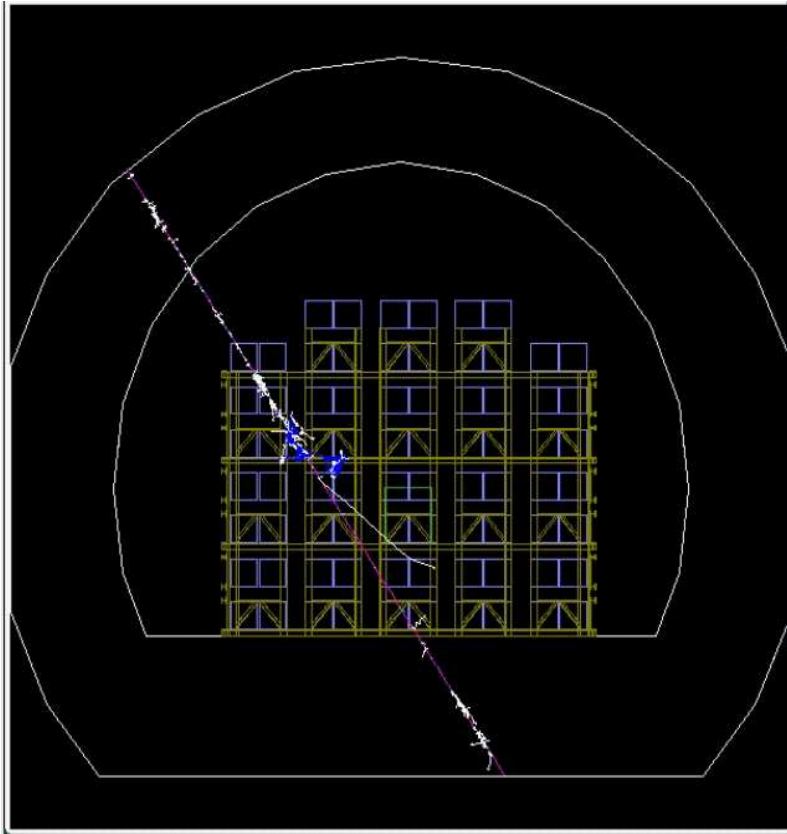


Figure 3.2: *View of a simulated muon event.*

The selectable geometries range from a simple block of homogeneous material to the single counter and finally to a full detector description. These geometries can be selected run-time by the user via a Geant4 Messenger in a macro file and an example of the geometry used in the simulation is shown in figure 3.2.

3.2.2 EventGenerators

These classes generate the initial conditions of each event to be simulated. LVDG4 has an event generator (*LVDG4ParticleSource*) that is instantiated in the base class (*LVDG4PrimaryGeneratorAction*) constructor. The user can instantiate the selected generator at run-time via a Geant4 messenger. The base class contains the method:

- *GeneratePrimaries*(*G4Event * pEvent*) method that sets the seeds for the random generator and passes the initial event particle type (or array of particles), position, momentum and time to the *G4Event* object.

The event generator class contains the following relevant methods:

- *GeneratePrimaryVertex*(*G4Event * pEvent*) method that takes the information given by Geant4 messenger and creates the primary vertex or vertexes to be passed to the base class.
- *ReadMuFile*() method that reads the muon momentum direction and energy from a file.
- *FindInitialPosition*() method used to find out the vertex position.
- *GenerateCfSource*() method that generates neutrons in a given position, with an isotropic flux and energy sampled from the Cf emission energy spectrum.
- *Multigenerator*() method that reads an input file and can generate multiple vertex with different types of particles each one with its energy, position, momentum direction and time.

The muon flux is a specific parameter that characterizes each underground laboratory and it is known experimentally. The muon energy spectrum and angular distribution are interrelated and this correlation depends on the particular surface profile of the mountains above the laboratory. This information can be obtained by Monte Carlo simulations and confirmed for a given range by experiment. In this case it has been used MUSIC [12], a fast code able to propagate muons through large distances in different materials, and to predict reliably the energy and angular distribution, provided the mountain profile (figure 3.3 *left* is showed the muons slant depth as a function of their direction for the Gran Sasso mountain). It has been used also another code MUSUN [13] to generate muons accordingly to their angular and energy distribution at the underground site. LVDG4 uses the outcome of these two dedicated code and propagates them in the rock and detector. Muons are randomly sampled over a circle centered in the LVD detector and with radius

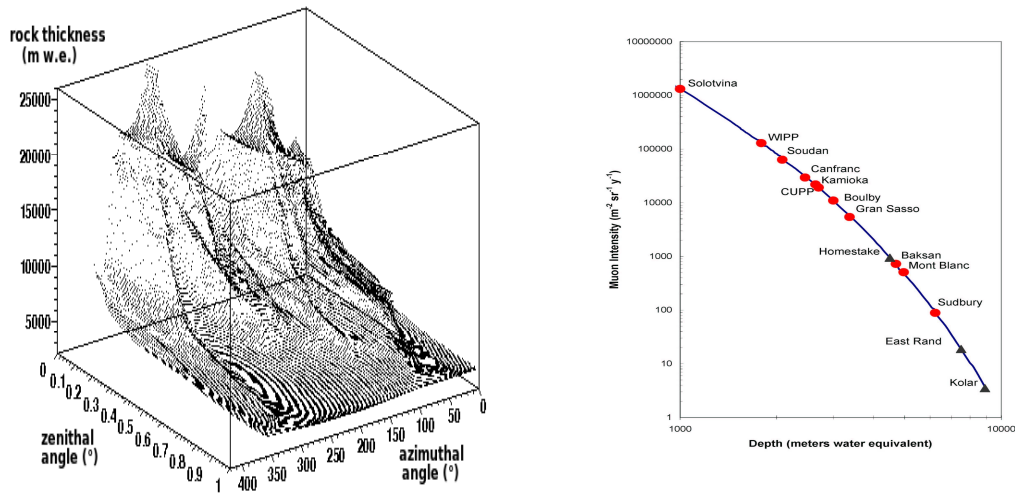


Figure 3.3: *Left: Map of the rock thickness crossed by muons as function of the zenithal and azimuthal angle for the Gran Sasso laboratory. Right: Muon intensity as a function of depth in the main underground laboratories.*

a slightly larger than the maximum detector dimension (15.3 m). In this way, knowing the residual muon flux in the laboratory (as showed in figure 3.3 *right*), it is easier to evaluate the live time corresponding to a certain number of muons simulated. Once the point has been sampled, the circle (and so the point over it) is rotated to make it perpendicular to the muon direction and the vertex position is given by the intersection between the external rock surface and the line that crosses the point and with the same direction cosines of the muon.

3.2.3 Physics Lists

Geant4 physics is encoded into classes called *physics lists*, which are meant to be a complete specification of the physics employed to simulate a particle's path through an experimental setup. No one model is sufficient to deal with all the physics over a wide energy range and variety of particle species and in most cases alternative models cover similar energy ranges and particle types. In constructing a physics list, it is often required that two very different models be joined together to cover a given energy range. In Geant4 this is done by causing the two models

to overlap in an energy range where they are both valid and merging them in that range. The blending is done by randomly choosing one model or the other with a probability that changes linearly with energy over the common interval. The smoothness of this probability depends on the width of the overlap interval and nature of the two models. A process can not have an energy range with no valid model registered and a model can not be entirely contained in the energy range of another model. The Geant4 toolkit provides the possibility to define a process, attach it to different kind of particles and then describe the process with several physics models each of them valuable in a specific energy range that can be set by the developer, otherwise it can choose one of the Geant4 pre-defined physics lists like a *black box*.

The LVDG4 physics is based on several advanced examples distributed with Geant4 [41] and it is instantiated in the base class (*LVDG4PhysicsLists*) and the main methods are:

- *ConstructParticle()* method that builds all the particles could be produced in the interactions like bosons, mesons, baryons, leptons, etc.
- *ConstructProcess()* method that builds the process for each kind of particle.
- *SetCuts()* method that set the production cuts for particles. These cuts are given as a function of the range and then they are internally converted in energy cuts by Geant4 for each type of material used in the simulation. They are optimized for each region defined in the detector.

In LVDG4 we choose to build the physics list as follows. Standard models have been used for the electromagnetic interactions of muons, electrons and positrons. The e^\pm interactions with nuclei are simulated on the basis of the equivalent photon approximation and the final states are generated by a Chiral Invariant Phase Space (CHIPS) decay model [42]. The same model is used to describe the photo-nuclear reactions below 3 GeV, while for higher energies the final states are generated according to a theory-based parton-string model, called Quark-Gluon String Pre-compound model (QGSP). Hadronic interaction of muons with nuclei are managed by the `G4MuNuclearInteraction` model, where muons produce virtual photons which are in turn converted to pions which interact with the nucleus using a

model derived from the GHEISHA code [43]. The physics list includes the capture and decay processes for the μ^\pm as well.

The hadronic interactions handle the elastic scattering, inelastic scattering (for all hadrons), capture (for neutrons, π^- and K^-), fission (only for neutrons) and decay. All these processes are included in the LVDG4 code and associated to the respective particle. The elastic scattering of all long-lived hadrons is described by the `G4HadronElastic` model, instead of the `G4LElastic` model used in past versions of Geant4. Elastic scattering of neutrons from thermal energies up to 20 MeV is simulated according to the high-precision, data-driven `G4NeutronHPElastic` model, which is based on the tabulated cross section and final state data from the ENDF/B-VI database [44]. The same database is used as well by other processes defined for neutrons below 20 MeV that simulate capture, inelastic scattering and fission processes, while for energies above 20 MeV the capture and fission processes are described by models called `G4LCapture` and `G4LFission`. A particular attention has been paid to describe the neutrons inelastic scattering. For neutrons between 20 MeV and 10 GeV it uses the Geant4 Binary Cascade that is a time-dependent model of the intra-nuclear cascade. The Low Energy Parametrized (LEP) model bridges the low-energy Binary Cascade region and the high-energy QGSP regime. Its energy range of validity is between 9.5 GeV and 25 GeV. The QGS model handles the inelastic interactions from 12 GeV to the highest energy neutrons by simulating hadron-nucleon collision as exchanged quarks, which form strings, which in turn stretch and hadronize to produce multiparticle hadron final states. Geant4 provides pre-equilibrium and de-excitation models that are used as back-end stages for the nuclear reaction. The pre-equilibrium model is based on the semi-classical exciton model [45], where the precompound stage of nuclear reaction is considered until nuclear system reaches equilibrium. During this stage, transitions to states with different number of excitons compete with particle emissions, including emission of light compound fragments (up to α). Further emission of nuclear fragments or photons from excited nucleus is simulated using the Geant4 native de-excitation model that includes several semi-classical alternative/competitor models: evaporation of nucleons and light fragments, photons evaporation, fission, statistical multifragmentation and Fermi break-up [46]. The QGSP model has been adopted for inelastic scattering of proton with en-

	rock	concrete	iron	scintillator
cut in range	1	0.5	0.1	0.1
γ cut in energy	6.5	4.8	6.3	0.1
e^- cut in energy	631	363	236	76
e^+ cut in energy	603	349	228	75

Table 3.1: *Production cuts. Cuts in range are given in mm, while cuts in energy are given in keV.*

ergy higher than 12 GeV, the binary cascade for low-energy ones (less than 9.9 GeV and between the two region the interaction is described by the Low Energy Parametrized (LEP) model. The latter model has been used as well for charged pions and kaons with energy below 25 GeV while QGSP is adopted above 12 GeV. To simulate the inelastic interactions of long-lived hadrons the models used are the parametrized ones LEP for hadrons below 25 GeV and HEP above 20 GeV. These models originates from the old GHEISHA hadronic package of Geant3, they provide a faster alternative to the theory-driven models and they are used for some long-lived baryons, due to the lack of alternatives.

Geant4 tracks all simulated particles down to zero range, although various options exist to manually limit step size, track length, time-of-flight, and other parameters. Production cuts for δ -rays and for soft bremsstrahlung photons are expressed in spatial ranges and internally converted into energy thresholds for the production of these particles in the corresponding material. It is necessary to find a trade-off between accuracy and computing time. For this reason the cut-per-region approach is used in the LVDG4 setup and the production cuts in range (and in energy) for each material are showed in the table 3.1. The cuts are really small in order to have an accurate description in the sensitive regions while in other materials are more relaxed.

3.2.4 Output Format

During the simulation Geant4 generates complete information about the trajectory and interaction of particles as they propagate through the detector. LVDG4 defines a generic base output class and does not use a built-in output format, but we have implemented an interface to the ROOT [47] analysis tool. LVDG4

has implemented few classes that save several important Geant4 information that are gathered in two different ROOT *trees*. The first *tree* collects all information concerning the neutron generation and their interactions, the characteristics of the primary particles and all the information for each kind of particle inside the sensitive component of the detector defined in subsection 3.2.1. The second *tree* saves information about the energy deposition and time in each counter as well. The output format consist of a class that inherits from a virtual base class (*LVDG4AnalysisManager*) that contains the following main methods:

- *BeginOfRunAction()* and *EndOfRunAction()* methods that are executed at the beginning and the end of a simulation run respectively. They are used to open and close data files, ROOT trees and allocate and deallocate data structures.
- *BeginOfEventAction()* and *EndOfEventAction()* methods that are executed at the beginning and end of the events. They are used to process on event data, fill the ROOT trees and clear vectors and structures that store stepping information.
- A *SteppingAction()* method that is executed at the end of each step. It gathers all the information concerning the particle in the boundary between the concrete and the experimental hall. It updates also the track length in each materials crossed by the primary particles.

3.2.5 Materials

The basic unit of the mandatory class that defines the geometry is the *logical volume* that consists of a shape, material, visualization attributes and can be marked as *sensitive* so the user code can be invoked when a particle passes through. Geant4 gives the possibility to use some pre-defined material with the right isotopic and element composition and density, or to define user own materials building materials by their elements. The elements as well, can be pre-defined or user built specifying the isotopes concentration. The main materials used in the LVDG4 are several, but some of them like iron, argon, mylar, plexiglass and air are ordinary and so we used the pre-defined materials provided by Geant4, while other

ones have some peculiar compositions that do not correspond to the pre-defined ones like the liquid scintillator, rock concrete and stainless steel.

Gran Sasso rock consists mainly of $CaCO_3$ and $MgCO_3$ with a density of $2.71 \pm 0.05 g/cm^3$ [48]. Due to the presence of a certain type of rock, called *roccia marnosa nera*, the pre-defined rock composition differ from the Gran Sasso rock. Since there are no data on the chemical composition of Gran Sasso concrete available in literature, several samples were taken from different places in the laboratory and then analyzed. In order to reduce radioactivity in the underground laboratories a special cement was used with an higher concentration of cement instead of sand and so the concrete composition is different respect to the one provided by Geant4. As seen in section 2.1 the basis of the liquid scintillator is based on hydrocarbon with composition C_nH_{2n} , where $\bar{n} = 9.6$, and is defined with the fraction mass of H and C, 14.37% and 85.63% respectively. The fraction mass The stainless steel has been defined as: 71% of Fe, 19% of Cr and 10% of Ni. All the materials are built giving the fraction mass of each element and they are showed in table 3.2. In the table it is also reported the rock composition of the underground laboratories of Modane (LSM) in France, which we used to compare the muon-induced neutrons fluxes in both laboratories and presented in the section 4.4 and the rock composition around the underground laboratories in Sudbury that will be used in the evaluation of the LVD performances as shield and active vetoing in section 5.1.

3.3 Physics lists validation

The Geant4 simulation toolkit is used in various applications of modern physics and its wide use in so many different fields provides the possibility to test all the physics models (electromagnetic, hadronic and optical processes) implemented in Geant4 and employed by the LVDG4 code.

For the electromagnetic interactions of photons and electrons, four models are available: *Standard*, *Low-energy*, *Penelope* and *Livermore*. The *standard* models adopted in the LVDG4 code are tuned to high-energy physics applications; they are less precise in the low-energy region and do not include atomic effects, however they are faster in terms of computing time. The other models describe photon and electron interactions with energies down to 250 eV and take into account

	concrete	LNGS	LSM	Sudbury
H	1	0.03	1	
C	0.1	12.17	5.94	
O	52.9	50.77	49.4	43.47
Na	1.6		0.44	2.3
Mg	0.2	8.32	0.84	5.6
Al	3.4	0.63	2.58	9
Si	33.7	1.05	6.93	25.9
P			0.06	
K	4.4	0.1	0.21	0.7
Ca	1.3	26.89	30.6	5.8
Ti			0.07	
Mn			0.03	0.13
Fe	1.4		1.9	7.1

Table 3.2: *Fraction mass of the elements that compound the LNGS, LSM and sudbury rock, and the concrete.*

fluorescence, Auger emissions, Doppler broadening, atomic relaxation subsequent to photoelectric, Compton and ionization interactions. All these models provided by Geant4 for γ rays and e^\pm have been systematically validated by the Geant4 Collaboration [49] and by other groups [50] at few-percent level.

During the last five years, development of Geant4 hadronic physics models has been driven largely by the LHC detectors and the subsequent comparison of new data with the simulated detector responses. As the data has begun to come in, the validation of these models has represented one of the major efforts of the Geant4 collaboration. These models include quark-gluon strings, intra-nuclear cascades, nuclear de-excitation and elastic and quasi-elastic scattering [51]. LHC experiments (in particular ATLAS and CMS) have studied the physics performances of the different physics lists and have converged towards the use of the so-called QGSP_BERT physics lists as the default one. According to reference [52], the Bertini cascade combined with the QGS model gives the best results in terms of describing the data collected with the calorimeters during the test-beam campaigns. The predictions of the Binary cascade for the differential cross sections of secondary neutron production for proton beam with energy below 1 GeV [53] is better than the Bertini-style cascade. However, the Binary cascade cannot replace

the Bertini cascade because for high incident proton energies the BIC currently overestimate forward neutron cross section and underestimate backward neutron cross section. Moreover the Binary cascade simulation is slower, especially for heavy targets [54].

The review of the native pre-equilibrium and de-excitation models of Geant4, used for sampling of residual nucleus fragmentation in hadron/ion inelastic scattering, has recently performed and presented in reference [46].

Chapter 4

Neutron measurements and simulations

Several measurements and simulations were performed concerning the neutron production and propagation but there are disagreement between experimental data and simulations. A summary of the existing measurements and simulations will be presented in section 4.1 and, where possible, a comparison among the results are shown. Before applying the MC simulation developed to analyze experimental data, several tests have been performed. In section 4.2 a set of simulations have tested 4 physics lists, provided by Geant4, in order to evaluate which one was the best. A test on the neutron capture time has been performed for neutrons emitted by a ^{252}Cf source and presented in section 4.3. Finally in section 4.4 the simulation has been applied to estimate the flux of neutrons coming from the rock and a comparison with FLUKA will be shown.

4.1 Existing measurements and simulations

Simulations of fast neutrons are difficult due both to the uncertainties in theoretical models and to disagreement between simulations and experimental data. The fact that primary neutrons and other secondary particles, originated from cosmic muon, may themselves produce secondary neutrons and hadronic interactions, further complicates calculations and makes benchmarking these processes difficult.

The main characteristics studied are focused on the neutron propagation and production and on the neutron flux. In this section are presented the experimental results and, where data are available, a comparison with simulations. Furthermore differences and analogies between FLUKA and Geant4 in this field are presented too.

4.1.1 Neutron propagation

The neutron propagation is of fundamental importance to study the shielding techniques which must be adopted in order to reduce the neutron flux from rock. For this reason the Monte Carlo codes must be accurate enough for such a job.

An experiment was performed at the Stanford Linear Accelerator Center (SLAC) which involved a 28.7 GeV electron beam incident upon a cylindrical aluminum beam dump inside a shield housing that consists of two lateral steel shields and one top steel shield in addition to concrete positioned around all sides. An organic liquid scintillator detector was placed outside the shields and the measurement were performed for three different widths of the concrete shield (2.74, 3.35 and 3.96 m). A detailed description of the SLAC beam dump experiment can be found in reference [55]. Primary neutrons were generated mainly by photonuclear interactions initiated by bremsstrahlung photons from the decelerating electrons. The neutron time-of-flight (TOF) and energy spectra were measured outside a steel-and-concrete shield. The final neutron spectrum outside the shield consisted of both primary neutrons as well as secondary neutrons created through inelastic interactions of the primary neutrons with shield material. The experiment has been simulated in detail using the FLUKA simulation package [56] generating results in agreement with experimental data.

Last year the MAJORANA and GERDA collaborations developed MAGE [57] (MAJorana-GERda), a Geant4-based physics simulation software framework. In the early phases of the program developing, the MAGE collaboration performed two simulations [58] for testing the physics lists used in their code. The first test was conceived to study the propagation of neutrons and compare the results with experimental data and FLUKA simulation of the experiment performed at SLAC. For this test they have used the version 8.1 of Geant4 and the physics list called

QGSP_BIC_HP. The simulations were performed for all three shield widths and they have calculated the total fluence in addition to neutron energy spectra and TOF distributions at each shield width. Comparisons between the Geant4 calculated spectra, the FLUKA calculated spectra and experimental data are showed in figure 4.1. Geant4 demonstrates reasonably good agreement with the shape of the spectra, but the agreement with the fluence slightly worsens as the shield width is increased. Geant4 and FLUKA both calculate harder spectra than the experimental data. The TOF distributions reproduce the shape of the data but show the same difference for the fluence. The total fluence of neutrons having kinetic energy 6 MeV and greater was calculated and exponential fits were performed for all three data sets. These fits show that the attenuation length of neutrons simulated by Geant4 is shorter than the one measured in the experiment. The fits also indicate that the total neutron flux entering the concrete shield is underestimated by Geant4 by about a factor of 4÷5. Using the integrated neutron fluxes, the authors of the paper suggest that for a material of 10 ft width, Geant4 overattenuates neutrons by roughly a factor of 4. No data are available to which one may compare a simulated neutron transport through high-Z materials. Therefore, it must be extrapolated from results at low-Z. These results are in disagreement with the ones got in reference [59], where for the first time it has been compared the propagation of low-energies neutrons through large thickness of rock and two common shielding materials (lead and hydrocarbon material) using the MCNPX version 2.5 [60],[61] and Geant4 version 7.0 patch 01. MCNPX is a toolkit extensively used to model shielding around nuclear detectors with a precise description of low-energy neutrons. In this work neutrons from radioactivity have been generated in a volume of rock of $1 \times 1 \text{ m}^2$ section and 3 m depth and volume for neutron propagation has been taken much larger with a cross section of $10 \times 10 \text{ m}^2$. Two configurations of shielding have been studied. In the first one, neutrons have been propagated through different thickness ($5 \div 50 \text{ g/cm}^2$) of hydrocarbon shielding CH_2 . In the second one, neutrons have first been propagated through a slab of lead 30 cm thick before further propagation through CH_2 . At the rock surface (it has been considered the rock composition at Boulby mine, with a high concentration of NaCl), Geant4, MCNPX and GEANT3 simulations differ at most by 20% in a narrow region around 1 MeV, while the integrated neutron fluxes above

1 MeV agree within 10%.

The difference is due to an error in the inelastic cross section on chlorine. The simulation has been also performed for the Modane rock and the agreement between the codes is better. The neutron spectra originated in NaCl and propagated through different thickness of CH₂ shielding gives a reasonable agreement between MCNPX and Geant4, even if taking into account the exact geometry of the cavern and the back scattering of neutrons off the cavern walls.

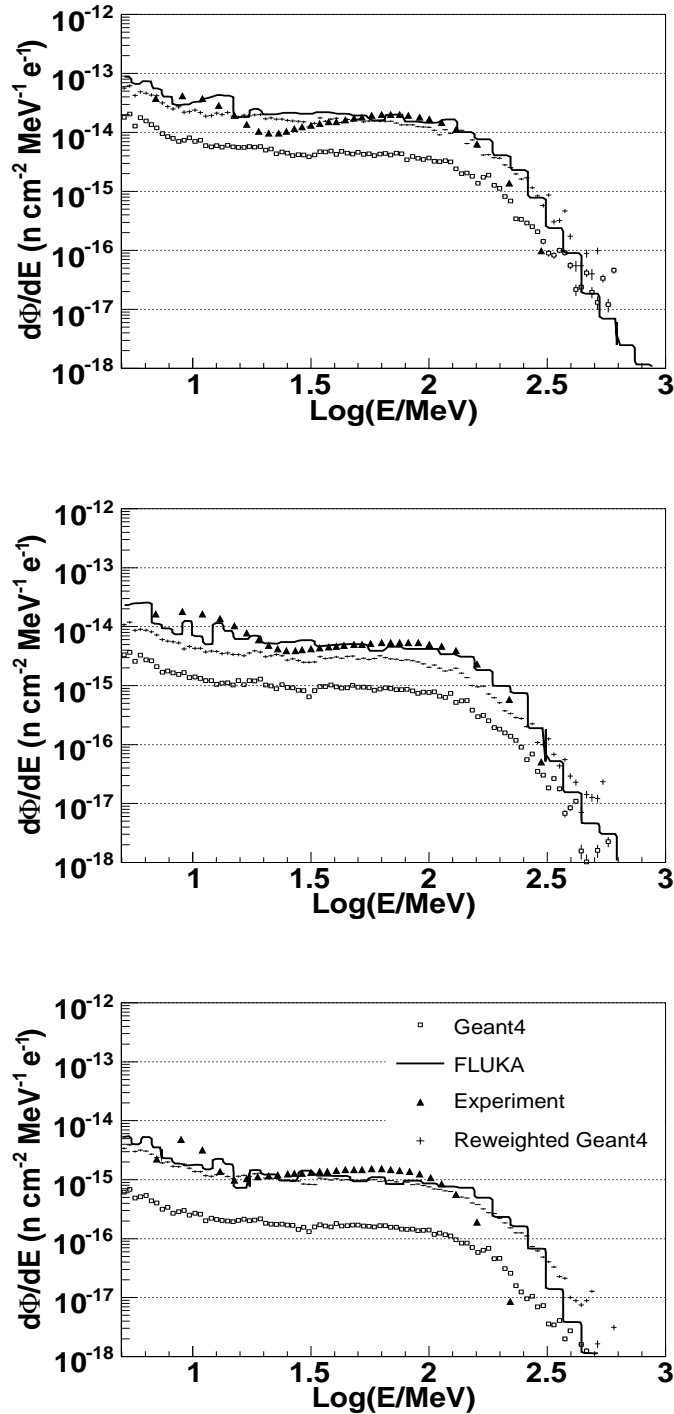


Figure 4.1: A comparison of calculated (FLUKA, Geant4 and Geant4 re-weighted) and experimental energy spectra for three shield widths (9, 11 and 13 ft). Statistical error bars are included on both of the Geant4 histograms but not on the spectra from FLUKA and experiment.

4.1.2 Neutron production

Several output parameters and distributions can be derived from the Monte Carlo simulation and one possible output is the integral neutron yield, which is normally quoted in neutrons per muon per g/cm^2 of crossed target material. The integral neutron yield has to be compared to experimental data for specific target, in order to validate and cross-check the simulations. Experimental measurements of muon-induced neutron yield are difficult because the flux is very low in deep underground laboratories. Only tonne-scale detectors are able to measure the muon-induced neutron flux with reasonable accuracy. The neutron flux can be artificially enhanced by placing a large amount of high-A material around the detector, since the neutron yield increases with the atomic weight of the target material. Unfortunately, high-A materials cannot be used for detecting neutrons. Moreover the processes of neutron production, transport and detection are quite complicated and the precise modeling of the detector geometry, hardware and software cuts and all physical processes involved, is necessary for the accurate derivation of the neutron yield.

Neutron production by muons underground have been measured at a span of depths and muon energies, from about 20 m w.e. depth and 10 GeV energy to 5200 m w.e. and 400 GeV. An estimate of the neutron production in liquid scintillator as a function of the mean muon energy has been obtained by Wang [62] and by Kudryavtsev [63] based on Monte Carlo simulations made with FLUKA. The two works are in agreement between them and both are about a factor two within the available data for depths with a mean muon energy above 100 GeV. The total neutron yields, which include neutrons of any energy, are shown in figure 4.2 as a function of muon energy (the MC statistical uncertainties are comparable to the size of the data markers). These plot has been taken from reference [64] where for the first time a comparison among FLUKA, Geant4 and experimental data has been performed. Although Geant4 results agree, at higher energies, with the power law:

$$N_Y = a \times E^\alpha \quad (4.1)$$

predicted by FLUKA ($\alpha = 0.74$ in [62] and $\alpha = 0.79$ in [63]), there is an enhancement with decreasing energy relative to the previous FLUKA simulations.

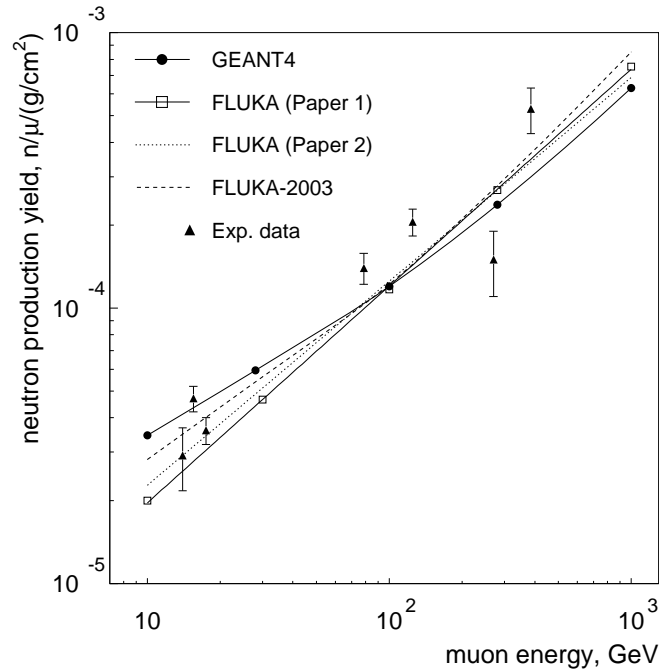


Figure 4.2: Variation of the neutron yield (per unit of muon track length) with the initial muon energy for C_nH_{2n} scintillator. Experimental data are taken from measurements at various depths between 20 and 5000 m w.e. using the mean muon energy for the respective depth [68].

In this work the authors have also analysed the importance of individual neutron-producing processes in the simulation, and it has been compared with FLUKA. There is a degree of agreement between the two codes, in that both predict neutron production in electromagnetic cascades (real photonuclear interaction) to dominate at lower energies and to decrease in importance with increasing muon energy, and generation in hadronic cascades to become more important with increasing muon energy. Both codes confirm that most neutrons are not produced in direct muon-induced spallation, but rather in the cascades muons initiate, and more so at higher energies. However, the Geant4 results reveal a greater dominance of electromagnetic cascades at low energies, and this scenario is not significantly different at high energies, where FLUKA predicts neutron production in hadronic cascades to take over. In liquid scintillator, although Geant4 appears to overproduce neutrons in electromagnetic cascades, it under-produces in hadronic cascades compared to

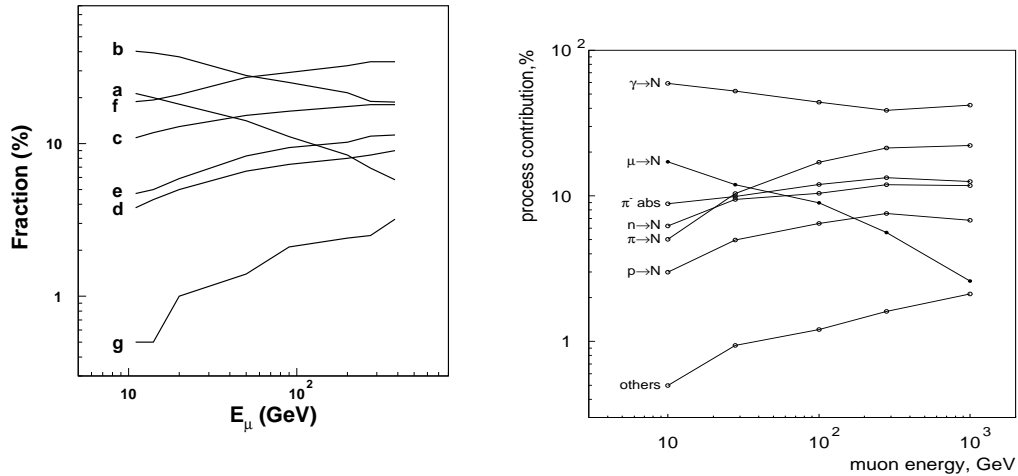


Figure 4.3: *Relative contribution of individual processes to the total neutron yield in scintillator from FLUKA (left, [62]) and Geant4 (right, [63]). FLUKA processes are: a) direct muon spallation, b) real photonuclear disintegration, c) neutron inelastic scattering, d) proton inelastic scattering, e) π^+ inelastic scattering, f) π^- inelastic scattering and capture, g) others.*

FLUKA, giving similar total yield in both codes. In figures 4.3 are shown the relative contribution of individual processes to the total neutron production in scintillator for both codes.

The overall agreement between Geant4 and FLUKA is quite good for low-A materials. FLUKA predicts the dominance of hadron-induced spallation in neutron production for practically all targets, while Geant4 favours nuclear disintegration by real photons at almost all energies and all materials.

While for low-A targets the agreement between different codes and data is reasonably good (certainly within a factor of two), some experiments with heavy targets showed much larger neutron yield than expected. The NA55 experiment at CERN measured the double differential cross-section for neutrons emitted at 45° , 90° and 135° from a 190 GeV muon beam incident upon three different materials: graphite, copper and lead. The three neutron detectors have an energy threshold (in neutron energy) of about 10 MeV. The thin-target experiment does not correspond to the real situation underground laboratories, where showers can

develop through large thickness of rock but can be modeled more accurately. A complete description of the experiment can be found in reference [65]. This experiment has been simulated by Araújo et al. (see reference [64]) using Geant4 version 6.2 and FLUKA. In this work Geant4 and FLUKA agree with each other within a factor of two, but both codes underestimate significantly the neutron production as measured by NA55, especially for copper and lead (shown in figure 4.4). The same experiment has been simulated in one of the preliminary test of the MAGE code using Geant4 version 8.0, where a comparison between the measured and simulated double differential cross-section ($d\sigma/dEd\Omega$) has been considered. The results obtained for the angular dependence agree well with the results from both Geant4 and FLUKA reported in reference [64]. Moreover the comparison between simulated and measured double differential cross-sections indicates a growing disagreement as the atomic mass of the target material increases. In particular the simulated spectrum at 135° is significantly harder than the measured spectrum as can be seen in figures 4.5 and, for lead and copper, the simulated angular distribution shows opposite curvature to the measurement.

There are other experimental data available for neutron yield in lead, obtained in deep underground laboratories, but these data are old and controversial [66], [67] and they also indicate higher neutron production in lead than expected from modern Monte Carlo simulations.

Preliminary results from the measurements of muon-induced neutrons, mainly in rock and lead, at Boulby Underground Laboratory have recently been reported [68]. The authors have built a MC simulation based on Geant4 version 8.2 to interpret the measurement obtained using a large scintillator veto deployed around the ZEPLIN-II WIMP detector. In the direct comparison between Monte Carlo and experimental data, they found that the simulation produces a 1.8 times higher neutron rate, which they interpret as over-production in lead by Geant4. This result is not consistent with the deficit of simulated neutrons discussed previously and this observed inconsistency makes the predictions of muon-induced neutron rate in various detectors uncertain by about a factor of two.

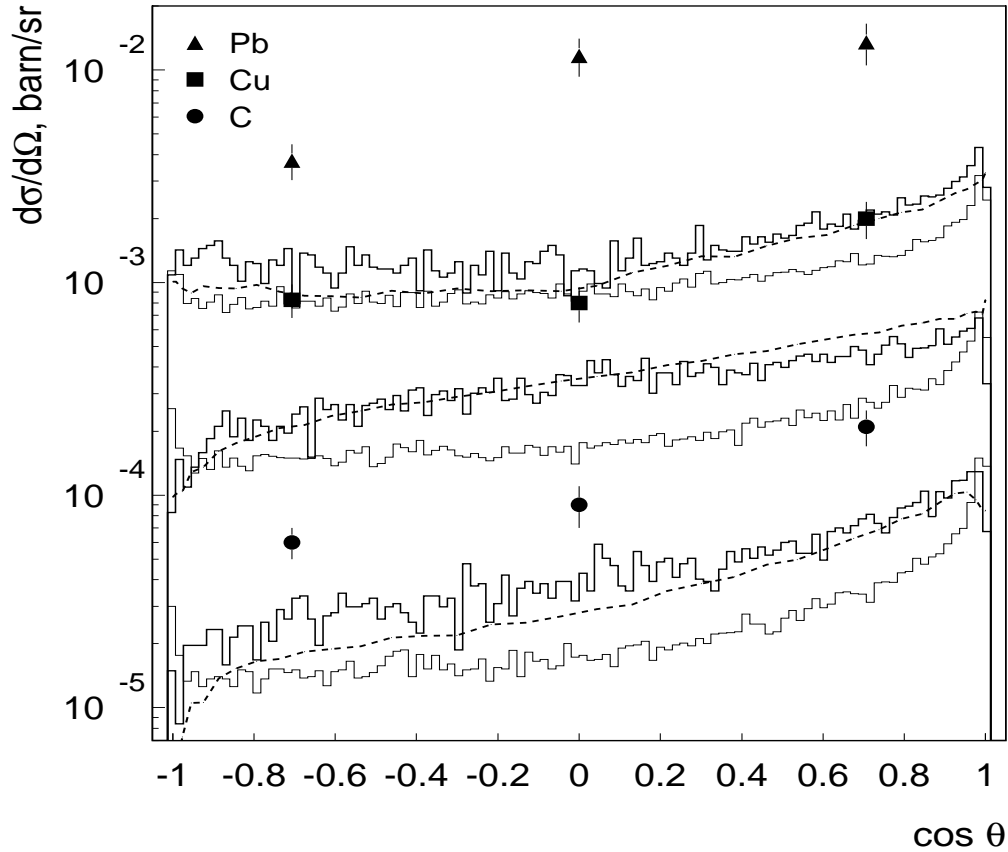


Figure 4.4: *Differential cross-section of neutron production by 190 GeV muons for a 10 MeV threshold in neutron energy. The data points represent the experimental data. The thin line histogram shows the Geant4 simulation considering muon-nucleus interactions only, while the thick histogram includes all physics processes. The dashed line represents the FLUKA results for the latter case [64].*

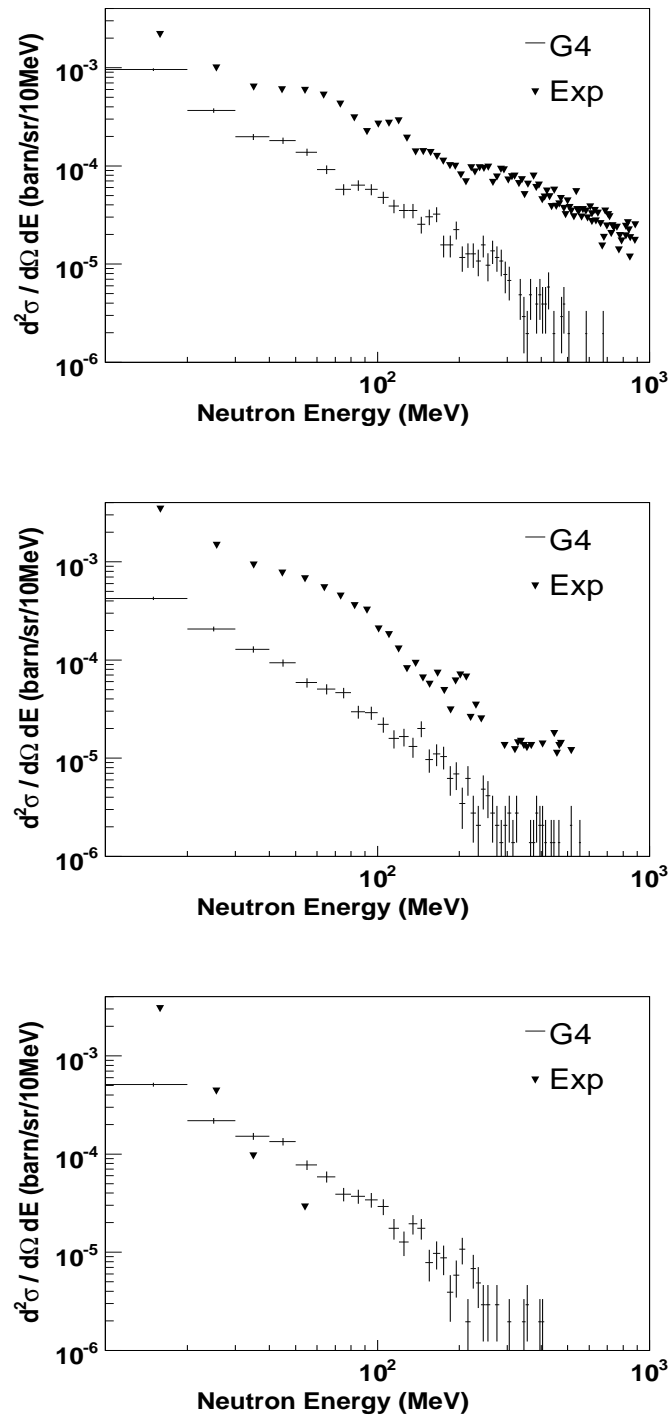


Figure 4.5: Comparison between the NA55 experiment and simulations for the lead beam dump at 45° (top), 90° (middle) and 135° (bottom). The simulated spectrum at 135° is significantly harder than the measured spectrum [58].

4.1.3 Neutron flux

The muon-induced neutron flux emerging from the rock into the cavern has been estimated for the various underground sites by Mei and Hime in reference [69]. In this work they have derived the neutron flux using a simulation based on FLUKA with an additional neutron multiplicity function to correct the neutron production rate. This function is obtained by extrapolating the variation in neutron multiplicity as a function of muon energy between the proposed parametrization based on the measurements [70], [71] and the FLUKA simulation. Using this simulation, the proposed correction function and the muon fluxes, they derive the neutron flux ϕ_n as a function of depth that can be fitted with the following:

$$\phi_n = P_0 \left(\frac{P_1}{h_0} \right) e^{-\frac{h_0}{P_1}} \quad (4.2)$$

where h_0 is the equivalent vertical depth (in km w.e.) relative to a flat overburden. The fitting function is shown in figure 4.6 and the fit parameters are $P_0 = (4.0 \pm 1.1) \times 10^{-7} \text{ cm}^{-2}\text{s}^{-1}$ and $P_1 = 0.86 \pm 0.05 \text{ km w.e.}$. In table 4.1 is summarized the neutron flux at the rock/cavern boundary for the various sites without including the back scattering of neutrons entering the cavity.

The results are in agreement with another existing simulation for Gran Sasso performed by Dementyev [72] and, within a factor of two, it is also in agreement with the neutron flux obtained by Wulandari et al. (see reference [4]) with FLUKA, which estimate the total flux of neutrons above 1 MeV entering the hall without back scattering to be $4.27 \times 10^{-10} \text{ n/cm}^2/\text{s}$ (without back scattering) and $8.53 \times 10^{-10} \text{ n/cm}^2/\text{s}$ (with back scattering).

4.2 Neutron yield

As seen in the previous sections, Geant4 provides several physics lists, each of them with a characteristic model that describe one or more processes for one or more particles and for different energy range. Moreover, the last section has also stressed the point that there are several disagreement among the experimental results and simulations for what concerning the muon-induced neutrons. For these

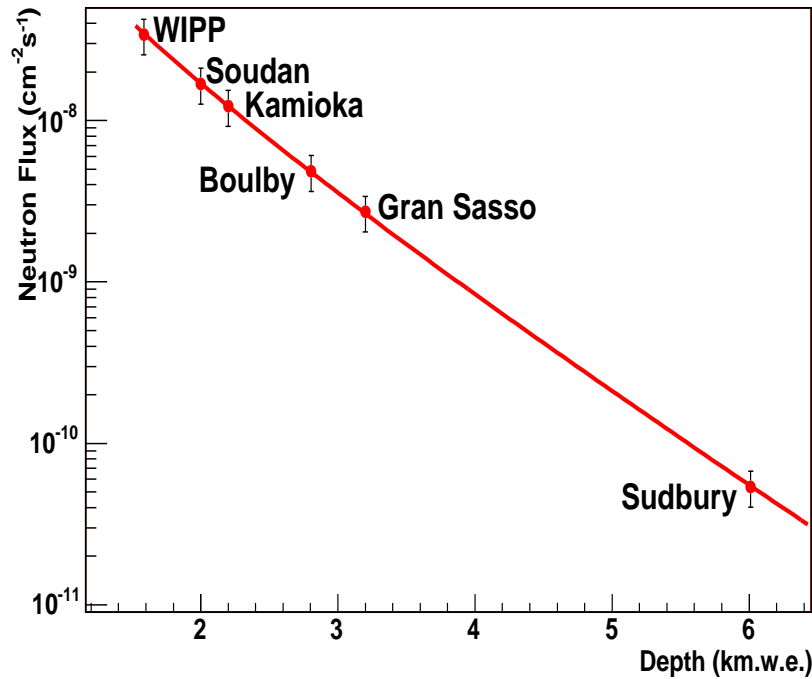


Figure 4.6: *Total muon-induced neutron flux deduced for various underground sites estimated with FLUKA in reference [69].*

reasons a large number of preliminary tests were done, before building the LVDG4 simulation code.

One of the first parameter that is necessary to estimate differences among the physics lists provided by Geant4 is the neutron yield. For such study a simple simulation has been built where muons are fired on a parallelepiped of different material. The energies of the incident muons are sampled on the muon energy spectrum at the underground laboratory as shown in figure 5.3 with a mean energy of about 270 GeV. As proved in another test [73] and observed in reference [63], a reduction (about 10 ÷ 20%) in the neutron production has been experienced when muon with fixed energy were shot instead of muon with a real spectrum underground. The muons used in the simulation are both μ^+ and μ^- and no difference has been found respect to a beam made up only by negative muons. The initial muon vertex is centered on the lateral squared face of the block material, few

Site	total	> 1.0 MeV	>10 MeV	>100 MeV
WIPP	34.1	10.78	7.51	1.557
Soudan	16.9	5.84	4.73	1.073
Kamioka	12.3	3.82	3.24	0.813
Boulby	4.86	1.34	1.11	0.277
Gran Sasso	2.72	0.81	0.73	0.201
Sudbury	0.054	0.020	0.018	0.005

Table 4.1: *The muon-induced neutron flux for six sites (in units of $10^{-9} \text{ cm}^{-2}\text{s}^{-1}$). The total flux is included along with those predicted for neutron energies above 1, 10, and 100 MeV [69].*

centimeters far parallelepiped. The materials chosen for this simulation test are: liquid scintillator, rock, iron and lead. The first three have been selected because they represent the main materials used for the full simulation of LVD, while the latter is commonly used for shielding detectors underground. As many neutrons are produced in large cascades initiated by muons, the equilibrium between neutron and muon fluxes (when the number of neutrons produced is constant with respect to the unit of muon path length) begins only when a muon has crossed a certain thickness of a medium (about 400 g/cm^2 [73]). This is because cascades need some depth to fully develop and produce neutrons, and this effect is showed in figure 4.7 where is plotted the origin vertex of muon-induced neutrons in black, and divided by their creation process, spallation in green, electromagnetic showers in red and hadron showers in blue. The spallation process has a flat shape all along the block, while neutrons induced by hadronic and electromagnetic showers needs some space before having a constant production rate. On the other hand, large thickness of material can reduce the muon energy too much compared to the initial value due to interactions with matter, but this is particularly important for low muon energies. With these considerations, the thickness of medium was chosen large enough (3200 g/cm^2) for such an equilibrium to take place, and only neutrons in the central zone of the block were counted, where the equilibrium is in place. The lateral dimensions (with respect to the beam direction) of the block are the same for all the materials and is large enough to fully contain the muon induced cascades and is about $5 \times 5 \text{ m}^2$. The longitudinal dimensions in meters are: 20, 13, 4 and 3 for liquid scintillator, rock, iron and lead, respectively. The simulation

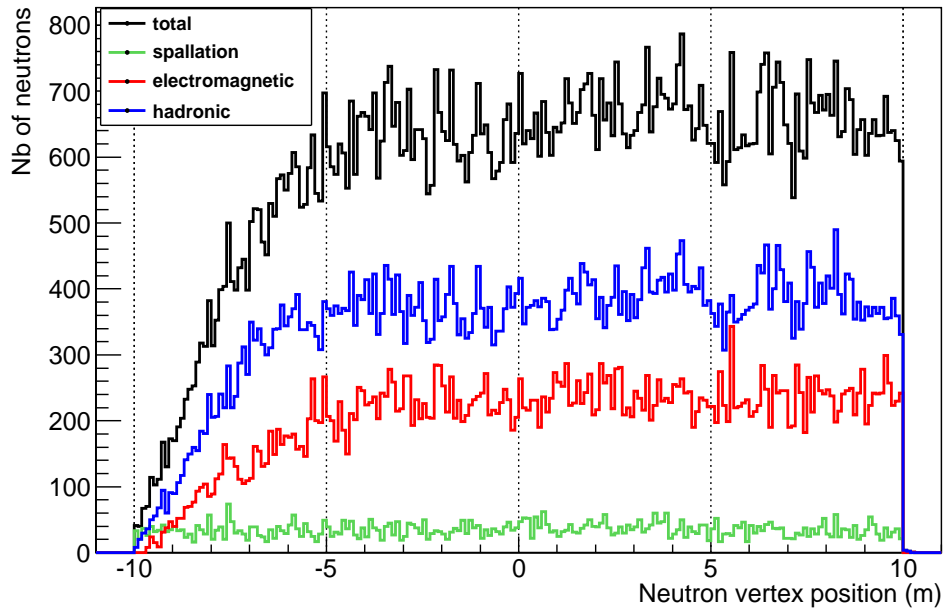


Figure 4.7: *Number of neutrons induced by muons as a function of their creation position in liquid scintillator. Bins are 10 cm wide.*

was repeated for several physics lists called QGSP_BIC_HP, QGSP_BERT_HP and QGSC. The description of these physics lists has been given in section 3.2.3. In table 4.2 are reported the values of the neutron yield got from a linear fit in the central part of the block. These values are also plotted in figure 4.12 as a function of the atomic weight of the material under investigation (or average atomic weight for compounds). It is obvious that on average the neutron rate increases with the atomic weight of material, but no exact parametrization was found which would explain the behaviour for all elements and compounds. The general trend can be fitted by a simple power-law:

$$R_n = b \times A^\beta \quad (4.3)$$

where A is the atomic weight, $b = (2.66 \pm 0.13) \times 10^{-5}$ and $\beta = 0.92 \pm 0.02$ for the physics lists QGSP_BIC_HP. The values found with this version 9,3 of Geant4 are a little bit different from the values ($b = (3.0 \pm 0.4) \times 10^{-5}$ and $\beta = 0.82 \pm 0.03$) presented in reference [64] obtained with the Geant4 version 6.2. The

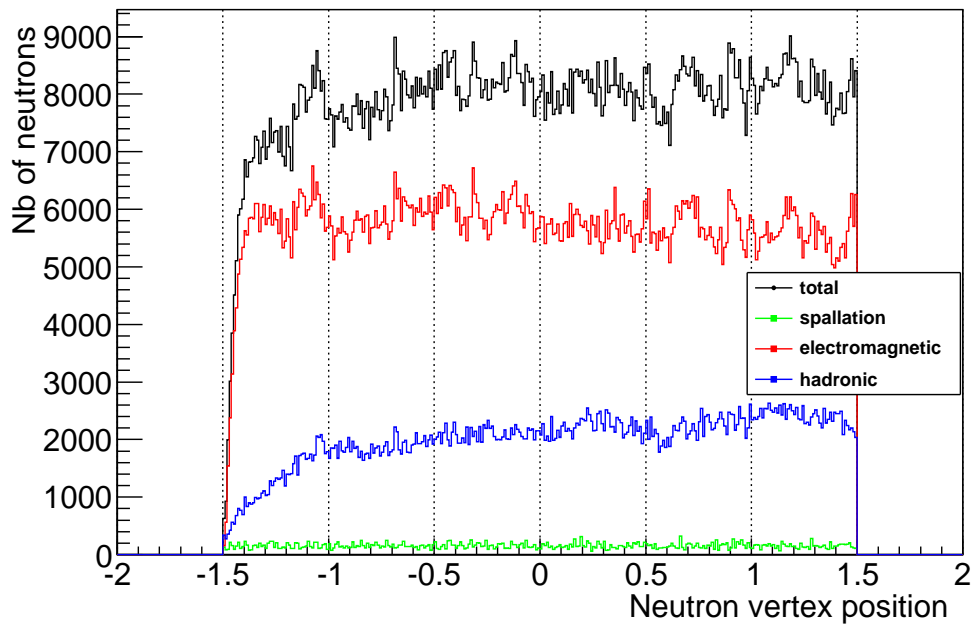


Figure 4.8: *Number of neutrons induced by muons as a function of their creation position in lead.*

increased neutron yield for high atomic weight could reflect the effort of the Geant4 collaboration to improve the agreement between simulations and experimental data for the experiment NA55 at CERN, already discussed in section 4.1.2.

Another characteristic that the chosen physics list can influence is the neutron energy spectrum. Energy spectrum of muon-induced neutrons is substantially harder than that from fission or (α ,n) reactions showed in section 1.2.1. In figures 4.11 top and bottom are plotted the neutron kinetic energy when they are produced, respectively, in liquid scintillator and lead for the three physics lists taken into account. Two important conclusions can be derived from these two figures. The first is that the neutron energy spectrum depends strongly on the target material. All enhancement of the neutron production in lead occurs at neutron energies below 20 MeV. This characteristic is due to photons emitted by muons in the electromagnetic showers that interact inelastically with the material nuclei. This is explainable considering that the muon cross section for electromagnetic

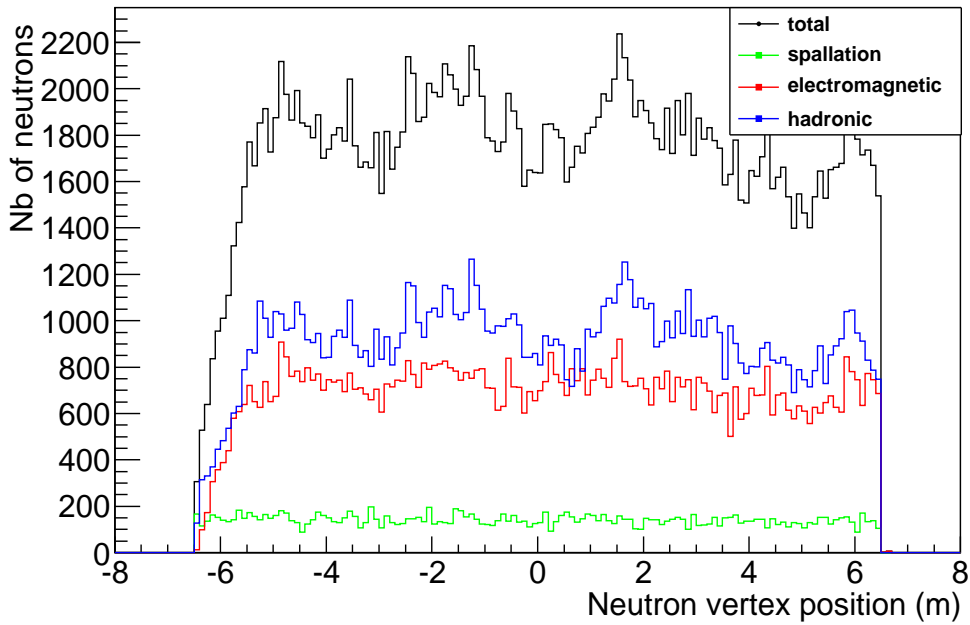


Figure 4.9: *Number of neutrons induced by muons as a function of their creation position in rock.*

interactions is proportional to Z^2/A . Hence, high- A targets give higher neutron yield than low- A ones, as deducible from equation 4.3 and graphic 4.12, but with a softer energy spectrum. Similar conclusion was derived also in ref. [62], [73], [64] and [74]. In figures 4.13 the physics list called QGSP_BIC_HP has been compared to the other two under investigation. The plots show the ratio between physics lists for each bin of the initial neutron energy spectrum in liquid scintillator and lead separately. That leads us to the second conclusion: there is a substantial agreement between the physics lists that are modelled by the Bertini cascade and the Binary cascade, in particular, for neutron below 1 GeV, deviations are smaller than 20%. On the other hand the QGSC has bigger deviations with respect to the previous ones especially for lead in the $10 \div 100$ MeV region. Big deviations for neutron with energy higher than 1 GeV is due to low statistic for the production of neutrons of such energy.

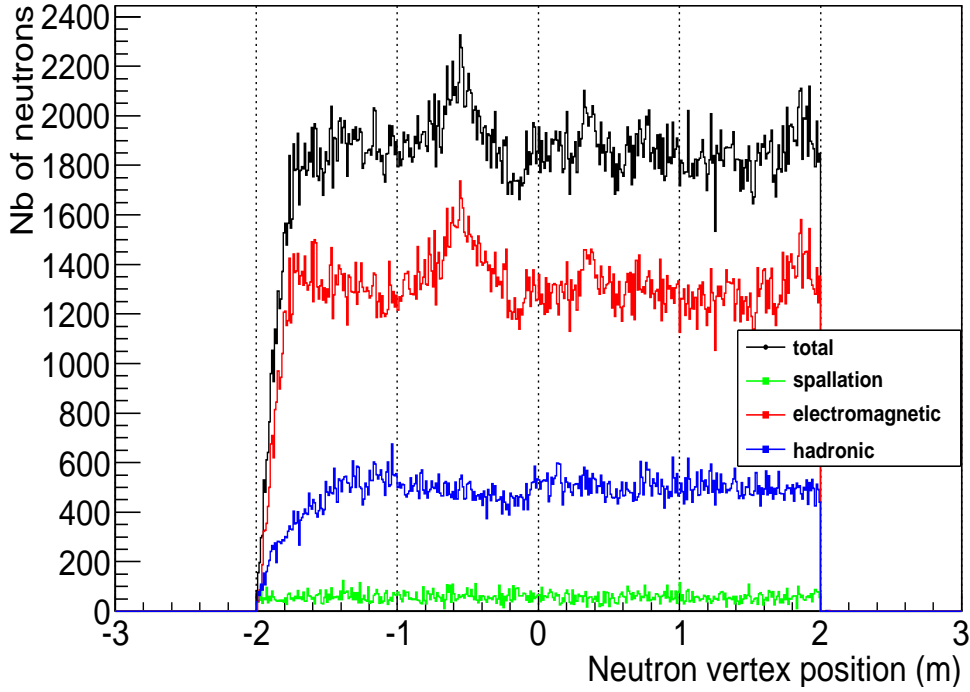


Figure 4.10: *Number of neutrons induced by muons as a function of their creation position in iron.*

material	BIC	BERT	QGSC
lead	3.55×10^{-3}	4.13×10^{-3}	3.27×10^{-3}
iron	1.19×10^{-3}	1.44×10^{-3}	1.15×10^{-3}
rock	3.37×10^{-4}	3.66×10^{-4}	4.09×10^{-4}
scintillator	1.95×10^{-4}	2.07×10^{-4}	2.62×10^{-4}

Table 4.2: *Neutron yield in different kind of material for three physics lists.*

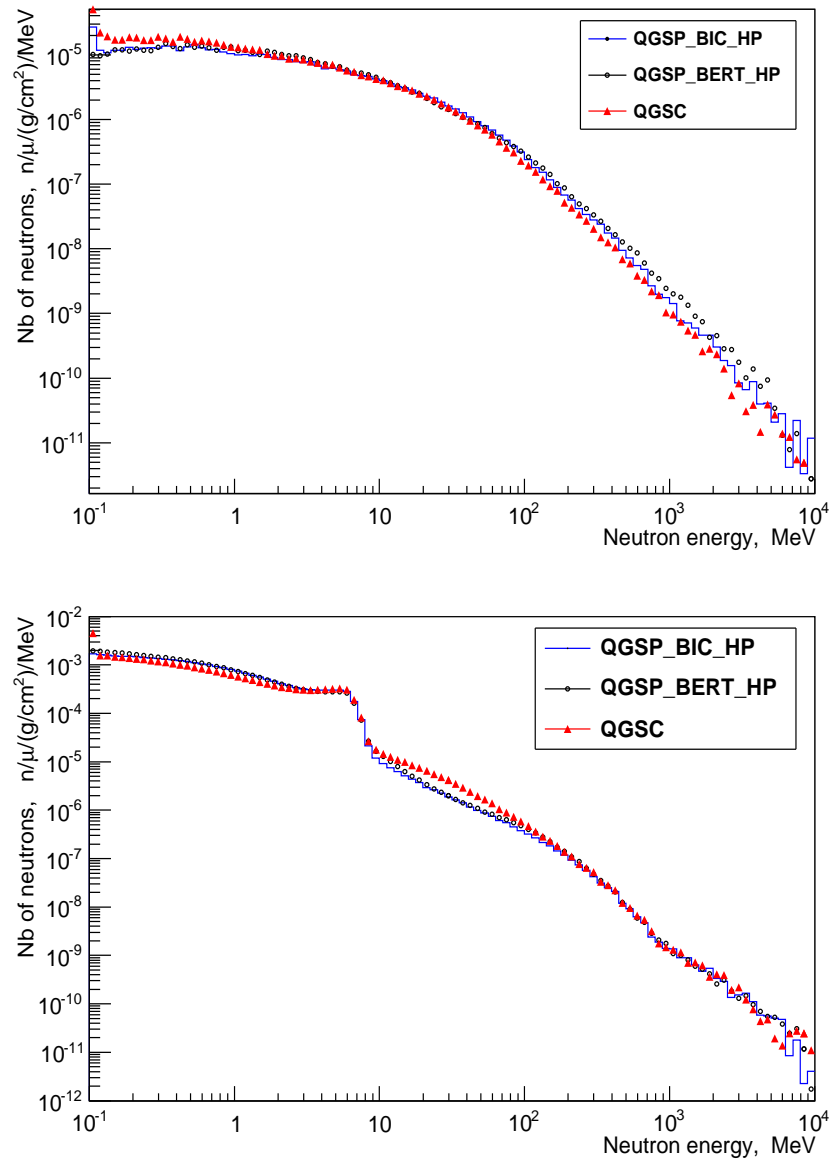


Figure 4.11: Neutron energy spectra from muons with LNGS energy spectrum in liquid scintillator (top) and lead (bottom) as obtained with three different physics lists.

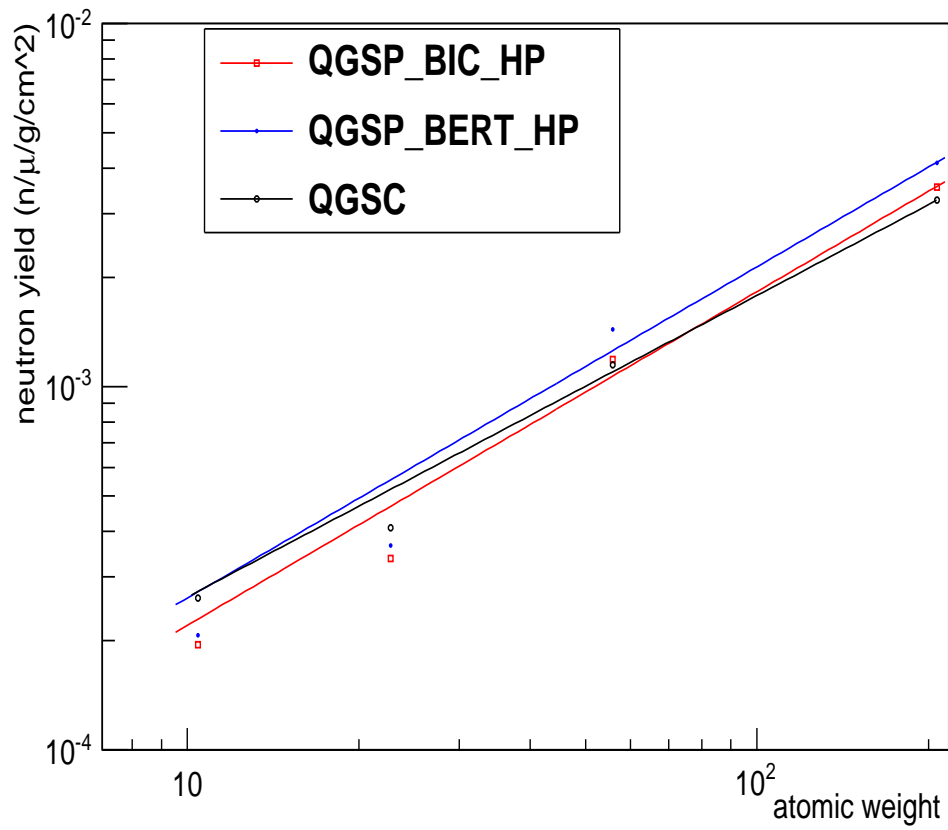


Figure 4.12: *Dependence of the neutron yield on the average atomic weight of the material for muons with energy spectrum a LNGS and mean energy of 270 GeV for the three different physics lists.*

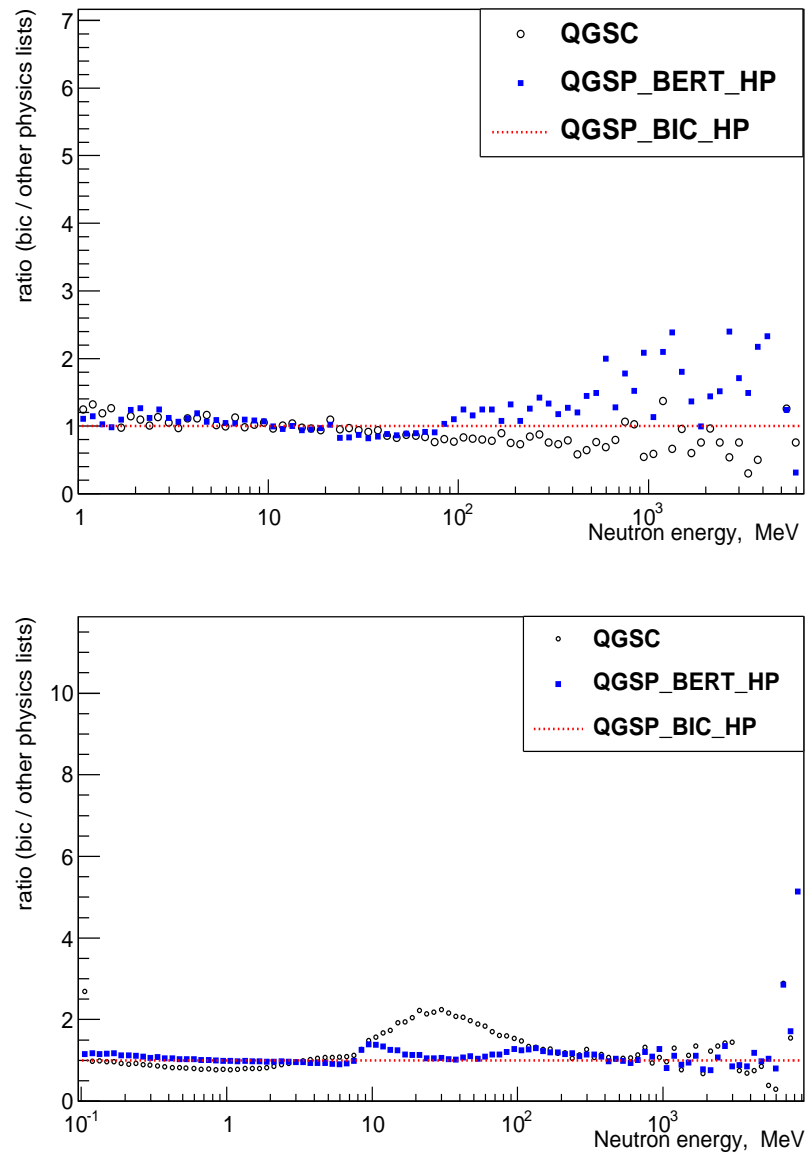


Figure 4.13: *Percentage variation among the physics lists for the initial neutron energy spectra in liquid scintillator (top) and lead (bottom).*

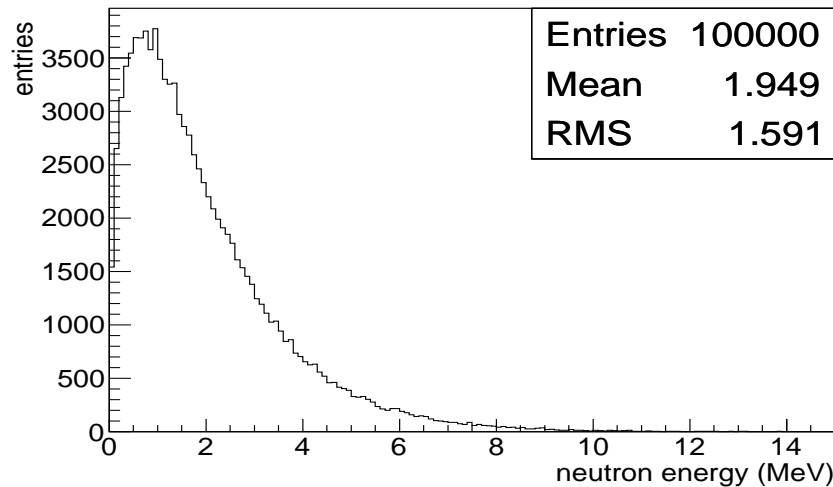


Figure 4.14: *Energy spectrum of neutrons from fission events of the ^{252}Cf source.*

4.3 Neutrons from a ^{252}Cf source

Another test has been performed in order to evaluate the capability of the MC simulation to estimate the mean neutron capture time τ for two different positioning of the neutron source: in the center of a counter and in the LVD detector beside a portatank. This simulation has been performed with Geant4 version 7.1 but the results have to be considered valid also for last version 9.3 because the neutrons at these energies are described by the same physics.

The neutron source used in this measure is a ^{252}Cf source which has a mean life of 2.65 years and an activity of about 0.5 fissions per minute. In the 97% of cases the ^{252}Cf decays emitting α particles, while in the leftover 3% it makes a nuclear fission. The number of neutrons emitted for each fission is Gaussian with a mean value of 3.735 and a sigma of 1.08 [75]. The energies of these neutrons have been sampled on a Maxwell's distribution, plotted in figure 4.14. Coupled to the radioactive source there was a Surface Barrier Counter (SBC) which generates the fission trigger [76].

The amplified trigger signal is discriminated to separate fission events from α -decays before recording the fission time with the module C176 (ADC-TDC module already described in section 2.2). After each fission trigger the electronics records

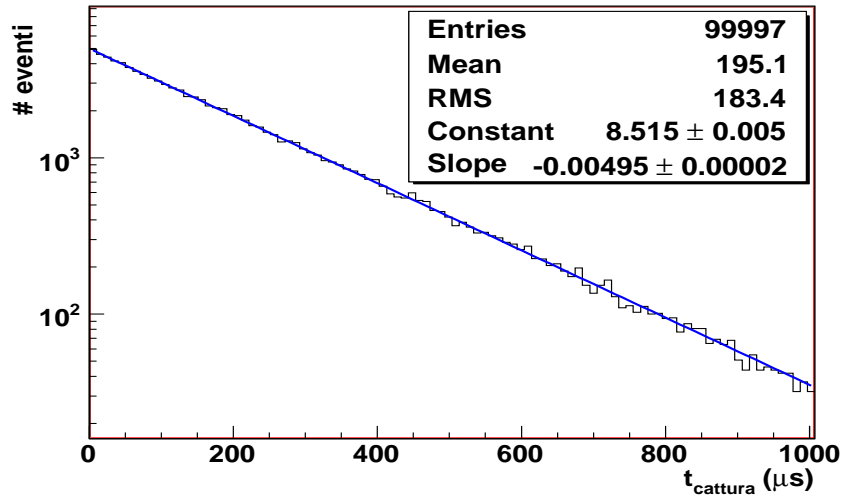


Figure 4.15: *Time distribution of the neutron capture for 1 MeV neutrons, generated in the center of tank and isotropic momentum.*

the time and charge of events that comes from the 3-fold coincidence of the PMTs for energy releases greater than the low threshold (set to 1 MeV). The time window for the events search is in the range $40 \div 500$ milliseconds after the trigger. In the case where the californium source is placed in the detector, the fission trigger lowers the threshold and allows the acquisition of LET signals in the whole portatank with the radioactive source.

4.3.1 ^{252}Cf source placed in the center of a tank

In this test the number of neutrons simulated is 10^5 and they are generated in liquid scintillator at the center of a tank. They are monochromatic with energies of 1 MeV and the angular distribution is isotropic. In figure 4.15 is plotted the neutron capture time obtained by simulation that gives the following value for the mean capture time:

$$\tau_{simG4} = (202.0 \pm 0.8)\mu s \quad (4.4)$$

τ_{simG4}	τ_{meas}	τ_{th}	τ_{simG3}
202.0 ± 0.8	202.3 ± 2.1	203	202.5 ± 0.9

Table 4.3: Mean capture time of neutrons obtained by simulations, theoretical calculation and experimental measurement.

This value of τ can be compared with the theoretical one got with the following relation:

$$\tau_{th} = \frac{1}{\sigma_c v_{th} N_H} = 203.1 \mu s \quad (4.5)$$

where the thermal speed of neutrons is $v_{th} = 2200$ m/s, the neutron capture cross section on Hydrogen $\sigma_c = 0.334$ barns and the the proton concentration in liquid scintillator is $N_H = 6.7 \times 10^{22}$ protons/cm³. Only protons have been taken into account because their cross section is two order of magnitude higher with respect to the carbon one. The measurement has been performed underground in the counter 1245 with the trigger logic over mentioned and the mean capture time is:

$$\tau_{meas} = (202.3 \pm 2.1) \mu s \quad (4.6)$$

The value obtained by simulation is in agreement with the measurement and with the theoretical calculation and moreover there is an older simulation in GEANT3 that provides the same mean capture time. All these values are summarized in table 4.3, where it is clear the validity of the LVDG4 code.

These results have been obtained for neutrons produced in the center of the tank, but neutrons can be produced everywhere in the liquid scintillator or in the detector . In reference [73] another simulation has been built where neutrons were generated uniformly in the liquid scintillator and the estimated mean capture time is $(181.8 \pm 07) \mu s$, about 20 μs lower than the previous one. This was understood to be due to geometrical effects.

4.3.2 ^{252}Cf source placed in the LVD detector

This test has been thought to verify if the MC simulation describes in the right way the behaviour of the τ found out in the measurement of the mean capture time of neutrons produced by a source placed on the side of a portatank inside the

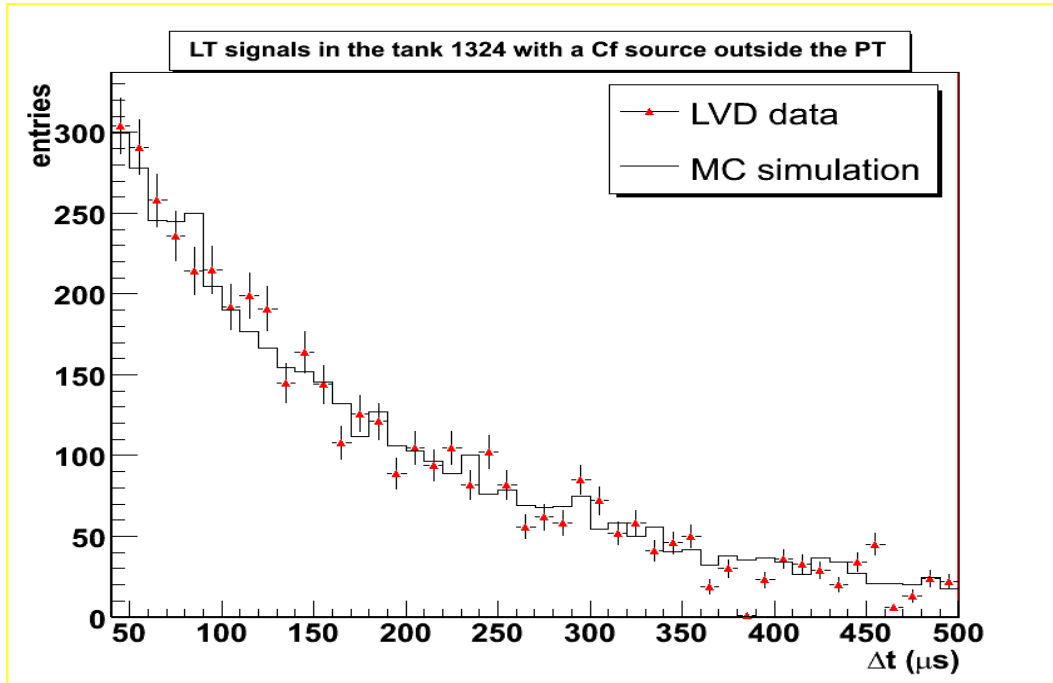


Figure 4.16: Time delay distribution of LET signals for MC simulation (black solid line) and experimental data (red triangles).

detector. The value measured is:

$$\tau_{meas,PT} = (148 \pm 10)\mu s \quad (4.7)$$

and it is $50 \mu s$ lower than the value measured in the center of a tank. The simulation confirms the τ measured with the source and gives:

$$\tau_{meas,PT} = (151 \pm 4)\mu s \quad (4.8)$$

In figure 4.16 is showed the expected time delay distribution of LET signals normalized to the experimental data. This low value is due to the presence of iron in the detector structure that has a neutron capture cross section that presents resonances for neutrons with energies above 1 keV and that reduce the neutron capture time capture time, even if iron is not a good neutron moderator.

4.4 Neutrons coming from the rock

In this study we have realized a MC simulation with Geant4 version 9.3 to evaluate the muon induced neutron flux in two different laboratories: LNGS and the Laboratoire Sotterraïne de Modane (LSM). We have also compared the neutron flux estimated for LNGS to the results showed in reference [4] got with the MC simulation code FLUKA.

4.4.1 Simulation description

The geometry of this simulation is quite simple because it has been taken into account only the rock around the experimental hall and 30 *cm* of concrete. Nevertheless we have had to consider several simulation features:

- The thickness of the rock: a very large thickness implies too much computing time, whereas a too small thickness underestimates the particle yield because cannot be fully developed the electromagnetic and hadronic shower.
- The rock composition: the neutron yield in the rock of both laboratories under investigation is quite the same even though the rock composition is different for the two sites. But the most important feature we need to figure out is the amount of Hydrogen present in the rock; it produces a reduction in the number of neutrons coming in the hall, and also a reduction in the mean energy of the incoming neutrons.
- The concrete thickness: the density, mean A value and composition is similar to the rock but there is Hydrogen and it is important to take into account the incoming neutrons

In order to evaluate the amount of rock we need to get the muon-induced showers totally developed, so the number of neutrons produced per unit of muon path length is constant, we made a small simulation in which we shoot muons with the LNGS energy spectrum on a block of rock of 12 *m* and we count the neutrons induced for every slice with thickness of 10 *cm*. It has been found that, as showed in figure 4.17*left*, at least 2 ÷ 3 *m* of rock are necessary to get the production

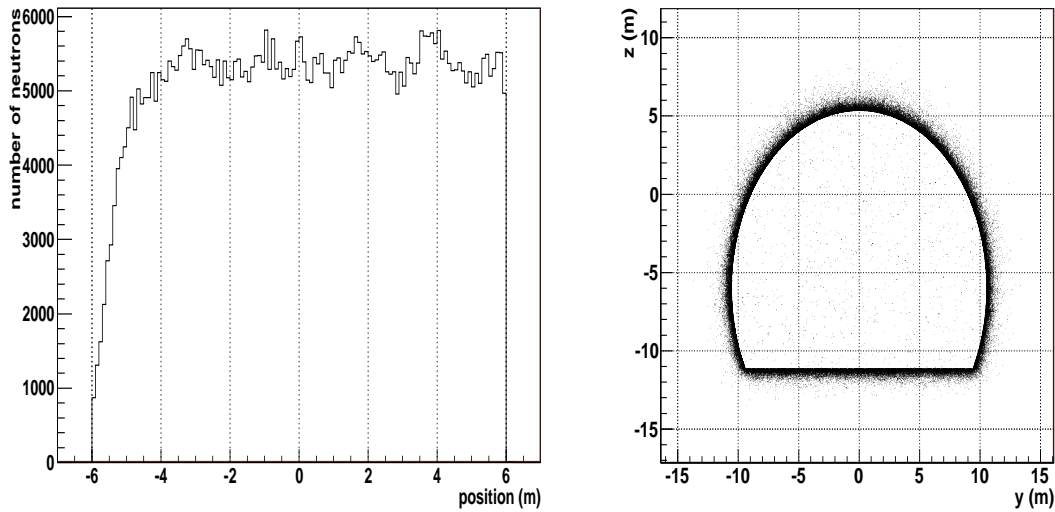


Figure 4.17: *left*: Number of neutrons produced in a 12 meters block of rock by muons crossing the bulk from left to right. The bin size is of 10 cm. *right*: Vertex of production of all neutrons entering the experimental hall.

constant. Therefore we have to take into account that neutrons can be induced far away from the hall walls. In this MC muons were generated at the lateral surface of a cylinder of rock with radius of about 19 m. The experimental hall is an elliptical cylinder with mean radius of 12 m and 100 m long, cut on the bottom to have the floor and the height is 18 m. Between rock and the hall we introduced 30 cm of concrete. In such way muons have to cross at least 7 meters of rock before entering the hall and, as showed in figure 4.17, all neutrons entering the hall are produced at a maximum depth of 5 m behind the rock surface. We used the pre-build Geant4 material for the concrete of both laboratories with the composition reported in the table 3.2, in which we show also the composition for the LNGS and LSM rock.

We used the two fast dedicated code (MUSIC and MUSUN), as explained in section 3.2.2, to get the cosmic muons energy spectrum and angular distribution at the underground laboratory level for both sites. The mean energy of the muons reaching the laboratories are about 275 GeV in the LNGS and 307 GeV in the LSM. These programs provides us the residual muon flux as well: that is about 1.17 and 0.23 μ/m^2h in the LNGS and LSM respectively. Both μ^+ and μ^- were

simulated, with a ratio μ^+/μ^- of about 1.3. To find the initial vertex of muons on the external rock surface, the following procedure has been applied:

- the muon direction is taken from the MUSIC and MUSUN codes
- for each muon a point is generated randomly over a circle perpendicular to the muon direction, with center in the middle of the hall and radius of 16 m (larger than the maximum dimension of the LVD detector).
- the muon initial vertex is provided by the intersection between the external rock surface and the line parallel to the muon direction that crosses the point sampled over the circle

Once the vertex and direction are known, muons are propagated through the rock and all secondary particles are generated and propagated as well. For this simulation 5×10^6 muons have been shot.

4.4.2 Neutron energy spectrum

The neutron energy spectrum is particularly controversial, with a wide range of results reported in theoretical calculations and in the few experimental measurements. In figure 4.18 (*top*) we show the initial energy spectrum of all muon-induced neutrons in the rock surrounding each laboratory. The distributions are normalized to the total number of neutrons and the shape is quite the same even if the rock compositions are different and the mean muon energy is a little bit higher at LSM ($\langle E_\mu \rangle \sim 306$ GeV) with respect to the LNGS ($\langle E_\mu \rangle \sim 275$ GeV). The energy spectrum of neutrons entering the hall is shown in figure 4.18 (*bottom*): they are very similar and they have the gaps due to resonances in the cross section of the elastic scattering on Oxygen. The presence of Hydrogen in the rock and in the concrete reduces the number of neutrons below 1 MeV and, more in general, its presence reduces the mean energy of neutrons coming from the rock. In this figure, the neutron energy spectra have been scaled to the respective muon flux at the underground laboratories.

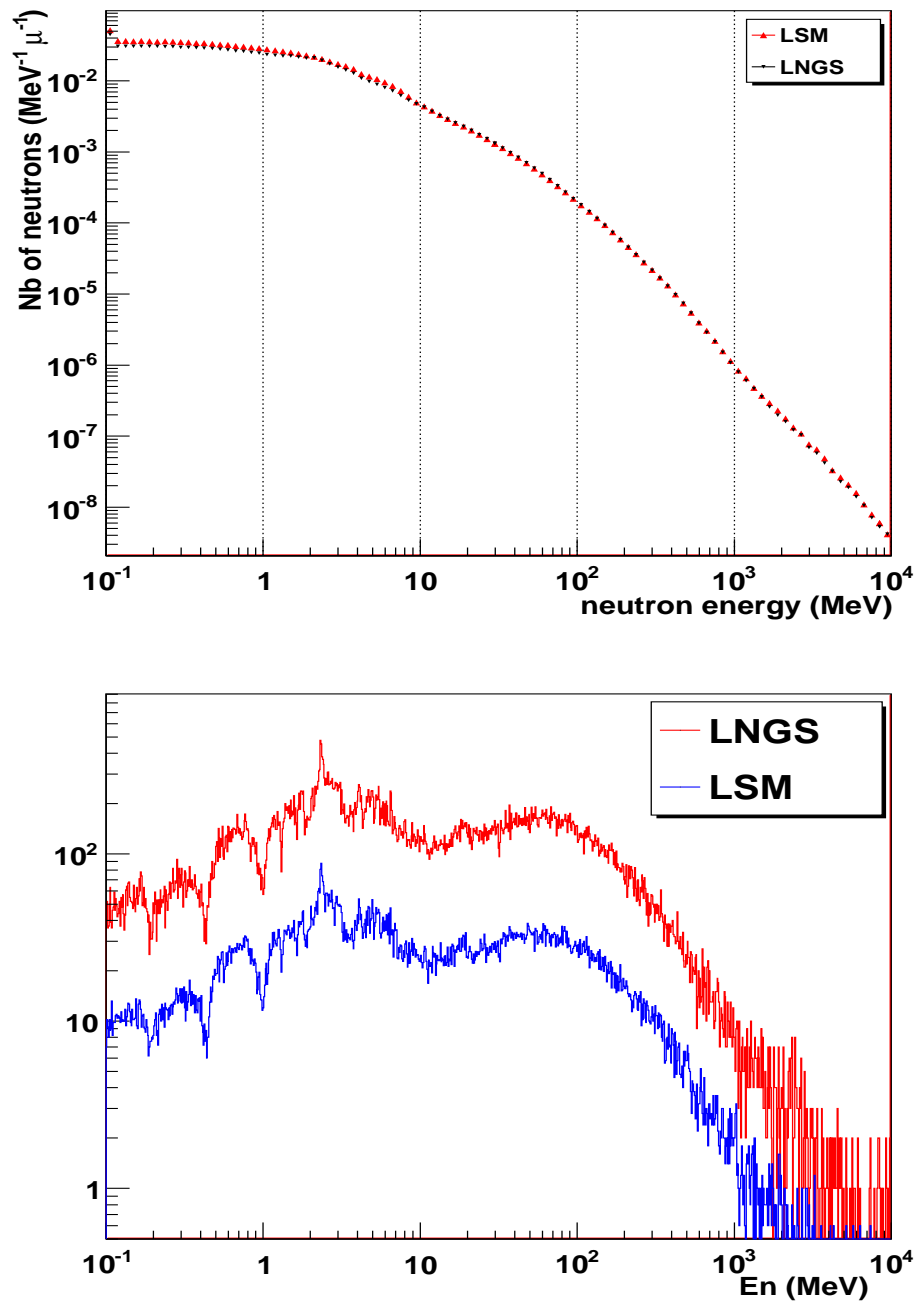


Figure 4.18: Initial energy of muon-induced neutrons (top) and the energy spectrum of neutrons entering the experimental hall scaled to the muon flux in the two sites (bottom) for both laboratories.

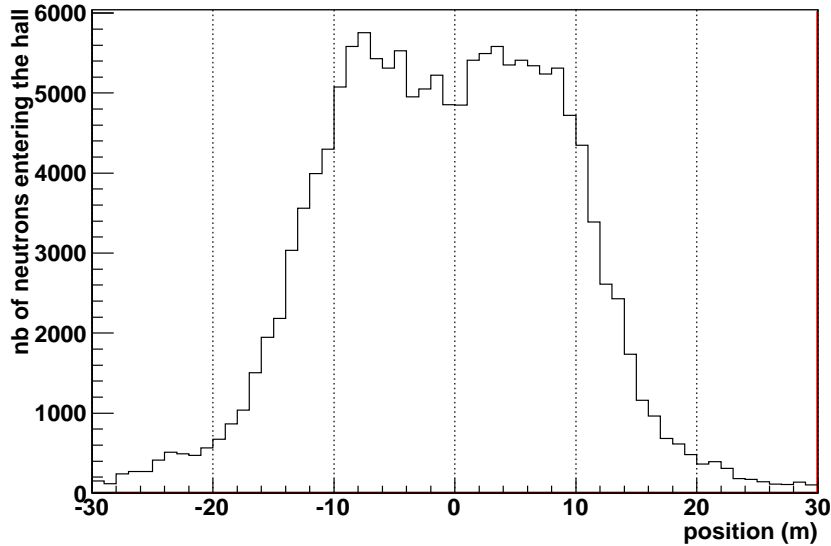


Figure 4.19: *Position of neutrons entering the experimental hall along the biggest axis of the hall itself.*

4.4.3 Neutron flux

The muon-induced neutron flux emerging from the rock into the cavern has been estimated for both the laboratories. In order to evaluate the neutron flux, we have taken into account only neutrons entering in the hall in the central part of the cavity, where the number of neutrons per unit surface is constant, as shown in figure 4.19. This is due to the fact that we are not sampling muons over the whole hall, but only on a circle centered in the middle of the hall and with a radius of 16 meters. The chosen region range between -10 and 10 m and both lateral and floor has been taken into account for this calculation. Moreover all neutrons are absorbed immediately after emerging the cavern walls in order to avoid back scattering. The values estimated by the simulation are presented in table 4.4. The integral flux above 1 MeV is 2.31×10^{-10} n/cm²/s and it is a factor 2 lower than the FLUKA prediction 4.27×10^{-10} n/cm²/s found in reference [4]. In figures 4.20 we show the differential neutron flux found out with FLUKA (*top*) and this simulation in Geant4 (*bottom*). In the former, the neutron flux has been exstimated with and

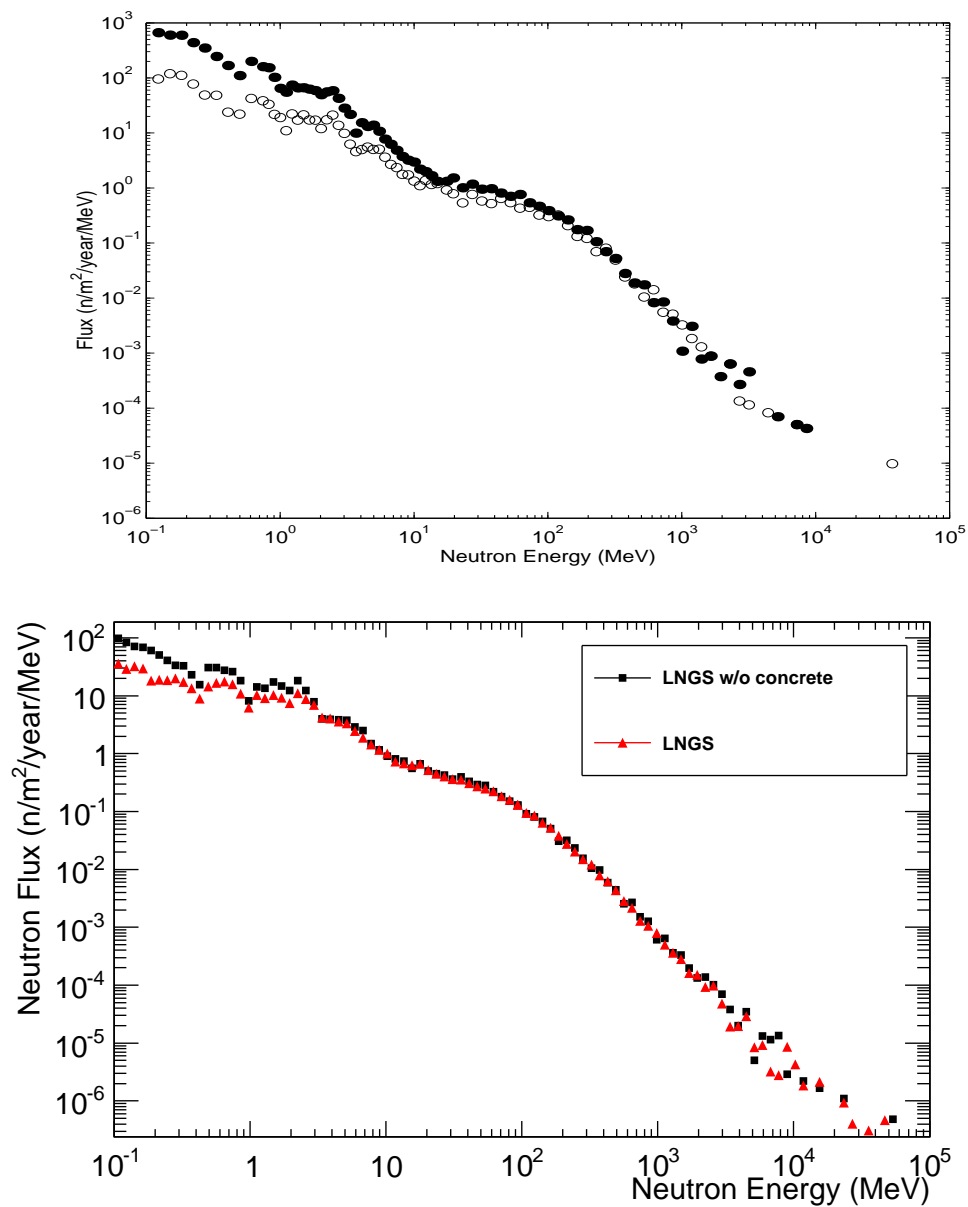


Figure 4.20: Flux of muon-induced neutrons entering the Gran Sasso hall obtained from the simulations based on FLUKA in reference [4] (top, without (\circ) and with (\bullet) back scattering) and from the simulation in Geant4 in this work (bottom, without back scattering, with (red) and without (black) concrete).

without the neutrons back scattering on the walls, while in the latter it has been considered onl the case without back scattering. For neutron energies above 3 MeV, fluxes of both simulations are in good agreement while under this threshold they diverge within a factor 2. This can be explained with the presence of Hydrogen in the concrete.

	LNGS w/o concrete	LNGS	LSM
$\phi_{n,total}$	7.18×10^{-10}	4.58×10^{-10}	8.62×10^{-11}
$\phi_{n,E_n>1MeV}$	2.66×10^{-10}	2.31×10^{-10}	4.59×10^{-11}
$\phi_{n,E_n>10MeV}$	1.22×10^{-10}	1.20×10^{-10}	2.42×10^{-11}

Table 4.4: Neutron fluxes in different energy range for the two laboratories in unit of $n/(cm^2s)$.

4.4.4 Neutron multiplicity

The number of neutrons produced per muon is called multiplicity and it is probably the least known quantity in the neutron production problem. In most cases muon spallation only happens once and produces only a few primary hadrons. But these hadrons can shower and generate secondary hadrons, including neutrons. Figure 4.21 shows the neutron multiplicity distributions in both laboratories from Geant4 and it has been found that in some cases the number of secondary neutrons exceeds 100. In reference [62] it has been proposed the following empirical parameterization:

$$\frac{dN}{dM} = A(e^{-A(E_\mu)M} + B(E_\mu)e^{-C(E_\mu)M}) \quad (4.9)$$

where M is the multiplicity and

$$\begin{aligned} A(E_\mu) &= 0.085 + 0.54e^{-0.075E_\mu} \\ B(E_\mu) &= \frac{27.2}{1 + 7.2e^{-0.076E_\mu}} \\ C(E_\mu) &= 0.67 + 1.4e^{-0.12E_\mu} \end{aligned}$$

We have tried to fit the distribution using the mean muon energy at the laboratories but it does fit the distribution. Unfortunately it is not easy to measure the neutron

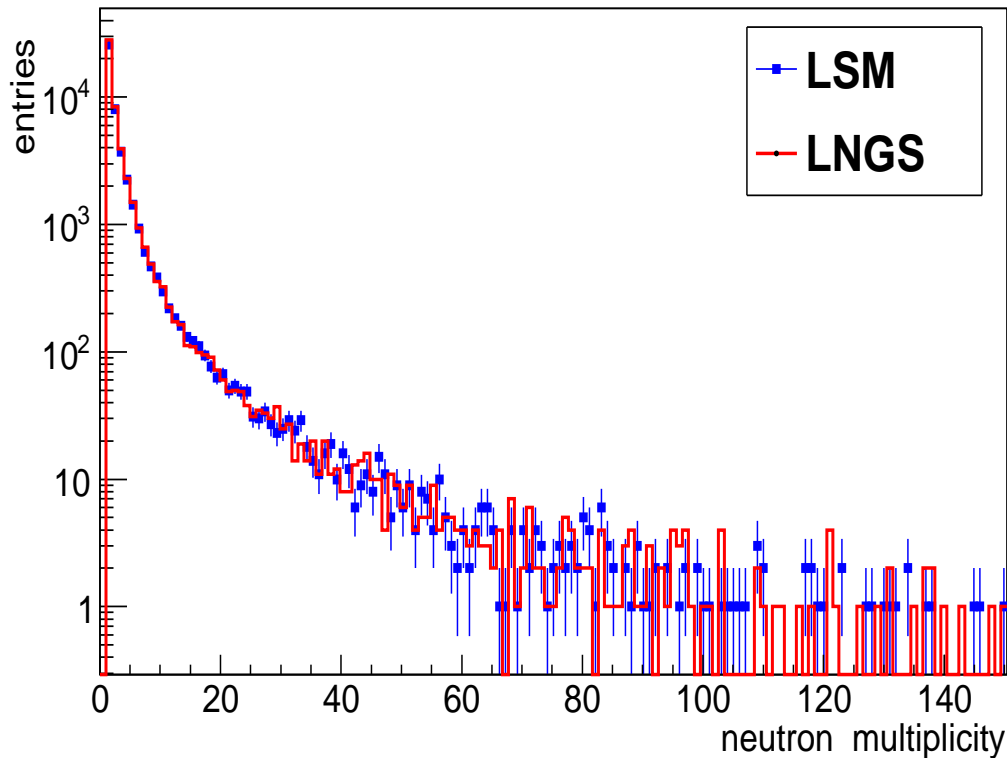


Figure 4.21: *Multiplicity of neutrons entering the experimental hall in both laboratories.*

multiplicity coming from the rock because the detector itself can produce secondary neutrons by electromagnetic and hadronic showers originated in the rock and that reach the cavity.

4.4.5 Neutrons generation processes

Muon-induced neutrons are produced in several physical processes. They can be produced directly by muon spallation or, mainly, by hadronic and electromagnetic showers induced by muons. In table 4.5 the contribution of each process is presented for the two rock and concrete samples. These percentages are different from the ones forecasted by FLUKA, even if the differences are smaller with respect to Geant4 version 7.0. In general, Geant4 shows enhanced neutron

	concrete	LSM rock	LNGS rock	LNGS rock [4]
μ -spallation	6.5	6.1	7.6	5.0
hadronic shower	48.9	51.0	54.4	74.3
e.m. shower	44.6	42.9	38.0	20.7

Table 4.5: *Physical processes for neutron production from cosmic-ray muon.*

photoproduction in electromagnetic cascades in light materials, while for heavy elements, FLUKA produces more neutrons than Geant4 in both electromagnetic and hadronic cascades [64].

Chapter 5

An application: LVD Core Facility

The code LVDG4 has been applied to establish the performances of a region inside the LVD detector that could host a dark matter experiment. The reason for finding a volume inside LVD is the low background level that characterizes this region for gammas and neutrons from radioactivity, and the possibility to use LVD as a muon veto that reduces the background due to fast neutrons induced by muons.

5.1 LVD core facility

Many experiments looking for dark matter are aiming to get the ton scale in the next future. However, it is well known that scaling dark matter detectors to higher mass is not a sufficient condition for sensitivity and that an equally important condition is to simultaneously keep the background low. As already written in previous sections, fast neutrons induced by muons represent the ultimate background for these kind of experiments. In particular the Gran Sasso laboratory is the one with the highest concentration of dark matter (DM) experiments. Furthermore, the sensitivity goal of DM searches is such that greater depths than that of Gran Sasso are required.

For such reasons it has been proposed to use the existing structure of the LVD experiment as an active shield and muon veto for hosting a next generation of DM experiment. Without affecting its main purpose of SN neutrino telescope, a

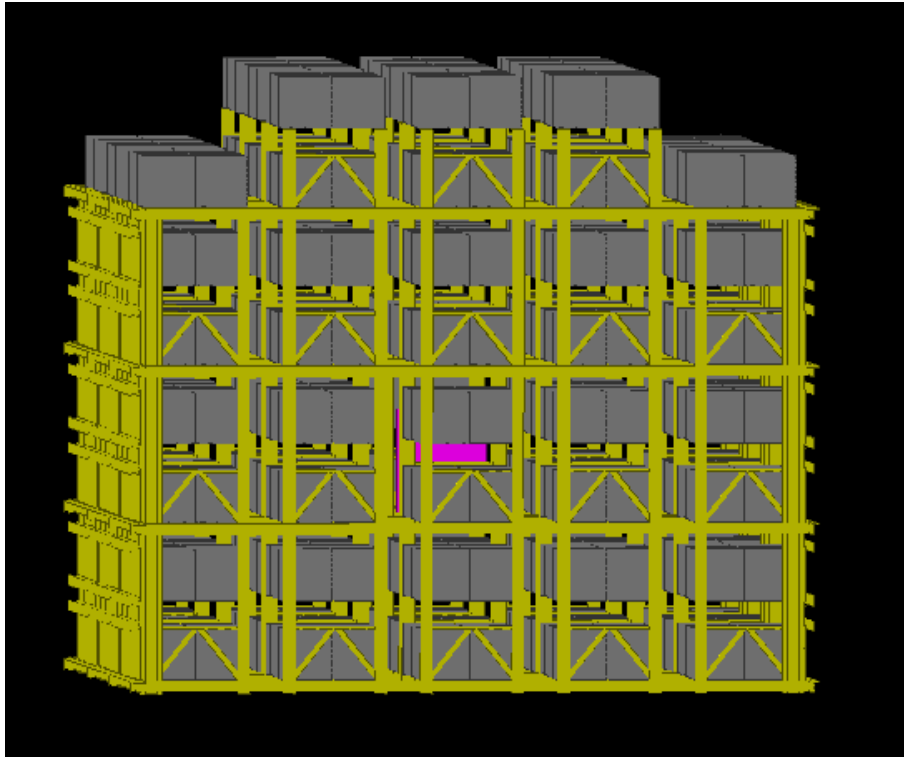


Figure 5.1: *Front view of the LVD detector with the LVD core facility highlighted in purple in the inner part of the detector.*

region in the most internal part of the detector has been identified. The empty volume can be obtained removing 2 modules and this operation would leave a space with dimension of $2.1 \times 6.2 \times 2.8 \text{ m}^3$, called LVD Core Facility (LVD-CF), as showed in figure 5.1. This volume is the minimum required for an 1 ton dark matter experiment. The background is due to gammas from radioactivity, the neutrons from (α, n) reactions and fission and muon-induced fast neutrons.

The measurement of gamma-ray induced background in the LVD-CF has been obtained by a set of of measurements carried out with a portable 2-inch NaI detector. As showed in figure 5.2, the gamma ray intensity inside the LVD-CF is reduced by a factor greater than 10 with respect to the one measured outside the LVD detector. From this result it is drawn that the overall structure of the experiment, which is made out of 1 kt of iron, is by itself rather clean, and act as a shield against the gamma ray flux coming from the Hall A walls.

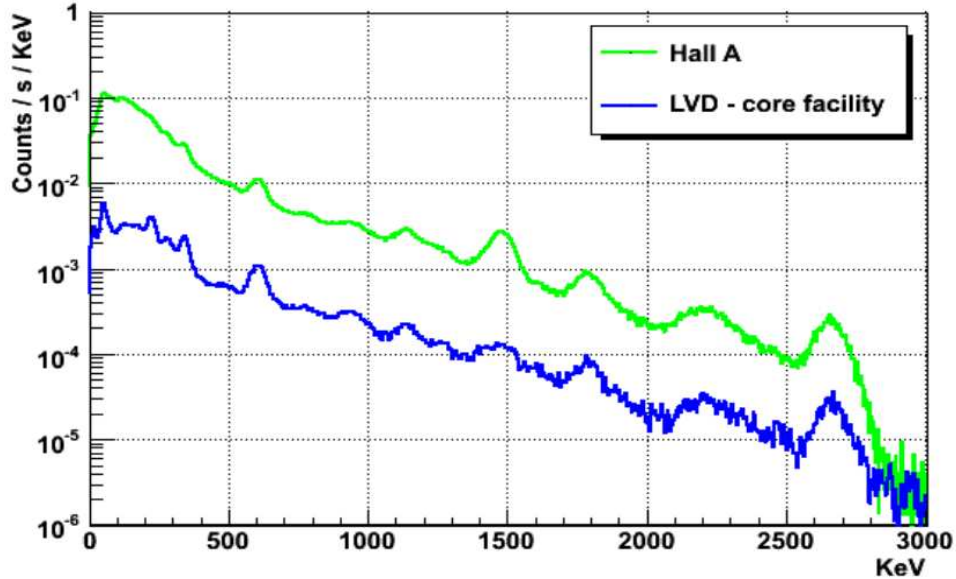


Figure 5.2: *Gamma ray energy spectrum measured inside the LVD-CF (blue line) and in the hall A (green line).*

For what concerns the neutrons from radioactivity, a simulation has been developed to evaluate the shielding power of LVD and the attenuation factor. The simulation is described in reference [30] and the conclusion is that the attenuation factor of LVD to radioactivity neutrons with energy above 1 MeV is $Q = 35.9 \pm 0.4$. This simulation has pointed out that most of the neutrons which reach the LVD-CF have been generated near a corridor, especially the corridors between the 3 towers and in general all the ones close to the LVD-CF. This confirms that LVD is a good neutron moderator. Considering the neutron flux due to radioactivity inside the Hall A, as estimated in reference [4], the neutron flux inside the LVD-CF has been evaluated $\Phi_n(E_{kin} > 1\text{MeV}) = (1.6 \pm 0.4) \times 10^{-8} \text{ n/cm}^{-2}\text{s}^{-1}$.

While it is relatively easy for LVD to moderate and capture neutrons from radioactivity with energy up to about 10 MeV, a different approach is needed for the more energetic ones. For this reason we developed a detailed Monte Carlo simulation of the detector and the rock that surrounds it, to evaluate the active vetoing and shielding power of LVD. In the next sections the simulation code and the results obtained will be described.

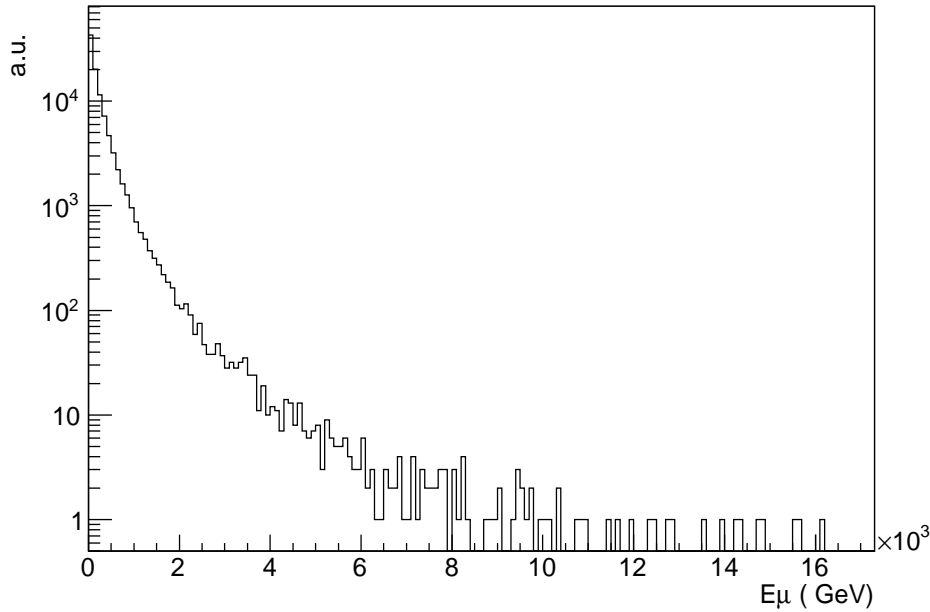


Figure 5.3: *Muon energy spectrum at LNGS.*

5.1.1 LVD-CF simulation description

The simulation used for studying the performances of the LVD-CF is based on version 7.3 of Geant4. There is little difference between the physics list adopted in this version of the LVDG4 code and the physics list used at present. The differences consist in the neutron yield, but not in the neutron energy spectrum. Anyhow the main items under investigation are the shielding power and active vetoing of the LVD-CF, comparing the muon-induced neutron flux at the surface of the core facility with the one got on the same surface without the LVD detector. Also a comparison in the deepest existing underground laboratories (Sudbury) has been done with the neutron flux. As explained in section 3.2.2 cosmic muon have been generated with energy spectrum and angular distribution sampled accordingly to what is expected in the LNGS underground laboratory and showed in figure 5.3 and 5.4 respectively.

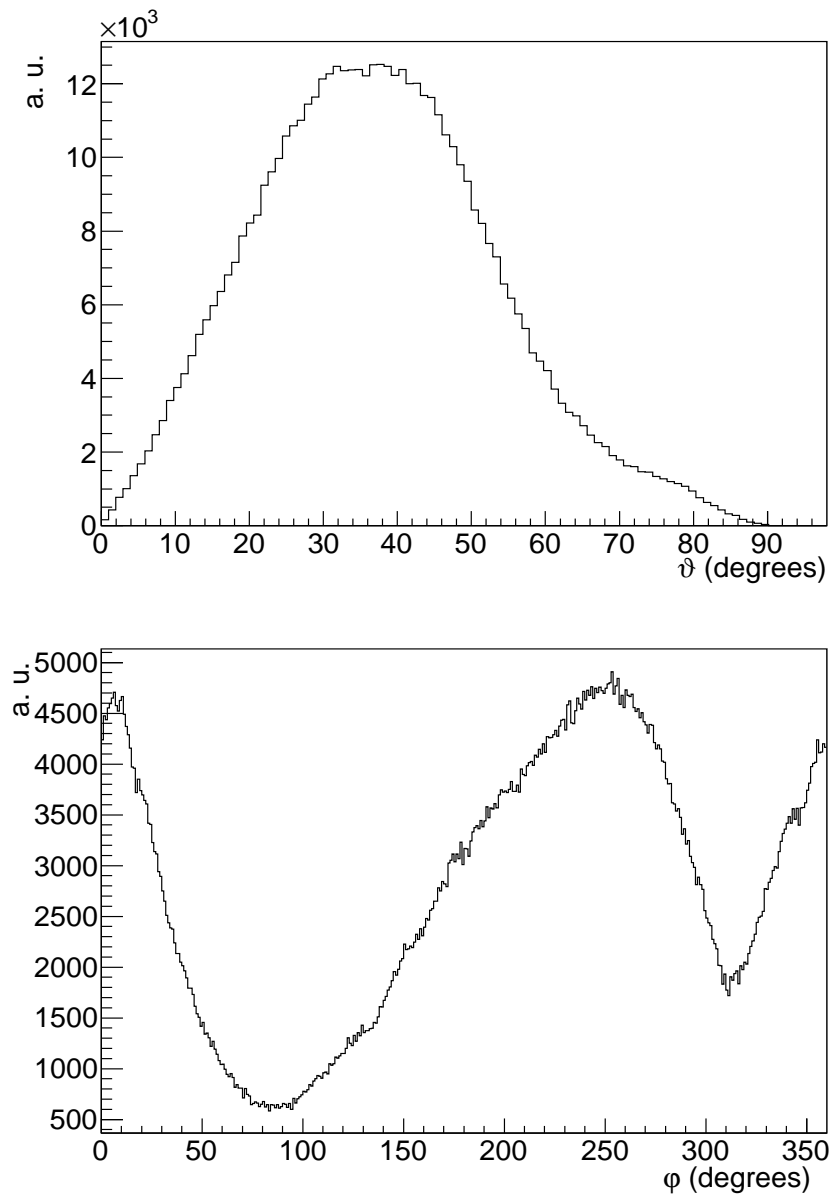


Figure 5.4: *Muon angular distribution at LNGS for the zenith angle (top) and the azimuthal angle (bottom).*

In order to evaluate the LVD shielding power two simulation have been done: in the first one the neutron flux on the surface of the core facility has been evaluated without simulate the LVD detector but only the rock surrounding the experimental hall, in the second one the detector around the core facility has been simulated without taking into account its active vetoing ability. Another simulation has been run launching muons with energy spectrum and angular distribution at Sudbury ($\langle E_\mu \rangle \sim 330$ GeV) to evaluate the number of neutrons that reach the surface of the core facility. The distribution of the azimuthal angle of muons that reach the Sudbury underground laboratory is flat because the laboratory is located in a deep mine and it has a more homogeneous shielding profile with respect to the laboratory located under a mountain as the LNGS. In this simulation only the rock has been taken into account and the shape of the experimental hall has been assumed to be the same in both laboratories. The rock composition at Sudbury is reported in table 3.2. The muons generated in each simulation are 5×10^6 , that taking into account the radius of the circle over which they are sampled and the muon intensity at LNGS, correspond to about 8 months of data acquisition.

5.1.2 LVD-CF simulation results

Because of its large volume, LVD can detect muons even very far from the LVD-CF: the LVD external dimensions, indeed, are $13 \times 22.7 \times 10$ m³ called LVDbox. Nevertheless inside LVD there are gaps and corridors, thus some muons can cross this volume without being detected. A muon is defined *tagged* if the are at least two scintillation counters that have recorded a high threshold (HT) signal ($E_{HT} > 5$ MeV) in time coincidence within the 250 ns. About 85% of the muons that hit the LVDbox are tagged. Hereafter neutrons induced by tagged muons will be called *tagged* as well, while neutrons induced by muons not detected will be called *untagged*.

For all the simulated muons, the number of neutrons that enter the LVD-CF when the parent muon is untagged is just 342 and they represent the 3.5% of all the neutrons entering the LVD-CF. Only 25% of untagged ones come from muons that cross the LVDbox and go through a corridor; the remaining 75% are neutrons produced in the rock around the detector that go inside the LVD-

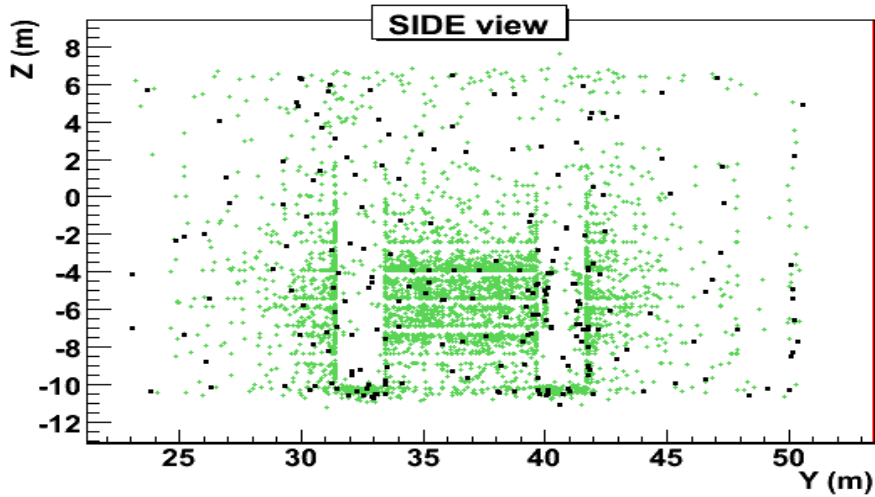


Figure 5.5: *Side view of the positions where the neutrons that enter the LVD-CF are produced. In green those neutrons whose parent muon is tagged, while in black the untagged ones.*

CF mainly through one of the gaps as can be seen in figures 5.5 and 5.6 where the side, front and top view are showed. In particular the positions of the whole neutrons that enter the LVD-CF are plotted, subdivided in tagged (green points) and untagged neutrons (black squares). Most of the tagged neutrons are produced by the detector itself and close to the LVD-CF. In figures 5.7 are plotted the muon distance with respect to the center of the LVD-CF for every muon that induces at least a neutron able to reach the core facility in the case when the parent muon is tagged (*top*) and untagged (*bottom*). In the first distribution the muons have a mean distance of about 5 meters and a long tail with distances up to 15 meters. The latter muons can be detected only in the case they induce electromagnetic or hadronic showers that enter the experimental hall and then detected. In the second distribution the mean muon distance is 10 meters, so most of them do not cross the LVDbox and this leads to the conclusion that even if a muon veto as large as the hall would be available, there would be a residual flux of neutrons induced by untagged muons.

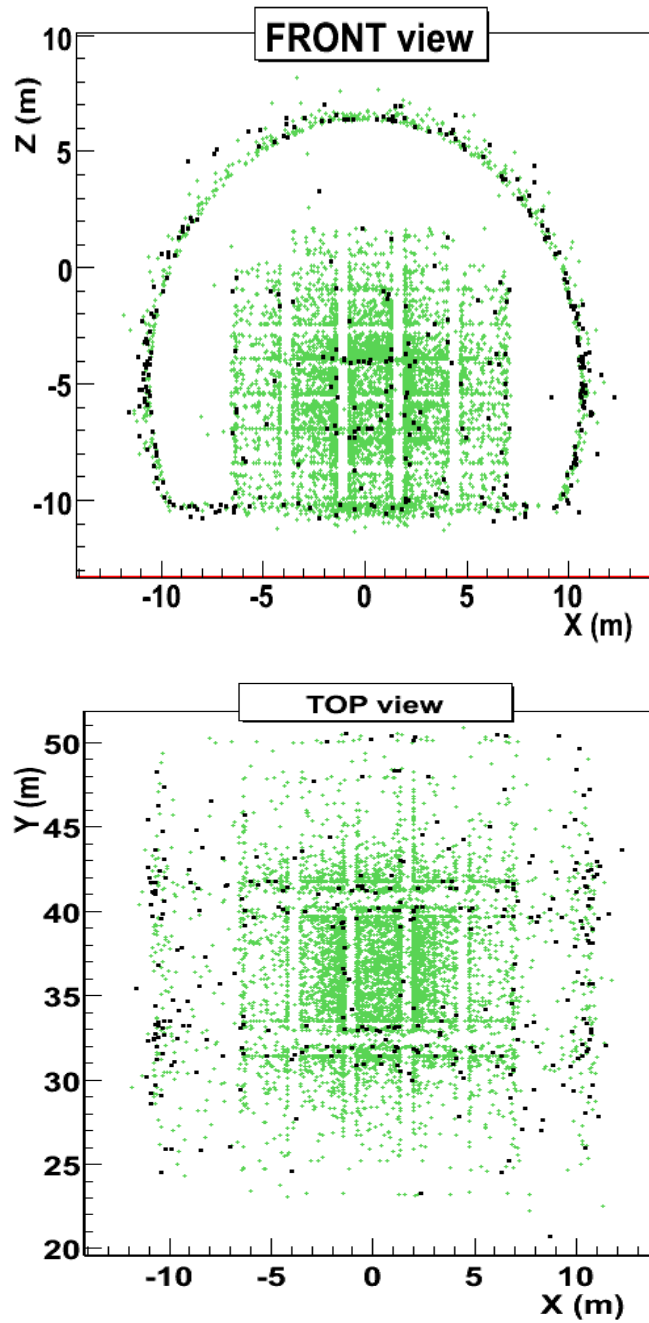


Figure 5.6: *Front view (top) and top view (bottom) of the positions where the neutrons that enter the LVD-CF are produced. In green those neutrons whose parent muon is tagged, while in black the untagged ones.*

In table 5.1 are reported the neutron fluxes for four different Monte Carlo simulation developed in order to evaluate the active vetoing and shielding power of LVD. The latter can be evaluated considering the differences in the flux at LVD-CF surface with and without the LVD detector (as passive shield) around the LVD-CF itself. From the first two columns, it is possible to see that LVD is able to reduce the total neutron flux by a factor of 3, but it leaves unchanged the flux for neutrons with an energy higher than 1, 10 and 100 MeV. This effect is mainly due to the fact the LVD is constituted by 1000 ton of liquid scintillator and so it is a good neutron moderator but on the other side, the 1000 ton of the iron support structure produce a large number of neutrons close to the LVD-CF reducing the shielding power for high energy neutrons. The third column shows that when LVD acts as muon veto it is possible to reduce the muon neutron flux by a factor 50. A similar MC simulation as been developed for the Sudbury site, considering in details its depth, rock composition and cosmic muon flux. The resulting muon-induced neutron flux, reported in the forth column, is comparable to what is got in the LVD-CF, using LVD as a veto. This result makes the muon-induced neutron background in the LVD-CF equivalent to that of the deepest existing underground laboratories, i. e. Sudbury (6020 m w.e.).

In dark matter searches, elastic scattering of high energy neutrons produces nuclear recoils within the expected energy range of interactions from Weakly Interacting Massive Particles (WIMPs). The rate expected from such events in the energy range of interest is quite low for the current generation of dark matter experiments based on liquefied rare gases, which have only a few kilograms of active material. But with projects under way to build detectors with hundreds or thousands of kilograms, the precise knowledge of this neutron flux becomes paramount for the design of the detectors [68]. A detector with good spatial resolution can resolve the locations of multiple neutron elastic interactions, which occur on average several cm apart. These are not regarded as irreducible background since they should not be caused by WIMPs [64]. High energy neutrons can give a single scatter in the sensitive part of the dark matter detector, so it is important to know not only the neutron flux at the LVD-CF surface but also the energy spectrum of the untagged neutrons entering the LVD-CF. The number of neutrons with energy larger than 10 MeV is about 1 per week. In terms of flux this corresponds

neutron flux	LNGS hall	LVD passive	LVD as μ veto	Sudbury hall
Φ_{total}	1.78	0.60	0.0220	0.0337
$\Phi(E_n > 1MeV)$	0.30	0.030	0.0066	0.0048
$\Phi(E_n > 10MeV)$	0.11	0.10	0.0023	0.0015
$\Phi(E_n > 100MeV)$	0.03	0.03	0.0005	0.0004

Table 5.1: Neutron fluxes at the LVD-CF surface given in unit of $10^{-9} \text{ cm}^{-2} \text{ s}^{-1}$.

	mean arrival time	up to
t (all energies)	152 μs	25 ms
t ($E_n > 1MeV$)	174 ns	2.1 μs
t ($E_n > 10MeV$)	89 ns	400 ns
t ($E_n > 100MeV$)	74 ns	250 ns

Table 5.2: Arrival time of tagged neutrons in the LVD-CF.

to $2.3 \times 10^{-12} \text{ n cm}^{-2} \text{ s}^{-1}$. The neutron energy spectrum from tagged (*top*) and untagged (*bottom*) muons are shown in figure 5.8.

Another important characteristic to be evaluated in order to consider LVD a good active veto system is the fraction of dead time that it introduces. In table 5.2 are reported the arrival time of tagged neutrons as a function of the energy at the LVD-CF. In figures 5.9 the time distribution of neutrons with $E_n > 1 \text{ MeV}$ (*top*) and $E_n > 100 \text{ MeV}$ (*bottom*). The maximum delay between the neutron arrival time and the parent muon, for neutrons with energy higher than 10 MeV, is 400 ns. Thus the dead time introduced when using LVD as a veto is well below 1%, while taking into account all neutrons the maximum arrival time is 25 ms that, considering the muon rate detected by LVD of 0.1 Hz, gives the maximum fraction of dead time is 2.5%.

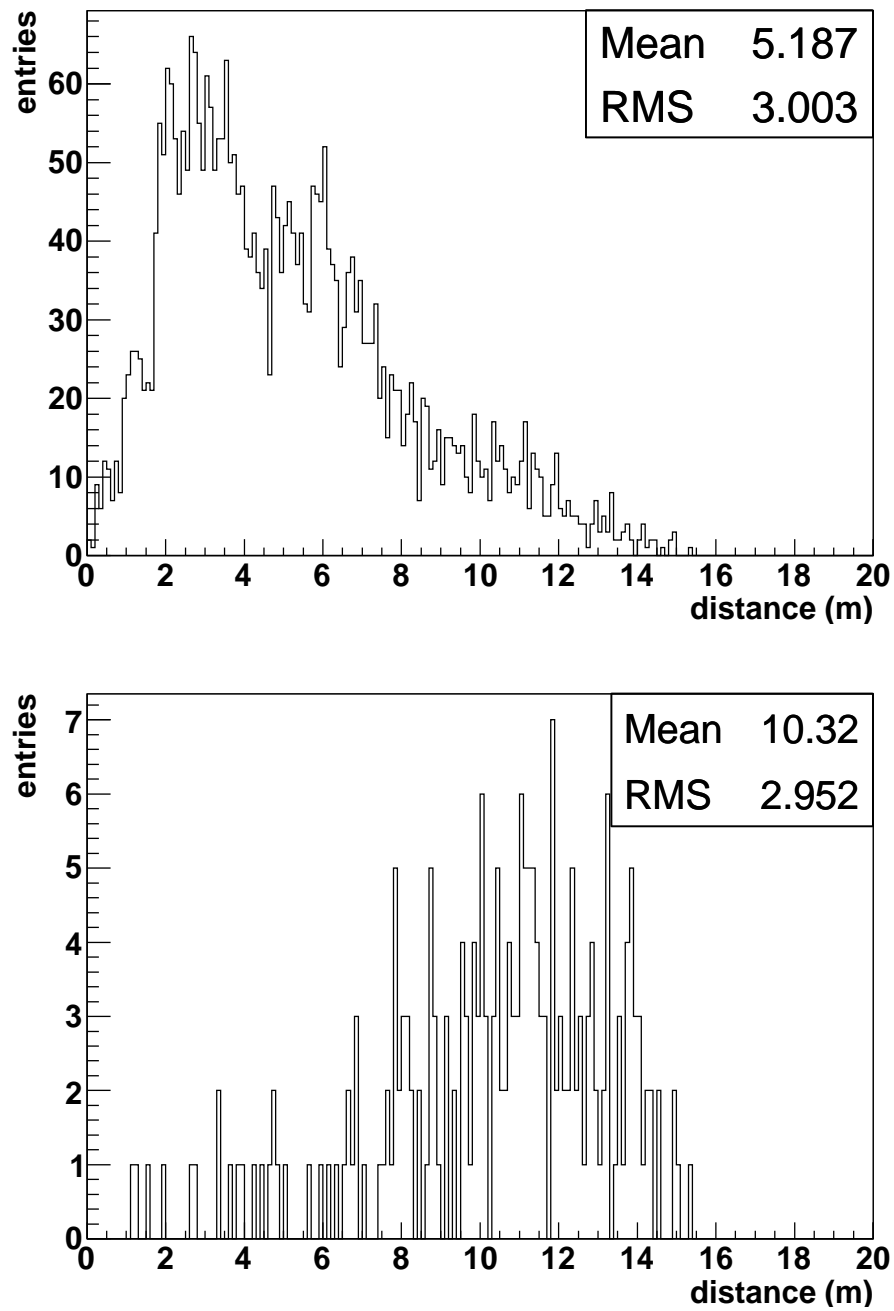


Figure 5.7: Distance, with respect to the center of the LVD-CF, of muons that originate at least one neutron that reaches the LVD-CF when the parent μ is tagged (top) or untagged (bottom).

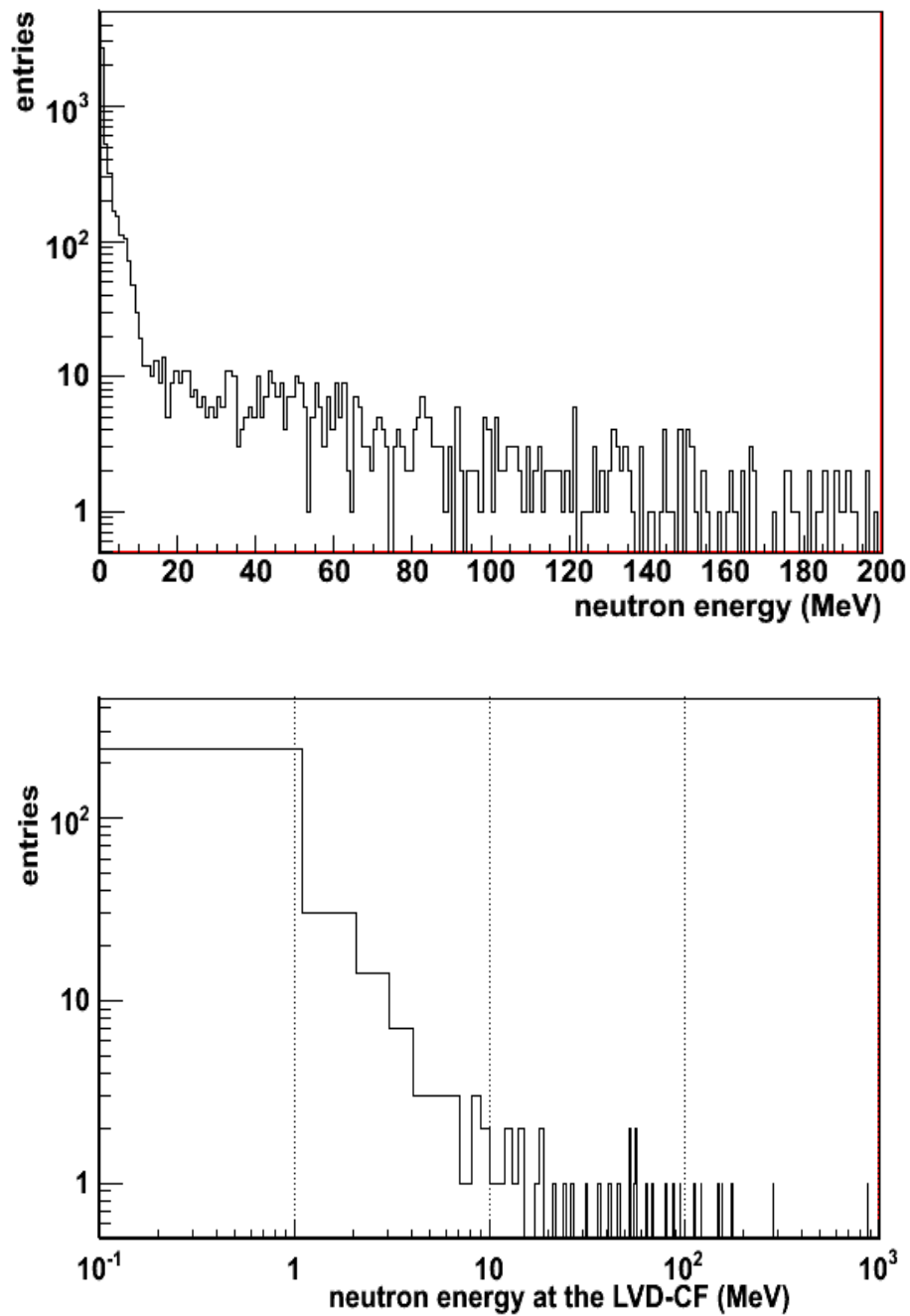


Figure 5.8: *Energy spectrum of the tagged (top) and untagged (bottom) neutrons which enter the LVD-CF.*

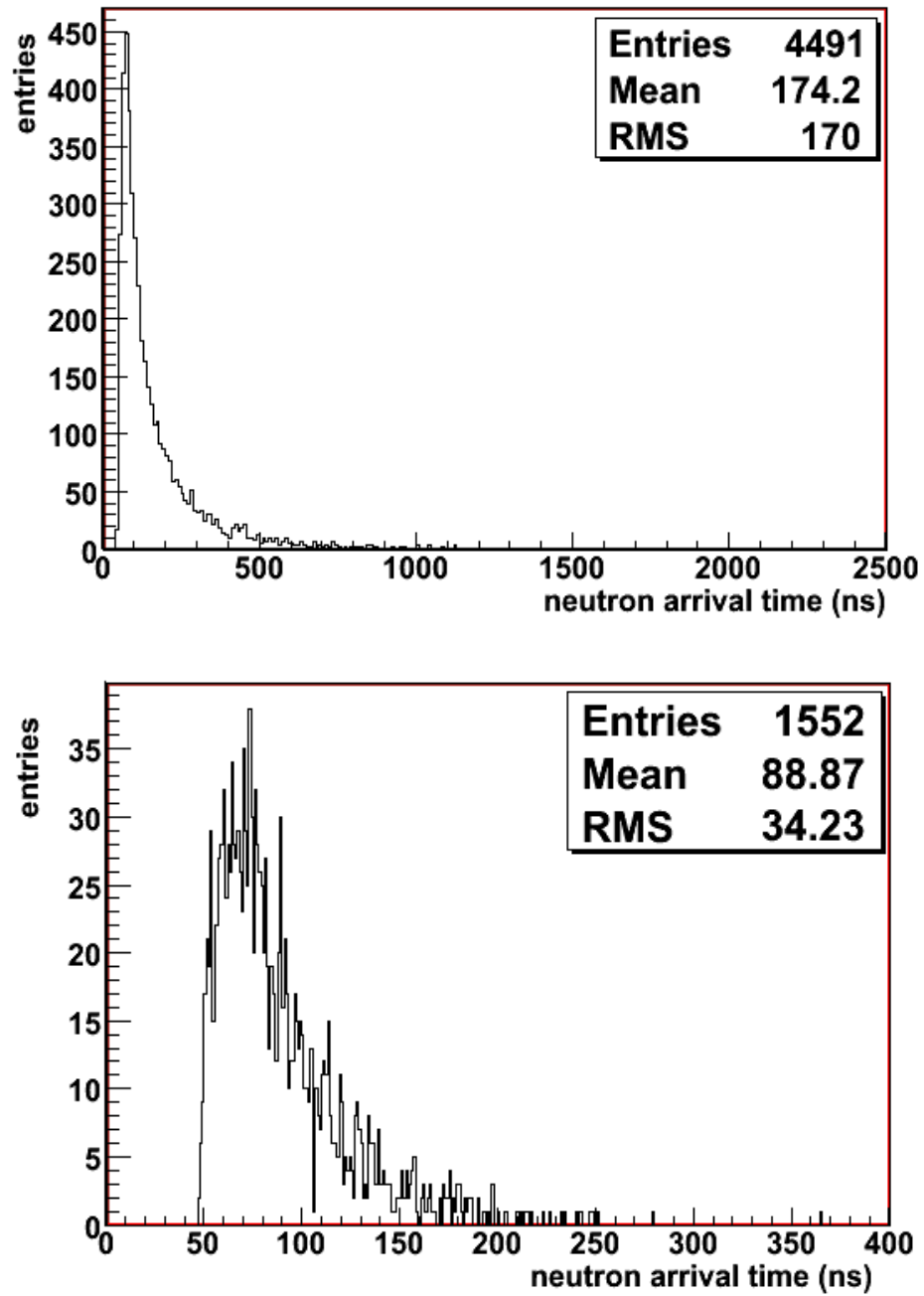


Figure 5.9: Delay between the neutron arrival time and the parent muon for $E_n > 1 \text{ MeV}$ (top) and $E_n > 100 \text{ MeV}$ (bottom).

Chapter 6

The muon-induced neutron yield measurements

The main purpose of this thesis is the measurement of the muon-induced neutron yield at the underground laboratory of Gran Sasso with the LVD experiment. A full Monte Carlo description is hardly needed in order to evaluating efficiencies and to interpret the experimental data. The simulation code LVDG4 and its output will be discussed in section 6.1 while in section 6.2 the analysis procedure will be presented with a particular attention to the parameters which are needed to be estimated and fixed by the simulation. Finally, in section 6.3, the measurement of the neutron yield in iron and liquid scintillator will be shown and, where possible, compared with other experimental data.

6.1 LVD simulation description

The LVDG4 code and this analysis, in particular, has been based on the last Geant4 version 9.3. The chosen physics lists is the one called QGSP_BIC_HP: its validation and physics models description have been already discussed in section 3.3. Muons, together with neutrinos, are the most penetrating component of cosmic rays in underground laboratories. Because of their interactions in the rock around the experimental hall and the detector itself, muons can induce neutrons through one of the reactions described in section 1.2.2. For what concerning the geometry,

it has been built taking into account the real dimensions of the experimental hall used for the evaluation of the neutron flux coming from the rock (see section 4.4). In order to have the full developping of the electromagnetic and hadronic showers 6.7 m of rock have been used plus 30 cm of concrete. The detector has been placed close to the end of the hall to take into account possible edge effects. Muons are simulated with energy spectrum and angular distribution at the LNGS and they are sampled in the same way already used in section 4.4 and 5 even if the center of the circle has been chosen in the center of the LVD detector instead of the center of the hall. The radius of the sampling circle has been set to 15.3 m, larger than the maximum dimensions of the detector itself. The number of muons generated is 3×10^7 that considering the muon rate at the underground laboratories of $1.17 \mu/(\text{m}^{-2} \text{ hour})$ corresponds to 3.98 years of detector live time.

6.1.1 Digitization

The LVDG4 code has been built in order to get an output file readable by the ROOT toolkit with two *trees* inside. In the first one all the physical information about neutron and muon interactions are saved, while in the second one the energy deposition in each counter, with its ID name and time information are recorded. The energies released in a counter have been grouped in time bin of 12.5 ns and the ones falling in the same bin have been summed. In this way it is possible to simulate the TDC response of the detector. The obtained ROOT files are then preprocessed and processed.

In the first step for each counter the pulses recorded are read event by event and for every pulse with a released energy higher than 0.1 MeV the procedure of pulses integration starts. This procedure consists in looking for and summing all the pulses in the first 4 bins with respect to the time of the trigger pulse and in the following 15 bins. In this way it is simulated the charge integration of the ADC over 250 ns (that corresponds to 20 time bins). At the same time the dead time of $1.125 \mu\text{s}$ due to the conversion and data reading in the acquisition is taken into account: all the pulses in this time windows are rejected. Before processing these data, the smearing of all energies using the detector energy resolution given by equation 2.2 is applied.

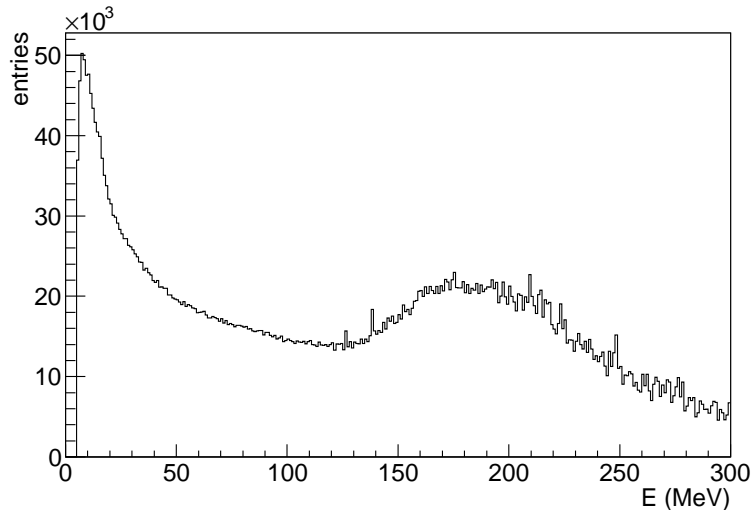


Figure 6.1: *Energy spectrum of the HET signals where it is clearly visible the muon peak at 185 MeV.*

The second step is the data processing where pulses are read and organized in order to get a ROOT file with the same information and format of the detector output data.

6.1.2 Selection cuts

The selection cuts used for the analysis can be arranged into three main categories:

- Muon selection
- Counter selection
- LET signals selection

As seen in chapter 2 the events detected by LVD are divided in two categories: neutrino-like and muon-like. LVD operates with two discrimination energy threshold: the first one set to 5 MeV (HET) and the second one set to 1 MeV (LET). The events that have only one HET signal or more HET signals but not in time coincidence within 250 ns are considered to be neutrino events. On the other side if

there are two or more signals above the HET in time coincidence they are classified as muon events. The BUILDER program correlates in time the part of an event from different towers in order to avoid the wrong reconstruction of a muon event in two neutrino events. The detected muon rate in LVD is about 0.1 Hz, that means more than 8 thousand muon detected per day and so the 4 years statistic taken into account for this analysis is very high. For this reason two stronger condition have been requested to define a muon event by software. In order to clean the muon sample and avoid events built like muon event but induced by background, the first selection cut consists in requesting at least two pulses in time coincidence with a detected energy higher than 10 MeV for each pulses. This sub-sample of muons are called μ -**def**. All the signals above the high energy threshold in time coincidence with the muon (within 250 ns) are defined as μ -**pulses** and all the counters with a μ -pulse are called **crossed**. With the second muon cut it is selected a sub-sample of the last selected muons. The request is that at least one crossed counter must be internal. Muons that satisfy both conditions are called μ -**good** and represent the sample on which the analysis is based on. In figure 6.1 is showed the energy spectrum of the HET signals in the detector for muon events. Most of the muons at the underground laboratory are particles at minimum of ionization and the mean path length in each counters is about 70 cm that means a mean energy deposited by muons per counter of about 185 MeV. This characteristic is well highlighted by a Gaussian peak in the energy spectrum of HET signals.

In figure 6.2 we show a section of the LVD detector with the inner tank coloured in blue and outer ones in white. For this analysis only the inner tanks (lower background level) have been taken into account. Moreover, the counters must have a flat time distribution of LET signals in neutrino-like events. Then an additional cut has been applied removing all counters with TDC problems, ADC problems or missing calibration. After these selections the remaining inner counters are 253 with respect to the 400 total internal counters.

As seen in section 2.2, LVD operates with two discrimination energy threshold and in particular neutrons are detected observing the low energy gamma signal (2.23 MeV) due to neutron capture on a proton of the liquid scintillator. Neutrons can be also captured by iron in the LVD structure with the emission of few gammas with a total emitted energy of about 7 MeV, but this case represent only the 10%

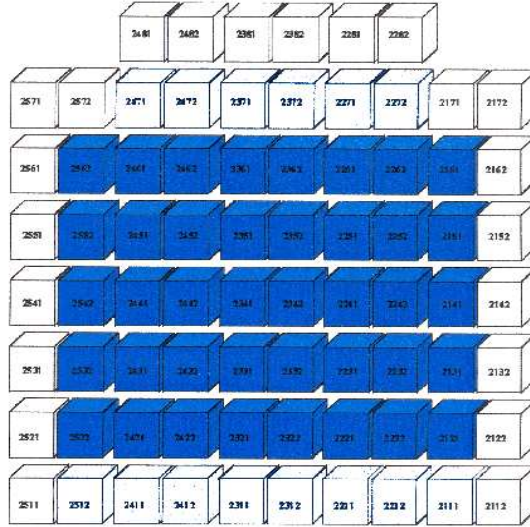


Figure 6.2: *Schematic view of the transverse section of the detector with external tank in white and the inner counters in blue.*

of all the neutron captured while the 90% are captured by a proton. The first request applied to the LET signals is on their energy: only signals with energy lower than 5 MeV have been taken into account. As explained in 6.2.1 the number of neutrons is obtained by fitting the time distribution of the LET signals with respect to the muon crossing time with a function that has a flat component due to background and an exponential part due to neutrons with a characteristic slope ($\sim 150 \mu\text{s}$). This distribution is fitted in a time window ranging between 50 and 400 μs in order to avoid after-pulses (short time region) and differences in the gate width (long time region). To carry out the total number of neutrons detected it is important to evaluate the background level and the slope of the exponential due

to neutrons. The MC simulation find out a value for the exponential slope that is in disagreement with respect to the value measured in LVD in counters crossed by muons, while there is a good agreement between MC and data for those counter outside the muon track: the analysis has been performed only for counters *not crossed*. The effect that cause this discrepancy has been investigated and it will be explained in section 6.2.2.

6.2 Background, capture time and efficiencies estimation

6.2.1 Description of the analysis procedure

Most of the neutrons produced in the LVD detector are mainly captured on hydrogen ($\sim 90\%$) and they can be identified by the characteristic capture γ rays of 2.23 MeV. Figure 6.3 shows the expected Δt distribution of LET signals after the muon crossing. The number of detected neutrons is calculated by fitting the time delay distribution with the following function:

$$\frac{dN}{dt} = A \times e^{\frac{-t}{\tau}} + B \quad (6.1)$$

where A is the multiplicative constant of the exponential, τ is the mean neutron capture time and B is the background level. In this figure it has been highlighted the time window used for fitting the distribution and the two components of the function: a flat component due to background not correlated with the crossing muon and an exponential component due to neutrons where the exponential slope is the mean neutron capture time. The number of neutrons in the time window $50 \div 400\mu s$ is estimated by the following:

$$N_{fit,t_1 \div t_2} = \frac{A \times \tau}{\delta t} (e^{\frac{-t_1}{\tau}} - e^{\frac{-t_2}{\tau}}) \quad (6.2)$$

while the total number of neutrons is given by:

$$N_{fit} = \frac{A \times \tau}{\delta t} \quad (6.3)$$

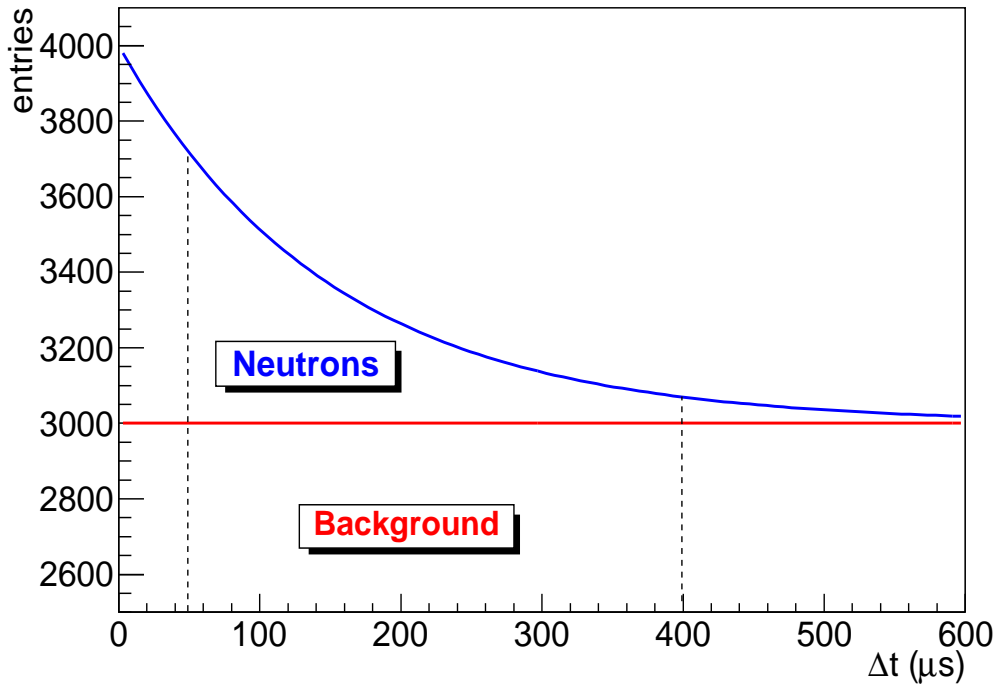


Figure 6.3: *Example of the expected time distribution of LET signals with respect to the muon crossing time. In blue the exponential component of the distribution due to neutron is highlighted while in red is represented the flat component of the background.*

where δt is the bin width adopted in the distribution (in our case it is $1 \mu\text{s}$). The parameters A and B are free, but the mean capture time is constrained by the Monte Carlo simulation. This solution has been applied to reduce the number of parameters of the fit and this choice is supported by the fact that the developed MC reproduces with a good agreement the τ value measured with a ^{252}Cf source (see section 4.3) in different configurations. The background, both in HET and LET signals, is due to natural radioactivity but, especially for LET signals, it can be also due to electronic noise. Anyway for these kind of events, the background is assumed to be approximately constant in the region of interest and this statement will be proved by a specific analysis described in section 6.2.3.

The actual number of neutrons produced by muons in iron or in liquid scintilla-

tor is related to the fit result N_{fit} by multiplying the fraction of induced neutrons in the considered material:

$$N_i = N_{fit} \times f_i \quad (6.4)$$

where i refers to iron or liquid scintillator and f_i is the fraction of detected neutrons that were produced in the i -th material. Using the last equation it is possible to extract the neutron yield with the following equation:

$$Y_i = \frac{N_i}{N_\mu L_{\mu,i} \rho_i S_m \varepsilon_i} \quad (6.5)$$

where N_μ is the number of muons after the application of the selection cuts, $L_{\mu,i}$ is the mean muon track length in each material, evaluated by the Monte Carlo simulation, ρ_i is the density of the i -th material, S_m is a scaling factor that take into account the number of internal active counters and $\varepsilon_{n,i}$ is the detection efficiency.

The data sample analysed spans 4 years, between 2005 and 2008, after the energy recalibration of the whole detector made in 2004. Muon events have been selected in the way already explained in section 6.1.2 and the number of muons is 77 M with a mean number of internal active mass of 304 tons, corresponding to about 253 counters.

6.2.2 Mean neutron capture time: MC estimation

As seen in the last section the parameter τ describes the slope of the exponential component of the LET time delay distribution and it is directly correlated to the total number of neutron detected. In section 4.3 it has been showed that the τ values got by the MC simulation are in agreement with values measured with a ^{252}Cf source in different configuration (at the center of the counter and beside the portatank). In figures 6.4 are plotted the time delay distribution obtained by the simulation (*top*) and by experimental data (*bottom*) for the counters not crossed by muons. The fit applied to both distribution has the three parameters free and they are in agreement for this sample of counters. The same has been done for the counters crossed by muon (see figures 6.5) but in this case there is an evident disagreement between simulation and data. The value of τ are reported in table 6.1.

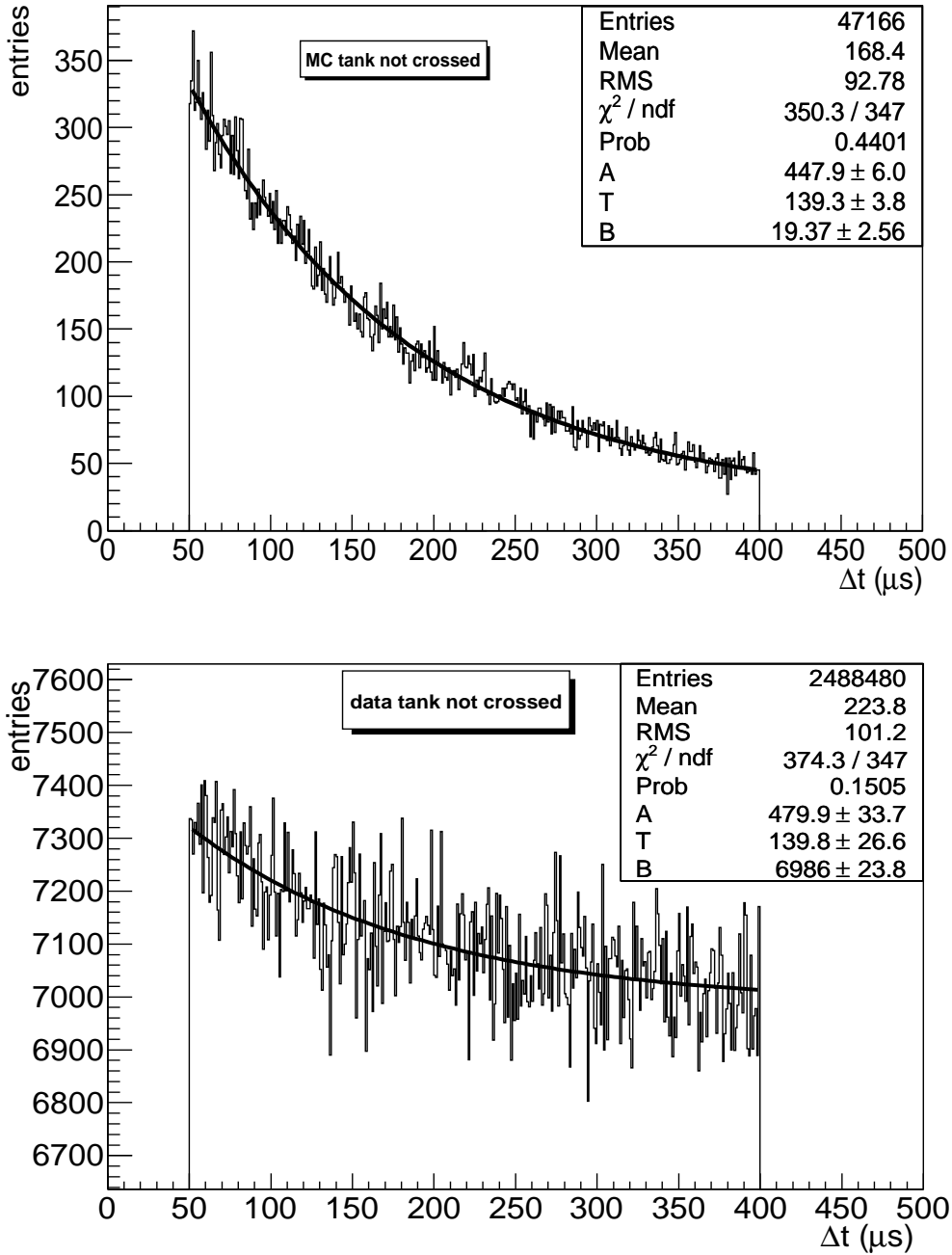


Figure 6.4: Time delay distribution of the LET signals in counters not crossed by muons obtained by MC (top) and data (bottom). The fit function has three free parameters.

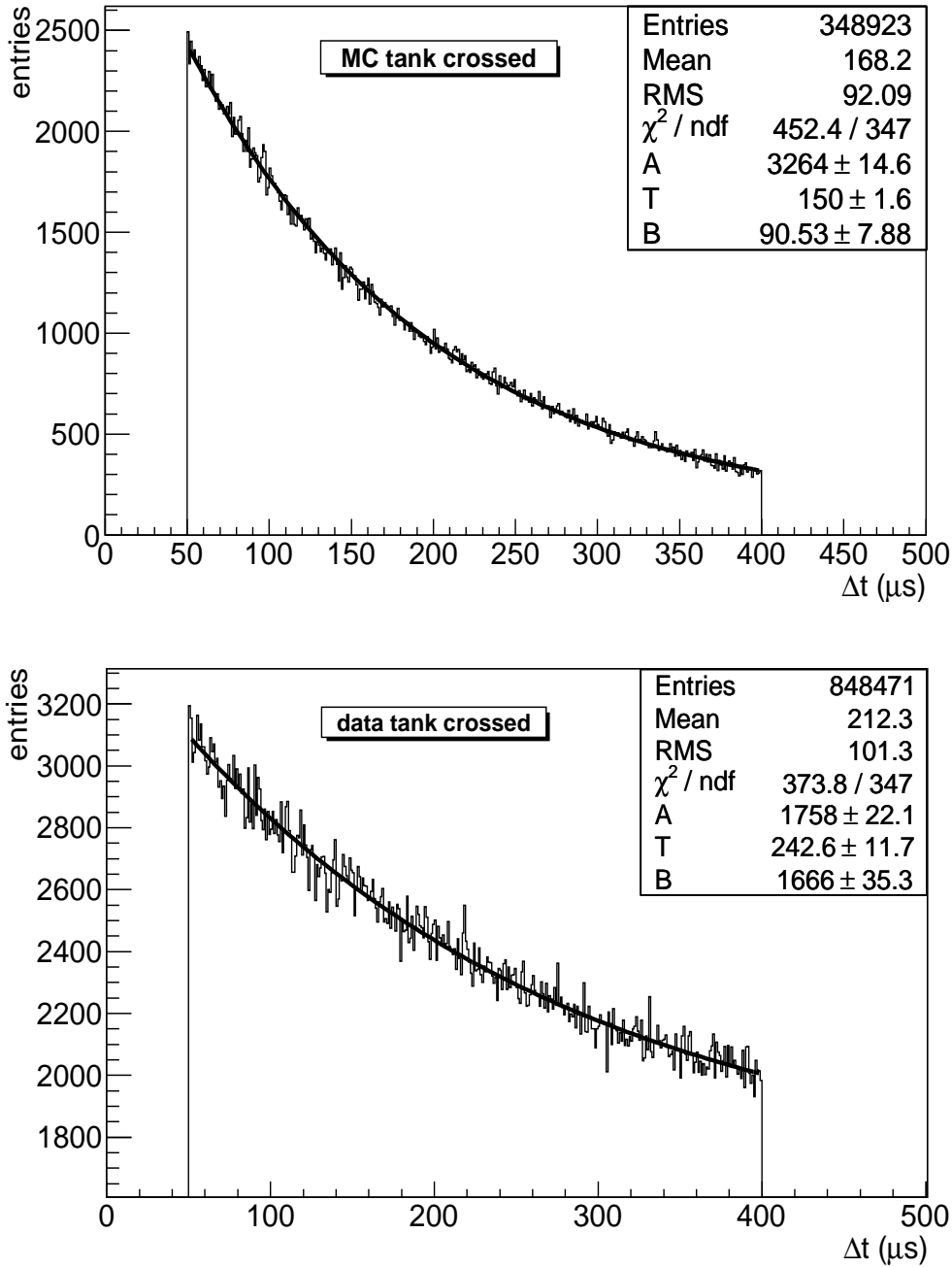


Figure 6.5: Time delay distribution of the LET signals in counters crossed by muons obtained by MC (top) and data (bottom). The fit function has three free parameters.

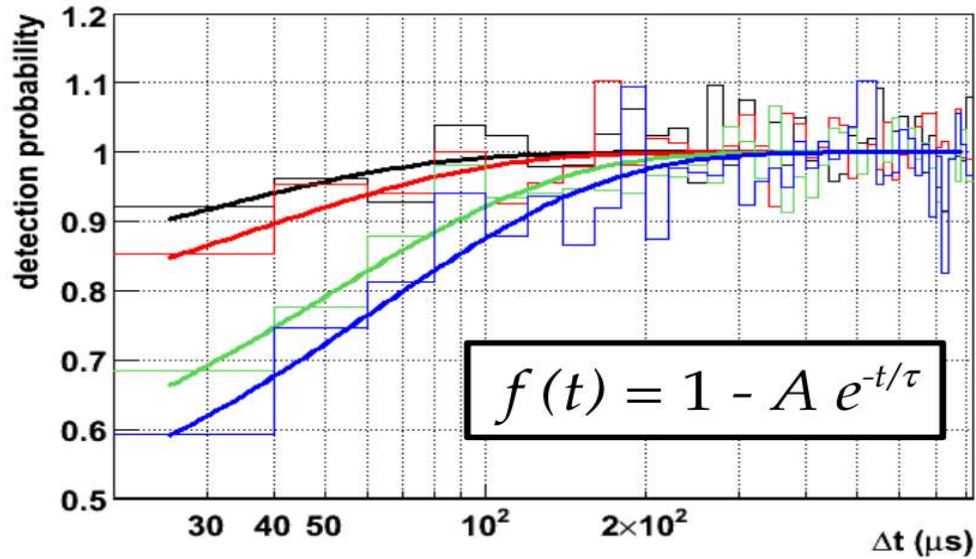


Figure 6.6: *Distribution of the time difference between any LET pulses occurring in 0.8 ms after the trigger and the trigger itself, for different energy of the HET pulse: 40 MeV (black), 80 MeV (red), 160 MeV (green) and 230 MeV (blue).*

The disagreement found in counters crossed by muons can not be imputable to the simulation because it is able to reproduce all the other measurement of τ . Moreover the experimental neutron capture time in counters crossed by muons, with a HET pulse lower than 50 MeV, is in agreement with the Monte Carlo estimation. The discrepancy seems to be related to some kind of electronic distortion due to the great muon energy releases in the counter. To explain this effect and try to sort it out a test on the detector has been studied. It is possible to emulate the huge amount of light produced by the muon with a flashing LED positioned inside a chosen counter and studying the background level in the same counter. The LET signals following the trigger given by the LED should give a flat dis-

τ	MC	data
tank not crossed	139.3 ± 3.8	139.8 ± 26.6
tank crossed	150.0 ± 1.6	242.6 ± 11.7

Table 6.1: *Summary table of the τ value in μ s obtained by MC and data for both tank samples.*

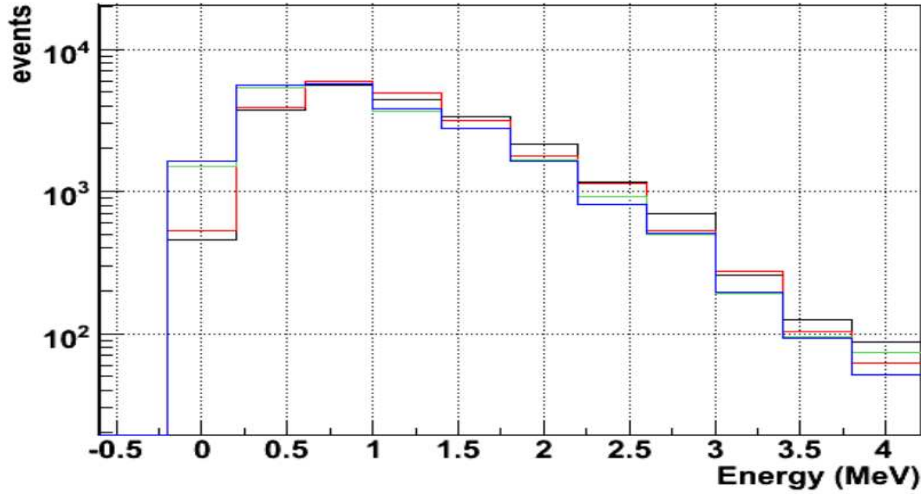


Figure 6.7: *Energy spectrum of LET signals for different energy of the HET pulse: 40 MeV (black), 80 MeV (red), 160 MeV (green) and 230 MeV (blue).*

tribution because they are uncorrelated in time and energy from the LED pulse itself, unless an electronic effect occurs. In figure 6.6 are showed the results of the test. They represent the time delay distribution of LET signals after the LED trigger and they are normalized to their asymptotic value so they can be regarded as probability distributions. All the distributions exhibit the following exponential behaviour:

$$f(t) = 1 - A e^{\frac{-t}{\tau_\mu}} \quad (6.6)$$

with the amplitude A and the slope τ_μ increasing with the energy of the trigger. An anti-correlation has been found between the energy of the trigger pulse and the energy of the pulses in the LT gate, that produce a weak distortion of the spectral shape, showed in figure 6.6. Until now there is no evidence of dependence of the fit parameters among different counters. This anomalous behaviour can be explained considering a derivative circuit somewhere between the PMTs and the discriminator. As showed in figure 6.8 a small pulse occurring after a big one could remain under threshold if the capacitor of the derivative filter is not yet completely discharged. The dividers of the PMTs FEU49b and FEU125 (used in LVD) have a capacitor of nominal value equal to $0.1\mu\text{F} \pm 10\%$ (measured value between 0.1

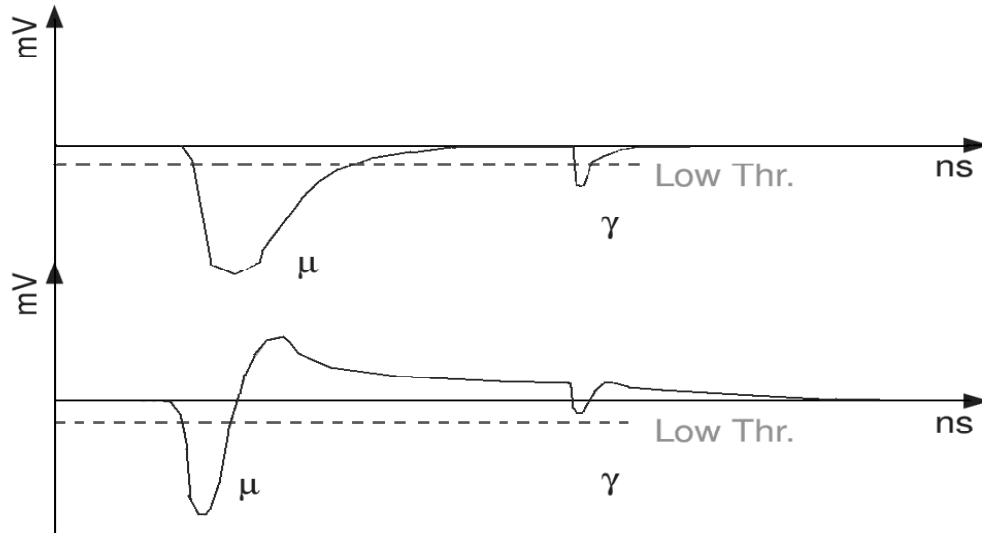


Figure 6.8: *Schematic view of the effect induced by the capacitor: after a high pulse the baseline is higher than the ground level due to the charge still present in the capacitor.*

and $0.8 \mu\text{F}$) connected in series to the anode, which lead to a time constant of $5 \div 40 \mu\text{s}$. This explanation has been confirmed performing another test using a pulse generator which feeds the module C175 (discriminator) through a $0.5 \mu\text{F}$ capacitor. It has been observed that immediately after the trigger there is a blind zone where the generated signals do not exceed the low energy threshold.

Once clarified the origin of this effect related to a high energy pulse in the counter, it has been tried to fit the time delay distribution for the counters crossed by muons in a smaller window that ranges between 200 and $400 \mu\text{s}$. In figure 6.9 is showed how change the fit when only time larger than $200 \mu\text{s}$ are fitted (black line) and in particular it is clearly visible the lack of events in the region of short time and this is in agreement with the mentioned effect. Because of the PMTs saturation it has not been possible to study this effect for released energy higher than 300 MeV and the MC simulation shows that muons can lose energy up to 2 GeV in a single counter.

Although the effect has been well understood in this work, the analysis has been limited to the counters not crossed by muons.

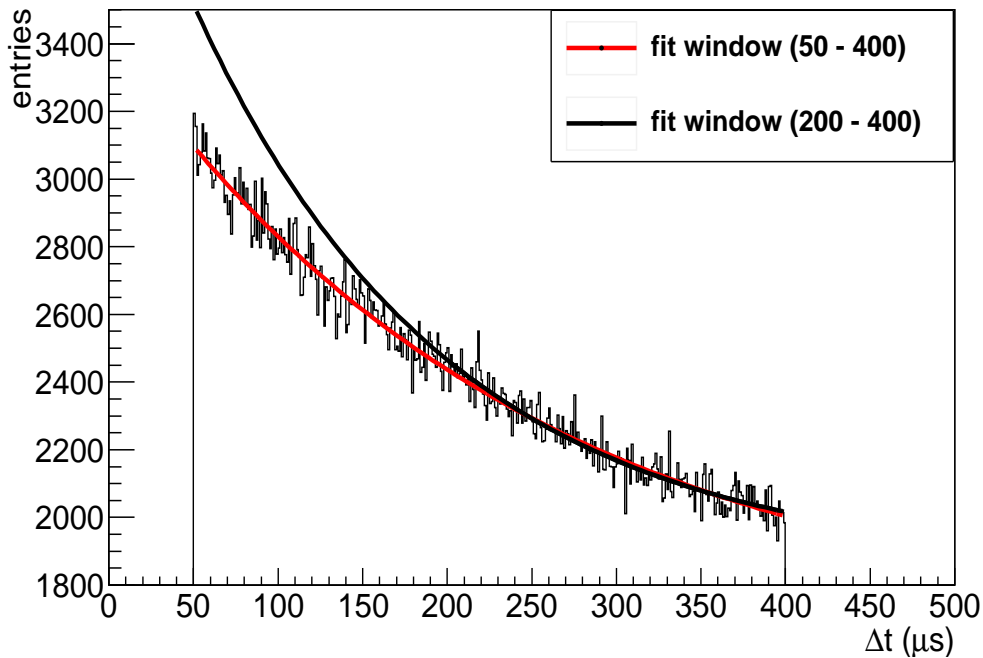


Figure 6.9: *Time delay distribution of the LET signals in counters crossed by muons obtained by data and fitted by a function with three free parameters in different range: $50 \div 400 \mu s$ (red line) and $200 \div 400 \mu s$ (black line).*

6.2.3 Background evaluation

In order to estimate the value of the background expected in the time delay distribution, it has been necessary to select events neutrino-like that consist in a single HET signal or more HET signals not in time coincidence. The reason for using the neutrino-like events is due to the presence of muon-induced neutrons in the muon-like sample which does not allow to measure the flat component of the background. For the neutrino-like events, the LET signal rate of each counters in the time window $50 \div 400 \mu s$ has been measured. The measurement has been performed grouping the counters in two samples: those which have an HET signal and those without an HET signal. In this way it is possible to estimate the background level for counters crossed by muon and not crossed, respectively.

The background evaluation has been performed for each counter and for each

year in the time period under investigation because in this way it is possible to get a time delay distribution of LET signals flat and not affected by residual neutrons induced by muons not detected. Once the background rate is known for each counter, it is possible to evaluate the total number of background events expected in the time window for the whole analyzed sample by the following:

$$B_{exp} = T \sum_i R_i N_i \quad (6.7)$$

where T is the time window width ($50 \div 400 \mu s$), R_i is the background rate per μs for the counter i and N_i is the number of times the counter has been opened for looking at LET signals after the μ . If the time distribution is got by summing the time of the LET signals for all the counters and for the whole 4 years, it can see the exponential behaviour due to neutrons, but their rate is more than one order of magnitude lower than the neutron flux produced by detected muons and so it can be neglected. In figure 6.10 is plotted the energy spectrum of the HET signals in neutrino-like events. The peak at 185 MeV is still visible but it is about 5 order of magnitude lower than the low-energy peak and it should be compared with figure 6.1 where the ratio of the two peaks is a factor 2.

The parameter B expected for the counters crossed by muon is:

$$B_{exp,c} = (1910 \pm 70) \text{ background events } / \mu s \quad (6.8)$$

while in the counters in absence of a HET signal, the background level expected is:

$$B_{exp,nc} = (6988 \pm 35) \text{ background events } / \mu s \quad (6.9)$$

These value should be comparable with the ones obtained by fitting the time delay distribution in counters crossed and not crossed in muon-like events but there is an agreement only for the not crossed tank sample. In order to show that the disagreement in tank with a HET signals is due, once again, to the same electronic effect that afflicts the τ , we have also evaluated the expected background in counter crossed by muons when the released energy is below 50 MeV. In this case there is agreement between the expected and the measured background level. In table 6.2 the background levels are summarized.

	fit	measured
tank not crossed	6986 ± 24	6988 ± 35
tank crossed	1698 ± 30	1910 ± 70
tank crossed ($E_H < 50\text{MeV}$)	446 ± 15	439 ± 7

Table 6.2: Summary table of the background value given as number of background events per μs obtained by fitting the data and by an independent way.

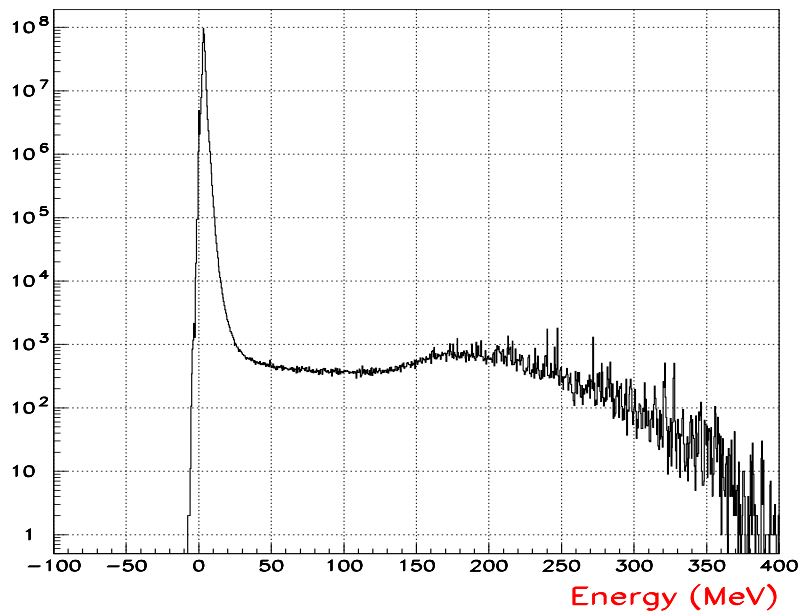


Figure 6.10: Energy spectrum of HET signals in neutrino-like events.

6.2.4 Low energy threshold

The detector response has been simulated selecting all the energy deposits higher than 100 keV in each counter. The signals are then smeared accordingly to the energy resolution of the detector. The effects of the smearing are shown in figure 6.11, where the released energy associated to LET signals with and without smearing are plotted. It is clearly visible the peak at 2.23 MeV, while the peak at low energies is mainly due to neutron capture on iron. The neutron binding energy on ^{54}Fe is about 7.45 MeV and this energy is released through several gammas. However, in some cases the whole binding energy can be detected in a

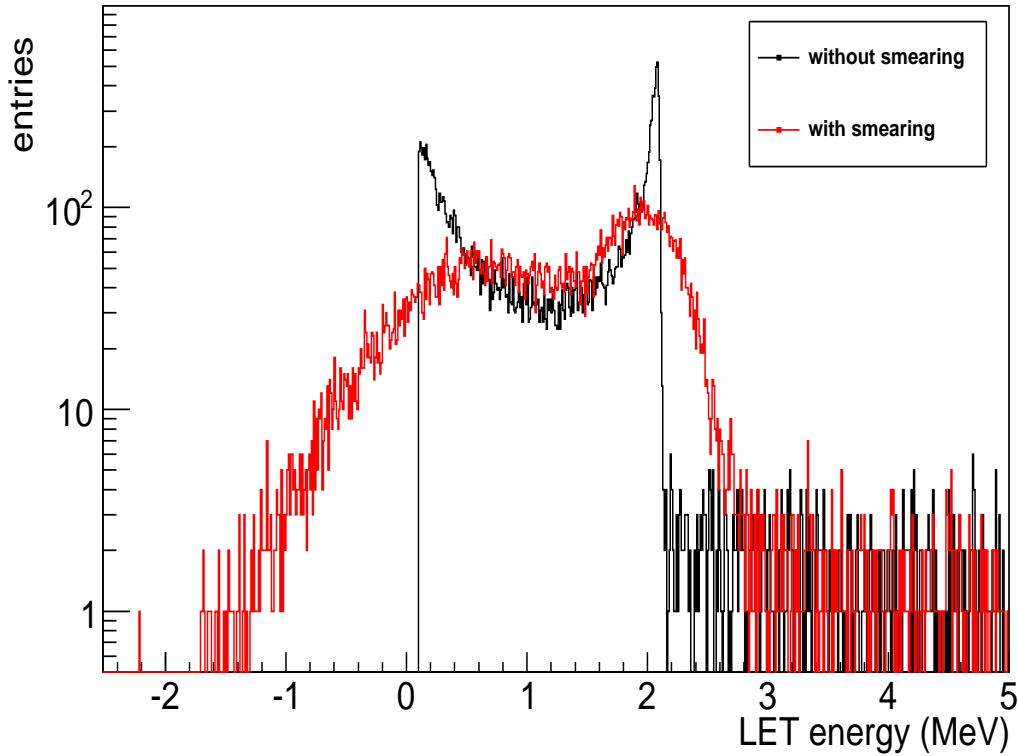


Figure 6.11: *Simulated energy spectrum of LET signals with (red line) and without (black line) smearing.*

single counter giving the few events above 2.23 MeV visible in the spectrum. The same argumentation can be applied to neutron capture on ^{12}C , that has a binding energy of 4.95 MeV.

The experimental low energy threshold is set to 500 keV and it is described by a step function, shown in figure 6.12. The function does not present a sharp edge at the set point because of the energy resolution. Moreover the internal counters are 400 and each of them can have small differences in the threshold level. For this reason it is necessary to fix a software energy threshold in both MC and data. With the MC simulation the integral number of neutrons detected has been evaluated for different energy thresholds for both MC and data, as shown in figures 6.13. Every point in the graphs represents the number of neutrons, obtained by fitting (with

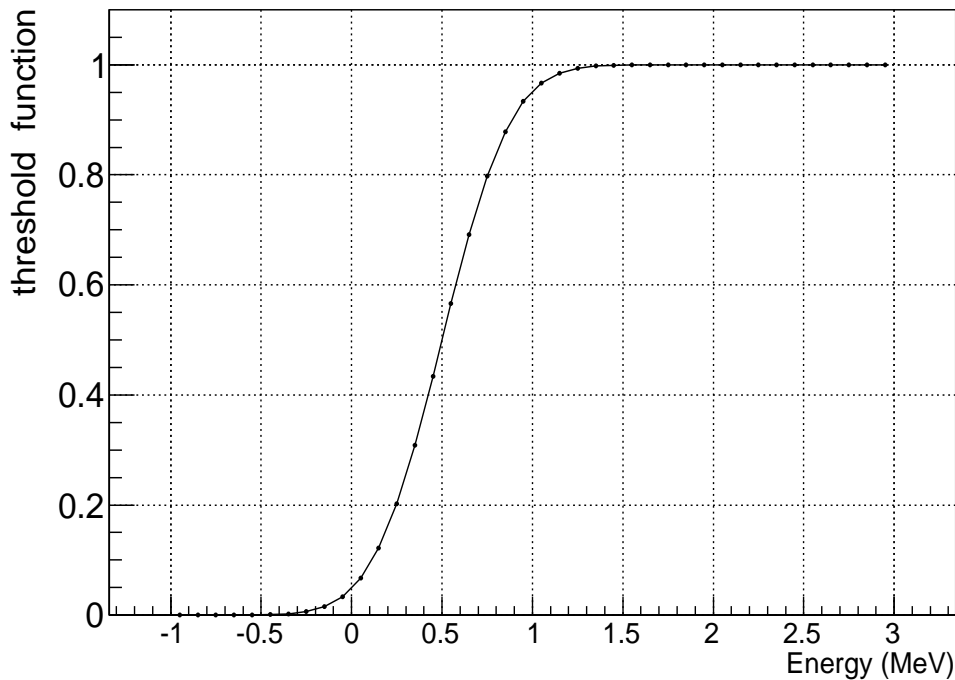


Figure 6.12: *Shape of the threshold function with a nominal value of 500 keV in LVD.*

the parameters A and B free and τ fixed by MC) the time distribution of LET signals with energy ranging between the software energy threshold and 5 MeV. The first bin of both histograms has been calculated without fixing a lower value for the LET signal energy: all pulses with energy lower than 5 MeV has been taken into account. Both histograms show the same behaviour, but for a better visualization, each bin of the LVD data histogram has been divided by the correspondent value of the same bin obtained with the simulation. The ratio is shown in figure 6.14 in the region $0 \div 2$ MeV. These plots fix an upper limit to the systematic error due to effects of the threshold function to a value of 7%, if the software energy threshold is fixed between 0.2 and 1.8 MeV.

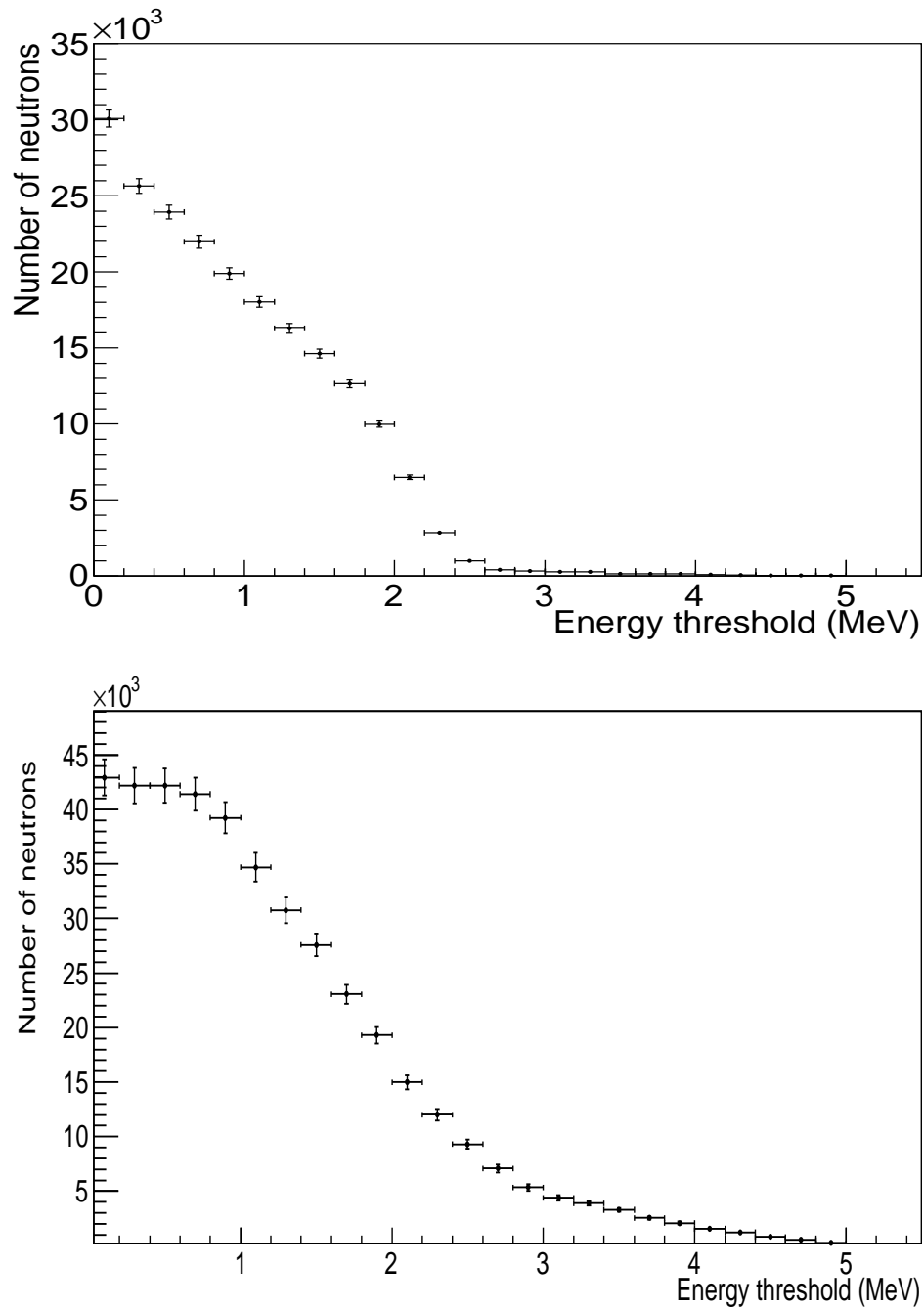


Figure 6.13: Integral distribution of the neutron numbers obtained from the fit of the LET signals time distribution, given as a function of the software energy threshold for MC simulation (top) and DATA (bottom). The bins have a width of 0.2 MeV and the threshold value is the lower edge of each bin. For the first bin no software energy threshold has been considered.

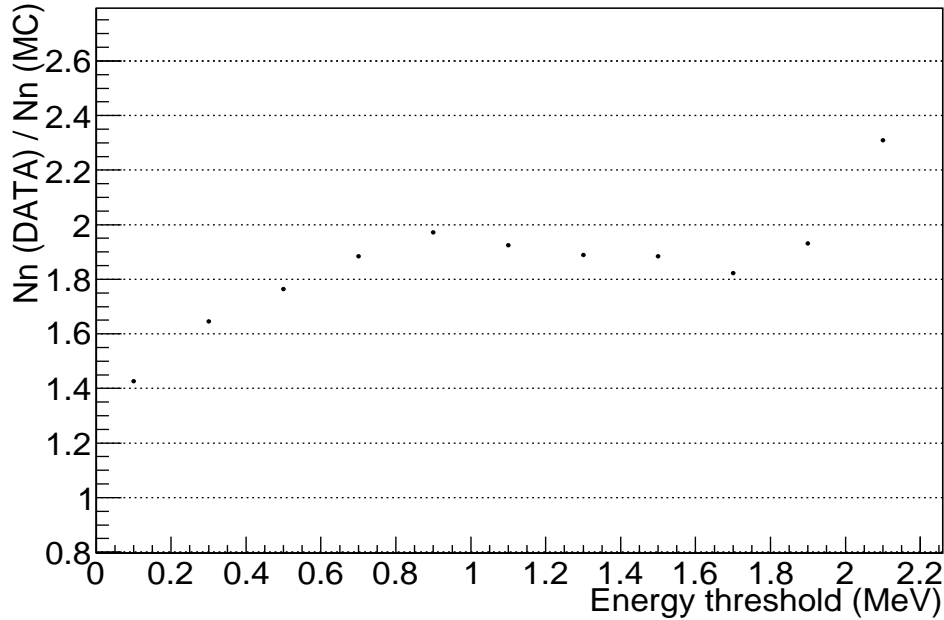


Figure 6.14: *Distribution of the ratio between the neutron number from DATA and MC as a function of the software energy threshold in the region 0÷2 MeV.*

6.2.5 Efficiency evaluation

In order to find the neutron yield in iron or in liquid scintillator for a given value of total neutrons detected by LVD the efficiency has to be evaluated from the MC simulation. The muon selection cuts does not affect the efficiency because they clean only the muon sample. The total efficiency of the analysis depends by the tank selection, the LET selections and intrinsic efficiencies. It can be written as:

$$\varepsilon = \varepsilon_w \times \varepsilon_{tr} \times \varepsilon_{tank} \times \varepsilon_{thr} \times f_n \quad (6.10)$$

where ε_w is the fraction of neutrons that fall in the time window 50÷400 μs with respect to the total neutron detected, ε_{tr} is the efficiency of the trigger logic, ε_{tank} is due to the selection of internal counters not crossed by muons, ε_{thr} is related to the software energy threshold for the LET signals and f_n is the fraction of muon-induced neutrons that escape the detector without being captured.

material	neutrons produced	neutrons detected	ε (%)
IRON	2252829	24301	1.07
LS	460152	3457	0.75

Table 6.3: *Number of neutrons produced and detected for the sampled muons. In the last column the overall efficiency are shown.*

With the MC simulation the overall efficiency can be evaluated dividing the number of LET signals related to a captured neutron and the total number of neutrons produced in the i -th material. The latter is shown in table 6.3 for the muon sample after the application of the selection cuts.

The factor S_m in equation 6.5 takes into account the mean active mass calculated for each run. Over the years LVD have been running under different configuration of active counters because of ordinary maintenance of the detector. This factor is evaluated as the ratio between the mean number of active counters in LVD, 253, and the total internal counters, 400.

6.2.6 Number of neutrons

The number of neutrons in the time window $50\div 400 \mu s$ detected by LVD is given by fitting the time delay distribution of LET signals with the equation 6.1 where the parameters τ is fixed by the MC simulation. The value of the multiplicative constant A and the background level B, as can be seen in figure 6.15, are 388.1 ± 20.1 and 4235 ± 6.2 respectively. Using the equation 6.2, it gives:

$$N_{fit}(LVD) = 34700 \pm 3\% \pm 3.2\% n$$

where the the first error is systematic σ_{sys} , and the second is the statistical one (σ_{stat}). The systematic error has been evaluated taking into account the maximum spread among the number of neutrons obtained by fitting the time distribution with three, two or only one free parameter. The statistical one comes from the propagation of the error on the fit parameters.

Fitting the time distribution of the simulated LET signals, shown in figure 6.4 (*top*), we see that there is a flat component, even if we know that all the entries in the histogram are genuine neutrons. The number of neutrons given by the fit is

material	neutron number	fraction (%)
IRON	24301	85.56
LS	3457	12.16
ROCK	547	1.93
OTHERS	100	0.35

Table 6.4: *Number and fraction of neutrons that give a LET signal obtained by MC simulation.*

85% of the real number of neutrons. For this reason the value $N_{fit}(LVD)$ has to be scaled by the factor $s = 0.85$, that leads to:

$$N_{fit}(LVD) = 40800 \pm 1600 n \quad (6.11)$$

From the MC simulation it is possible to establish how many LET signals correspond to a neutron capture in any material of the detector or in the rock/concrete. In the simulated time distribution, shown in figure 6.4, only 0.32% of the LET signals are not associated to a neutron capture, while for the remaining LET signals the production material has been tracked down. The results are summarized in table 6.4 where: ROCK collects neutrons produced in rock and concrete, IRON collects neutrons produced in the iron of the structure, portatanks and counters, LS collects only neutrons induced in the liquid scintillator and OTHERS collects neutrons produced in mylar, plexiglas, argon and air. This table highlights iron and liquid scintillator as the materials that produced almost all the detected neutrons. For this reason the analysis has been focused on these two materials and applying the fraction presented in the table, we find:

$$\begin{aligned} N_{n,Fe}(LVD) &= 34900 n \\ N_{n,LS}(LVD) &= 5000 n \end{aligned} \quad (6.12)$$

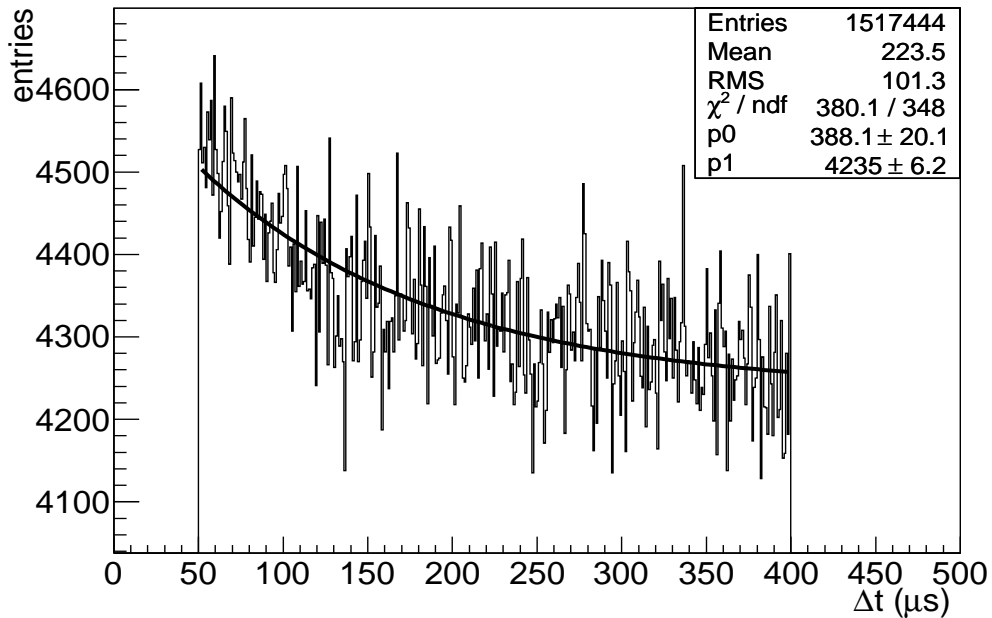


Figure 6.15: Time delay distribution of the LET signals with a software energy threshold of 1 MeV, in counters not crossed by muons obtained by LVD data. The fit function has two free parameters.

6.3 The neutron yield measurement

6.3.1 LVD neutron yield

The last parameter that has to be estimated by the simulation is the average muon path length in each crossed material. Its evaluation has been performed summing all the step length of muons that get through the selection cuts. Then these lengths are divided by the number of selected muons and they are provided as mass thickness using the density of the material. The muon mean path length in iron is 314 g/cm^2 while for the liquid scintillator it is 340 g/cm^2 . Thus, using the following equation:

$$Y_i = \frac{N_i}{N_\mu L_{\mu,i} \varepsilon_i S_m} \quad (6.13)$$

where $L_{\mu,i}$ is given in mass thickness unit (g/cm^2) and $N_\mu = 7707320$ is the number of muons analysed, the neutron yield measured by LVD in iron and liquid scintillator is:

$$Y_{Fe,LVD}(data) = (2.1 \pm 0.1) \times 10^{-3} \text{ n/g/cm}^2 \quad (6.14)$$

$$Y_{Ls,LVD}(data) = (4.0 \pm 0.2) \times 10^{-4} \text{ n/g/cm}^2 \quad (6.15)$$

6.3.2 The iron and liquid scintillator neutron yield

The neutron yield in iron and liquid scintillator can also be estimated by MC simulation taking into account the over mentioned mean path length and total number of induced neutrons, for the same μ -good muon sample. The values found are:

$$Y_{Fe,LVD}(MC) = 1.29 \times 10^{-3} \text{ n/g/cm}^2 \quad (6.16)$$

$$Y_{Ls,LVD}(MC) = 2.44 \times 10^{-4} \text{ n/g/cm}^2 \quad (6.17)$$

These neutron yields differ from the values found in section 4.2 where neutron production has been evaluated for a homogeneous block of material:

$$Y_{Fe}(MC) = 1.19 \times 10^{-3} \text{ n/g/cm}^2 \quad (6.18)$$

$$Y_{Ls}(MC) = 1.95 \times 10^{-4} \text{ n/g/cm}^2 \quad (6.19)$$

The comparison shows an enhancement of the neutron yields for both material: 8% for the iron and 20% for the liquid scintillator. This growth is due to the fact that LVD is not a homogeneous detector but it is made of iron and liquid scintillator interleaved together. More in detail, iron is a high-A material and, according to equation 4.3, it produces a large number of neutrons. Then these neutrons can go through the liquid scintillator and induce secondary neutrons increasing the neutron yield.

This effect shows that the measurements of neutron yields in LVD have to be scaled by the over mentioned factors S_{pure} . Finally, applying this scaling, the

neutron yields measured by LVD for pure materials are:

$$Y_{Fe} = (1.9 \pm 0.1) \times 10^{-3} \text{ n/g/cm}^2 \quad (6.20)$$

$$Y_{Ls} = (3.2 \pm 0.2) \times 10^{-4} \text{ n/g/cm}^2 \quad (6.21)$$

Neutron yield is dependent on the target material, as can be seen from these results and from the test described in section 4.2. It ranges from a few 10^{-4} neutrons/(g/cm²) for light materials up to a few 10^{-3} neutrons/(g/cm²) for high-A materials. Since the latter materials have higher neutron yield, they behave like a neutron source under muon irradiation. Generally they are used for passive γ -ray shielding but, taking into account the higher neutron yield, it is necessary to include an internal low-A shielding between the external shielding and the sensitive detector. Anyway fast neutrons can reach the detector and so it is crucial the knowledge on this induced background. The neutron yield in iron has been measured for the first time in this work and this value is in agreement with the scaling law for neutron yield as a function of the atomic mass of the target.

Generally, the neutron yield in liquid scintillator is given as a function of the mean muon energy at the underground laboratory and it is in agreement with the general trend of measurements performed by other experiments at different depths. In figure 6.16 the neutron yield in liquid scintillator is plotted as a function of the mean muon energy. The result, obtained with this thesis, is highlighted in red and it is in good agreement with the general trend.

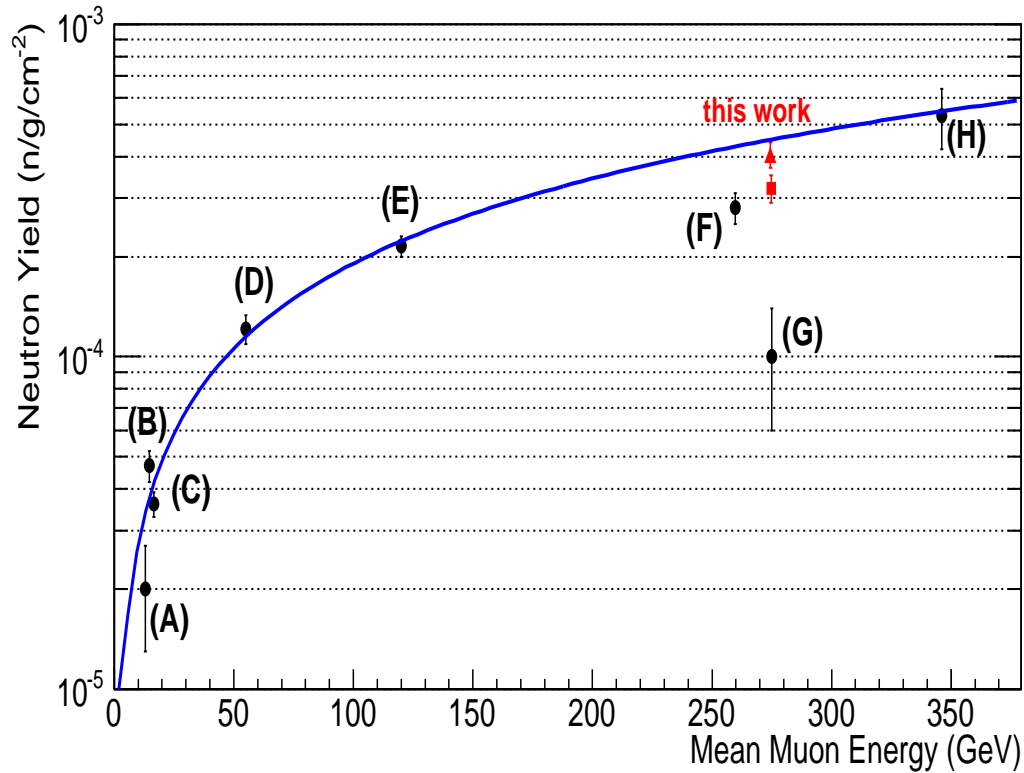


Figure 6.16: Neutron yield in liquid scintillator as a function of muon energy. The red points show the result obtained with this work: (\triangle) neutron yield in LVD detector $Y_{Ls} = (4.0 \pm 0.1) \times 10^{-4} \text{ n/g/cm}^2$ and (\square) neutron yield in pure liquid scintillator $Y_{Ls} = (3.2 \pm 0.2) \times 10^{-4} \text{ n/g/cm}^2$. Other points show the results from experiments at (A) 20 m w.e. [77], (B) 25 m w.e. [70], (C) 32 m w.e. [78], (D) 316 m w.e. [70], (E) 570 m w.e. [79], (F) 2700 m w.e. [82], (G) 3000 m w.e. [80], and (H) 5200 m w.e. [81].

Conclusions

In this thesis we describe in detail the Monte Carlo simulation (LVDG4) built to interpret the experimental data collected by LVD and to measure the muon-induced neutron yield in iron and liquid scintillator.

A full Monte Carlo simulation, based on the Geant4 (version 9.3) toolkit, has been developed and validation tests have been performed. The first test concerned the neutron production in several materials due to muons of 270 GeV. The reasons were to study the differences in three commonly used physics lists. That study led to the choice of the QGSP_BIC_HP physics list. Other tests concerned the measurement of the neutron mean capture time for neutrons emitted by a ^{252}Cf source in two different configurations: in the centre of a counter and beside the lateral panel of a portatank inside the LVD detector. The Monte Carlo simulation reproduces well both measurements. The last test concerned the estimation of muon-induced neutron flux coming from the rock at LNGS. The results have been compared with the flux obtained by other groups with a simulation program based on the FLUKA toolkit. A good agreement has been found within a factor two.

We used the LVDG4 to determine the active vetoing and the shielding power of LVD. The idea was to evaluate the feasibility to host a dark matter experiment in the LVD detector most inner part, called LVD Core Facility (LVD-CF). The first result is that LVD is a good moderator, but the iron supporting structure produces a great number of neutrons near the core. The second result is that if LVD is used as an active veto for muons, the neutron flux in the LVD-CF is reduced by a factor 50. Thus the residual neutron flux turns out to be at the same level as in Sudbury, the deepest underground laboratory.

Finally, the muon-induced neutron yield has been measured.

In liquid scintillator we found $(3.2 \pm 0.2) \times 10^{-4}$ n/g/cm², in good agreement

with previous measurements performed at different depths and with the general trend predicted by theoretical calculations and Monte Carlo simulations.

Moreover we present the first measurement, in our knowledge, of the neutron yield in iron: $(1.9 \pm 0.1) \times 10^{-3}$ n/g/cm².

That measurement provides an important validation of simulation codes of neutron production in heavy materials that are often used as shield in low background experiments.

Bibliography

- [1] A. Zichichi, Proceedings of the GUD-Workshop on "*Physics and Astrophysics with a Multikiloton Modular Underground Track Detector*", Rome, Italy, 29-31 October 1981 (INFN, Frascati, 1982), 141.
A. Zichichi, "*Perspectives of Underground Physics: the Gran Sasso Project*", Invited Plenary Lecture presented at the Symposium: "*Present Trends, Concepts and Instruments of Particle Physics*" in Honour of M. Conversi 70th Birthday, Rome, 3-4 November 1987; CERN EP/88-28.
A. Zichichi, Proceedings of the Workshop on "*Science Underground*", Los Alamos, NM, USA, 27 September-1 October 1982 (Amer. Inst. Phys., New York, 1983), 52.
- [2] *LNGS annual reports 2009*,
http://www.lngs.infn.it/lngs_infn/contents/lngs_en/research/experiments_scientific_info/library_publications/preprint_reports/report09/Intro_AR_2009.pdf
- [3] V.A. Kudryavtsev *et al.*, Eur. Phys. J. A **36** (2008) 171.
- [4] H. Wulandari *et al.*, Astropart. Phys. **22** (2004) 313.
- [5] D.J. Littler, Proc. Phys. Soc. London A **64** (1951) 638.
- [6] E. Bellotti *et al.*, INFN/TC-85/19, October 1985.
- [7] G. Bellini, Borexino proposal to Gran Sasso Laboratory, 1991, p. 184.
- [8] Y. Feige *et al.*, J. Geophys. Res. **73** (10) (1968) 3135.
- [9] M. Aglietta *et al.*, Phys. Rev. **D**, 58 (1998) 092005.

- [10] M. Aglietta *et al.*, Phys. Rev. **D**, 60 (1999) 112001.
- [11] M. Aglietta *et al.*, Phys. Atom. Nucl. 66 (2003) 123.
- [12] P. Antonioli *et al.*, Astropart. Phys. **7** (1997) 357.
- [13] V.A. Kudryavtsev *et al.*, Phys. Lett. B **471** (1999) 251.
- [14] A.S. Malgin *et al.*, Phys. Atom. Nucl. **71** (10) (2008) 1769.
- [15] C.F. Weizsacker, Z. Phys. **88** (1934) 612.
- [16] M. Aglietta *et al.*, Il Nuovo Cimento **A** (1992) 1793.
- [17] M. Aglietta *et al.*, Nucl. Instr. and Meth. **A** 277 (1989) 17.
- [18] A. Bigongiari *et al.*, Nucl. Instr. and Meth. **A** 228 (1990) 529.
- [19] P. Antonioli *et al.*, New Journal of Physics **6** (2004) 114.
- [20] N.Yu. Agafonova *et al.*, Astropart. Phys. **28** (2008) 516.
- [21] N.Yu. Agafonova *et al.*, Astropart. Phys. **27** (2007) 254.
- [22] M. Aglietta *et al.*, Nucl. Instr. and Meth. **A** 516 (2004) 96.
- [23] P. Antonioli *et al.*, Nucl. Instr. and Meth. **A** 309 (1991) 569.
- [24] M. Aglietta *et al.*, Astropart. Phys. **9** (1998) 185.
- [25] M. Selvi *et al.*, Proceedings of the 31st International Cosmic Ray Conference (ICRC 2009), Lodz, Poland, 7-15 July 2009.
- [26] A. Bassignani *et al.*, Radiation Measurements **5**, Nos 1-4, (1995) 557.
- [27] G. Bruno *et al.*, Proceedings of the International Conference on Topics in Astroparticle and Underground Physics (TAUP 2009), Rome, Italy, 1-5 July 2009.
- [28] I. R. Barabanov *et al.*, e-Print: aeXiv:0803.1577 [physics.ins-det]
- [29] F. Arneodo *et al.*, LNGS preprint, LNGS-EXP-02-08 (2008).

- [30] A. Bonardi, Ph.D. Thesis, Turin University (2010).
- [31] M. Selvi *et al.*, Proceedings of the 7th International Workshop on the Identification of Dark Matter 2008, Stockholm, Sweden, 18-22 August 2008.
- [32] H. L. Anderson, Los Alamos Science 14, pp. 96-108 (1986).
- [33] N. Metropolis, Los Alamos Science Special Issue dedicated to Stanislaw Ulam, pp. 125-130 (1987).
- [34] GEANT Detector Description and Simulation Tool, <http://wwwinfo.cern.ch/asdoc/pdfdir/geant.pdf>
- [35] FLUKA manual, <http://www.fluka.org/content/manuals/FM.pdf>
- [36] J. Ranft, Nucl. Instr. Meth. **81** (1970) 29.
- [37] K. Amako *et al.*, Proceedings of CHEP94, San Francisco, CA, USA, LBL-35822 CONF-940492.
- [38] S. Giani *et al.*, Geant4: An object-oriented toolkit for simulation in HEP, CERN/LHCC 98-44, 1998.
- [39] J. Allison *et al.*, IEEE Trans. Nucl. Sci. **53** (2006) 270.
- [40] S. Agostinelli *et al.*, Nucl. Instrum. Meth. A **506** (2003) 250.
- [41] Geant4 website, <http://geant4.cern.ch>
- [42] P.V. Degtyarenko *et al.*, Eur. Phys. J. A **9** (2000) 421.
- [43] H. Fesefeldt, RWTH Aachen report PITHA 85/02 (1985).
- [44] National Nuclear Data Center website, <http://www.nndc.bnl.gov>
- [45] J.J. Griffin, Phys. Rev. Lett. **17** (1966) 478.
- [46] J.M. Quesada *et al.*, Proceedings of the MC2010 sistemare meglio la referenza
- [47] ROOT home page at CERN, <http://root.cern.ch>

- [48] P.G. Catalano, Mem. Soc. Geol. It. **35** (1986) 647.
- [49] K. Amako *et al.*, IEEE Trans. Nucl. Sci. **54** (2005) 910.
- [50] E. Poon and F. Verhaegen, Med. Phys. **32** (2005) 1696.
- [51] D.H. Wright, Proceedings of the Monte Carlo Conference (MC2010)
<http://geant4.cern.ch/results/papers/hadronic-progress-MC2010.pdf>
- [52] A. Dotti *et al.*, Proceedings of the Conference of Calorimetry (CALOR2010)
<http://geant4.cern.ch/results/papers/hadronic-CALOR2010.pdf>
- [53] G. Folger *et al.*, Eur. Phys. J. A **21** (2004) 407.
- [54] J. Apostolakis *et al.*, Rad. Phys. and Chem. **78** (2009) 859.
- [55] S. Taniguchi *et al.*, Nucl. Instr. and Meth. A **503** (2003) 595.
- [56] S. Roeslera *et al.*, Nucl. Instr. and Meth. A **503** (2003) 606.
- [57] M. Boswell *et al.*, (2010) arXiv:1011.3827v1
- [58] M.G. Marino *et al.*, Nucl. Instr. and Meth. A **582** (2007) 611.
- [59] R. Lemrani *et al.*, Nucl. Instr. and Meth. A **560** (2006) 454.
- [60] Briesmeister *et al.*, (Eds.), MCNP-Version 4B (and later), LA-12625-M, LANL, 1997.
- [61] MCNPX home page, <http://mcnpx.lanl.gov>
- [62] Y.F. Wang *et al.*, Phys. Rev. D **64** (2001) 013012.
- [63] V.A. Kudryavtsev *et al.*, Nucl. Instr. and Meth. A **505** (2003) 688.
- [64] H.M. Araujo *et al.*, Nucl. Instr. and Meth. A **545** (2005) 398.
- [65] V. Chazal *et al.*, Nucl. Instr. and Meth. A **490** (2002) 334.
- [66] L. Bergamasco *et al.*, Il Nuovo Cimento A **13** (1973) 403.
- [67] G.V. Gorshkov *et al.*, Sov. J. Nucl. Phys. **18** (1974) 57.

- [68] A. Lindote *et al.*, *Astropart. Phys.* **31** (2009) 366.
- [69] D.M. Mei and A. Hime, *Phys. Rev. D* **73** (2006) 053004.
- [70] L.B. Bezrukov *et al.*, *Sov. J. Nucl. Phys.* **17** (1973) 51.
- [71] D.M. Mei, Ph.D. thesis, the Univeristy of Alabama, 2003.
- [72] A. Dementyev *et al.*, *Nucl. Phys. B (Proc.Suppl)* **70** (1999) 486.
- [73] R. Persiani, Degree Thesis, Bologna University (2007).
- [74] M.J. Carson *et al.*, *Astropart. Phys* **21** (2004) 667.
- [75] D.C. Hoffman *et al.*, *Phys. Rev. C* **21** (1980) 637.
- [76] G. Badino *et al.*, *Il Nuovo Cimento C* **7** (1984) 573.
- [77] R. Hertenberger *et al.*, *Phys. Rev. C* **52** (1995) 3449.
- [78] F. Boehm *et al.*, *Phys. Rev. D* **62** (2000) 092005.
- [79] R.I. Enikeev *et al.*, *Sov. J. Nucl. Phys.* **46** (1987) 883.
- [80] M. Aglietta *et al.*, *Proc.26th Inter. Cosmic Ray Conf.*, Vol. **2**, (1999) 44.
- [81] M. Aglietta *et al.*, *Nuovo Cimento C* **12** (1989) 467.
- [82] S. Abe *et al.*, *Phys. Rev. C* **81** (2010) 025807.